AIR QUALITY MODELS AND UNUSUALLY LARGE OZONE INCREASES: IDENTIFYING MODEL FAILURES, UNDERSTANDING ENVIRONMENTAL CAUSES, AND IMPROVING MODELED CHEMISTRY

Evan A. Couzo

A dissertation submitted to the faculty of the University of North Carolina at Chapel Hill in partial fulfillment of the requirements for the degree of Doctor of Philosophy in the Department of Environmental Sciences and Engineering in the Gillings School of Global Public Health.

Chapel Hill
2013

Approved by:

William Vizuete, Advisor

Harvey E. Jeffries, Reader

Jason D. Surratt, Reader

Tom W. Tesche, Reader

John P. Dawson, Reader

ABSTRACT

EVAN A. COUZO: Air quality models and unusually large ozone increases: Identifying model failures, understanding environmental causes, and improving modeled chemistry
(Under the direction of William Vizuete)

Several factors combine to make ozone (O_3) pollution in Houston, Texas, unique when compared to other metropolitan areas. These include complex meteorology, intense clustering of industrial activity, and significant precursor emissions from the heavily urbanized eight-county area. Decades of air pollution research have borne out two different causes, or conceptual models, of O_3 formation. One conceptual model describes a gradual region-wide increase in O_3 concentrations ''typical'' of many large U.S. cities. The other conceptual model links episodic emissions of volatile organic compounds to spatially limited plumes of high O_3, which lead to large hourly increases that have exceeded 100 parts per billion (ppb) per hour. These large hourly increases are known to lead to violations of the federal O_3 standard and impact Houston's status as a non-attainment area. There is a need to further understand and characterize the causes of peak O_3 levels in Houston and simulate them correctly so that environmental regulators can find the most cost-effective pollution controls.

This work provides a detailed understanding of unusually large O_3 increases in the natural and modeled environments. First, we probe regulatory model simulations and assess their ability to reproduce the observed phenomenon. As configured for the purpose of demonstrating future attainment of the O_3 standard, the model fails to predict the spatially limited O_3 plumes observed in Houston. Second, we combine ambient meteorological and pollutant measurement data to identify the most likely geographic origins and preconditions of the concentrated O_3 plumes. We find evidence

that the O_3 plumes are the result of photochemical activity accelerated by industrial emissions. And, third, we implement changes to the modeled chemistry to add missing formation mechanisms of nitrous acid, which is an important radical precursor. Radicals control the chemical reactivity of atmospheric systems, and perturbations to radical budgets can shift chemical pathways. The mechanism additions increase the concentrations of nitrous acid, especially right after sunrise. The overall effect on O_3 is small (up to three ppb), but we demonstrate the successful implementation of a surface sub-model that chemically processes adsorbed compounds. To our knowledge, this is the first time that chemical processing on surfaces has been used in a three-dimensional regulatory air quality model.

TABLE OF CONTENTS

LIST OF TABLES

LIST OF FIGURES

LIST OF ABBREVIATIONS AND SYMBOLS

AG	Alpine Geophysics LLC
AIRS	Aerometric Information Retrieval System
AQM	air quality model
BAYP	Bayland Park ambient monitoring station
CAMS	Continuous Ambient Monitoring Station
CAMx	Community Air Quality Model with extensions
CH_2O	formaldehyde
CLIN	Clinton ambient monitoring station
CMAQ	Community Multiscale Air Quality model
CNR2	Conroe Relocated ambient monitoring station
DRPK	Deer Park ambient monitoring station
EI	emission inventory
EPA	United States Environmental Protection Agency
ETH	Carbon Bond representation of ethene
Glo-BEIS	Global Biosphere Emissions and Interactions System
HALC	Aldine ambient monitoring station
HCHV	Channelview ambient monitoring station
HCQA	Croquet ambient monitoring station
HLAA	Lang ambient monitoring station
HNO_3	nitric acid
$HO_2^{\cdot}$	hydroperoxy radical

HROC	Houston Regional Office ambient monitoring station
HRVOC	highly reactive volatile organic compound
HSMA	Monroe ambient monitoring station
HTCA	Texas Avenue ambient monitoring station
HWAA	North Wayside ambient monitoring station
IOLE	Carbon Bond representation of internal olefin
LP-DOAS	long-path differential optical absorption spectroscopy
LYNF	Lynchburg Ferry ambient monitoring station
MACP	Manvel Croix Park ambient monitoring station
MEGAN	Model of Emissions of Gases and Aerosols from Nature
MM5	5^{th} generation National Center for Atmospheric Research/Pennsylvania State University Mesoscale Model
MOVES	Motor Vehicle Emission Simulator
MOZART-4	Model for Ozone and Related Chemical Tracers 4
NAAQS	National Ambient Air Quality Standard
NEI	National Emission Inventory
NME	normalized mean error
NO	nitric oxide
NO_2	nitrogen dioxide
NO_x	nitrogen oxides (NO + NO_2)
NTOC	non-typical ozone change
OLE	Carbon Bond representation of olefin
$^{\cdot}OH$	hydroxyl radical

O_3	ozone
PA	process analysis
PBL	planetary boundary layer
ppb	parts per billion
ppm	parts per million
pyPA	Python-based process analysis
SAPRC	Statewide Air Pollution Research Center
SBFP	Seabrook Friendship Park ambient monitoring station
SHARP	2009 Study of Houston Atmospheric Radical Precursors
SHWH	Westhollow ambient monitoring station
SIP	state implementation plan
SO_2	sulfur dioxide
TCEQ	Texas Commission on Environmental Quality
TRAMP	2006 Texas Air Quality Study Radical Measurement Program
TXCT	Texas City ambient monitoring station
VOC	volatile organic compound
WALV	Wallisville ambient monitoring station
WRF	Weather Research and Forecasting model
WRF-CHEM	Weather Research and Forecasting model coupled with Chemistry

CHAPTER 1

INTRODUCTION

Several factors combine to make Houston's O_3 problem unique when compared to other metropolitan areas in the U.S. These include the complex interactions between land-sea breeze circulations, intense clustering of industrial emission sources in the Houston ship channel and coastal areas, significant precursor emissions from the heavily urbanized eight-county area, and potential pollution transport from domestic and international source regions. The culmination of these factors has resulted in a complex and difficult environment to understand. This difficulty has garnered the attention of researchers and regulators with the common goal of understanding how O_3 is formed.

The resulting science and policies describe two unique causes, or conceptual models, for how high O_3 is formed in Houston. Figure 1.1 shows examples of each type of O_3 formation. One conceptual model - the blue line - describes a gradual region-wide increase in O_3 concentrations ''typical'' of many large U.S. cities. This conceptual model is well represented in the gradual evolution of O_3 seen in observations and predicted in photochemical models. The second conceptual model - the red line in Figure 1.1 - was first discovered in Houston and has been linked to episodic emission events of volatile organic compounds (VOCs). On days with unique wind conditions (Banta et al., 2005; Cowling et al., 2007; Ngan and Byun, 2011), these emissions produce narrow plumes of high O_3 concentrations that appear in only a few surface measurements as large changes in hourly pollutant measurements. On the basis of this dual conceptual model for high O_3, the Texas Commission on Environmental Quality (TCEQ) proposed, and the U.S. Environmental Protection Agency (EPA)

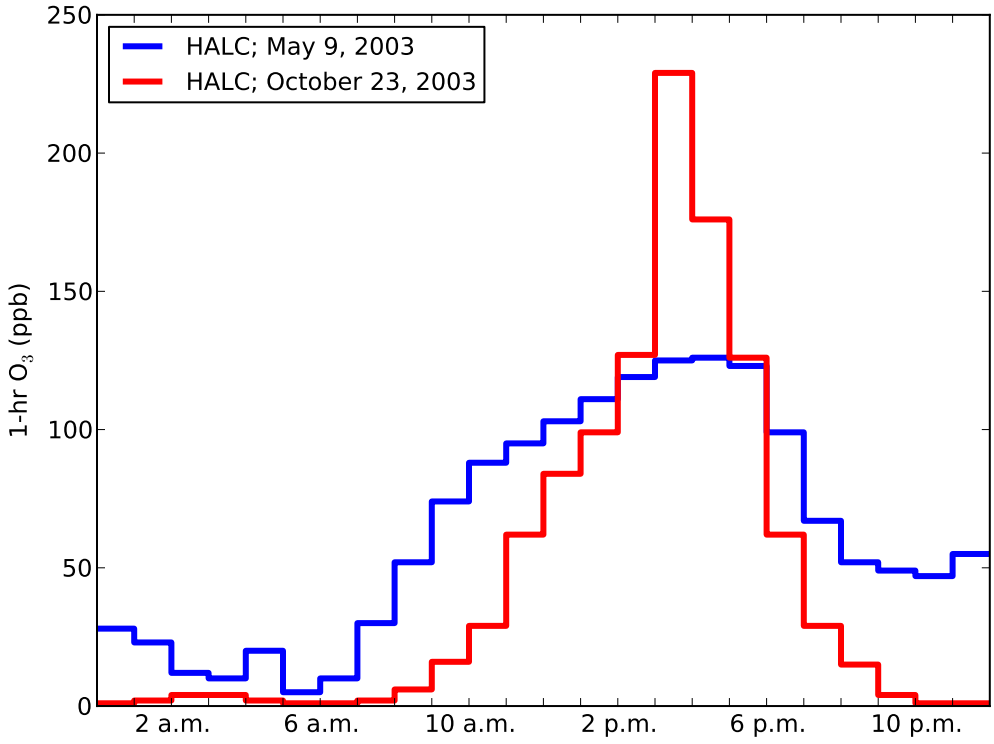

Figure 1.1: Observed 1-hr O_3 concentrations at the HALC monitor. "Typical" O_3 evolution - gradual hourly increases - is illustrated by the blue line. The red line shows a second kind of O_3 evolution - a non-typical O_3 change (NTOC).

accepted, a dual mitigation approach in their 2004 State Implementation Plan (SIP) (Texas Commission on Environmental Quality, 2004).

The 2004 SIP established for the first time a dual-O_3 management paradigm in Houston, Texas. In this SIP, the TCEQ recognized that relatively small amounts of short-term emissions from particular industrial sources of highly reactive alkenes could lead to a large, short-duration O_3 peak that skewed the observational attainment metrics used to calculate attainment of the federal O_3 standard. Most of these highest observations occurred at only a single monitor over the course of a day. Using observational and modeling evidence, the TCEQ proposed an innovative method

for targeting four VOCs termed highly reactive VOCs (HRVOCs), which include ethene, propene, 1,3-butadiene, and all butene isomers. Management strategies were developed to reduce the short-term and highly variable industrial releases of HRVOCs. A maximum hourly rate of 1200 lbs/hr was proposed by the TCEQ and was subsequently written into Texas state law. As defined in the TCEQ's 2004 SIP, this short-term cap applied to both unauthorized emissions and permitted emissions that may fluctuate on an hourly basis. Compliance with these new HRVOC controls necessitated significant abatement investments by certain industrial sources. Indeed, polymer production facilities in the region were reported to have spent up to $2.4 million in equipment to monitor and reduce HRVOCs emissions (Yarwood et al., 2008).

The state of Texas is now grappling with how it will show attainment of the 1997 8-hr O_3 standard of 0.08 parts per million (ppm) and, later, the 2008 8-hr O_3 standard of 0.075 ppm. The 8-hr O_3 metric and an updated EPA attainment methodology have been applied for the first time in Houston by the TCEQ for their 2010 SIP (Texas Commission on Environmental Quality, 2010). In Vizuete et al. (2011), we quantified the effect of large hourly O_3 changes, called non-typical O_3 changes (NTOCs), on the attainment metrics calculated in the 2010 SIP. We found that NTOCs occur on many of the days that determine whether an air quality monitor has attained the federal O_3 standard and, in fact, prevented some monitors from attaining the standard.

There is a need to further understand all of the causes of peak 8-hr O_3 levels in Houston, simulate them correctly, and find the most cost-effective controls. Houston's designation as a non-attainment region is in large part due to the NTOC phenomenon. Thus, identifying their environmental causes and accurately representing them in regulatory models is of paramount importance to the development of effective control strategies. High O_3 and rapid rates of O_3 production are the result of fast chemistry in industrial regions. This body of work identifies and quantifies modeled NTOC

performance, characterizes environmental conditions and geographic origins of observed NTOCs, and implements a new modeling framework that better represents free radical sources.

REFERENCES

R. M. Banta, C. J. Senff, J. Nielsen-Gammon, L. S. Darby, T. Ryerson, J. Alvarez, S. Sandberg, E. Williams, and M. Trainer (2005). A bad air day in Houston. *Bull. Am. Meteorol. Soc.*, 86(5):657--669. doi:10.1175/BAMS-86-5-657.

E. Cowling, C. Furiness, B. Dimitriades, and D. Parrish (2007). Final rapid science synthesis report: Findings from the second Texas Air Quality study (TexAQS II) - Final report to the Texas Commission on Environmental Quality. TCEQ Contract Number 582-4-65614. http://www.tceq.info/assets/public/implementation/air/am/texaqs/rsst_final_report_pdf.

F. Ngan and D. Byun (2011). Classification of weather patterns and associated trajectories of high-ozone episodes in the Houston-Galveston-Brazoria area during the 2005/06 TexAQS-II. *J. Appl. Meteorol. Climatol.*, 50:485--499. doi:10.1175/2010jamc2483.1.

Texas Commission on Environmental Quality (2004). Revisions to the State Implementation Plan (SIP) for the control of ozone air pollution: Houston/Galveston/Brazoria ozone nonattainment area. Austin, TX. Project No. 2004-042-SIP-NR.

Texas Commission on Environmental Quality (2010). Revisions to the State Implementation Plan for the control of ozone air pollution: Houston-Galveston-Brazoria ozone nonattainment area. Austin, TX. Project No. 2009-017-SIP-NR.

W. Vizuete, H. E. Jeffries, T. W. Tesche, E. P. Olaguer, and E. Couzo (2011). Issues with ozone attainment methodology for Houston, TX. *J. Air Waste Manag. Assoc.*, 61:238--253. doi:10.3155/1047-3289.61.3.238.

G. Yarwood, S. H. Ramsey, C. J. Colville, and S. B. Bhat (2008). Cost analysis of HRVOC controls on polymer plants and flares. Project 2008-104. ENVIRON International Corporation: Novato, CA.

CHAPTER 2
ASSESSMENT OF A REGULATORY MODEL'S PERFORMANCE RELATIVE TO LARGE SPATIAL HETEROGENEITY IN OBSERVED OZONE IN HOUSTON, TEXAS[1]

2.1 Introduction

In 2010, the state of Texas proposed policies aimed at reducing ozone (O_3) concentrations in Houston. These policies are described and justified with modeling and observational data in a document called the State Implementation Plan (SIP) (Texas Commission on Environmental Quality, 2010c), which follows the U.S. Environmental Protection Agency (EPA) attainment methodology (U.S. Environmental Protection Agency, 2007). The EPA attainment methodology describes the use of observational and modeling data to show attainment, and the assumptions underlying it have been the focus of several studies (Jones et al., 2005; Sistla et al., 2004; Vizuete et al., 2010, 2011). Specifically for Houston, researchers have found that the metrics used in the attainment methodology were influenced by large hourly changes in observed O_3 concentrations. In the observational data used by the 2010 SIP, it has been shown that some of the highest 8-hr O_3 levels included hourly changes in O_3 concentrations of at least 40 ppb in 1 hr, or 60 ppb in 2 hr (Vizuete et al., 2011). These large hourly changes usually appear at only a few monitors spanning a narrow geographic

[1] E. Couzo, A. Olatosi, H.E. Jeffries, W. Vizuete, Assessment of a regulatory model's performance relative to large spatial heterogeneity in observed ozone in Houston, Texas. *J. Air Waste Manag. Assoc.* **2012**, 62, 696-706, doi: 10.1080/10962247.2012.667050.

area. The observed large hourly changes are the result of a plume of higher O_3 being advected to the monitor site. These observations suggest high spatial heterogeneity in O_3 concentrations across Houston.

Using observational data collected by regulatory monitors from 2000 to 2009, days were identified on which there was an hourly change in O_3 concentrations of at least 40 ppb, or 60 ppb in 2 hr. These larger-than-typical hourly changes are called non-typical O_3 changes, or NTOCs. In Figure 2.1, all regulatory measurements made during 2000-2009 are separated into two categories, days on which a NTOC was measured and days on which only typical O_3 changes were observed. Shown are the distributions of measured 1-hr and 8-hr O_3 daily maximum concentrations. It is clear from Figure 2.1 that NTOC days have higher peak 1-hr and 8-hr O_3 concentrations than typical days. The greatest 1-hr peak measured on NTOC days is 229 ppb; 1-hr peaks on typical days never reached 170 ppb. The 25th, 50th, and 75th percentile values are also substantially different. The median peak 1-hr O_3 value for NTOC days is 107 ppb, 66 ppb greater than for typical days. Data from daily maximum 8-hr O_3 concentrations show the same trend. The median peak 8-hr concentration for NTOC days is 79 ppb, more than 45 ppb greater than for typical days, and at 145 ppb the greatest peak 8-hr value is about 15 ppb greater for NTOC days than typical days. In fact, the six greatest peak 8-hr O_3 values recorded between 2000 and 2009 occurred when a monitor was impacted by a NTOC. Overall, nearly 60% of all NTOC days exceeded the 8-hr O_3 National Ambient Air Quality Standard (NAAQS; 0.08 ppm), but just 1% of typical days exceeded the federal limit. Probability density functions for all daily maximum 8-hr O_3 from 2000 to 2009 are shown in Figure 2.2. Only measurement data from May through October are shown. The figure also shows which 8-hr O_3 concentrations were measured on days including an hourly change that would be considered a NTOC. The typical O_3 change days dominate all 8-hr maxima

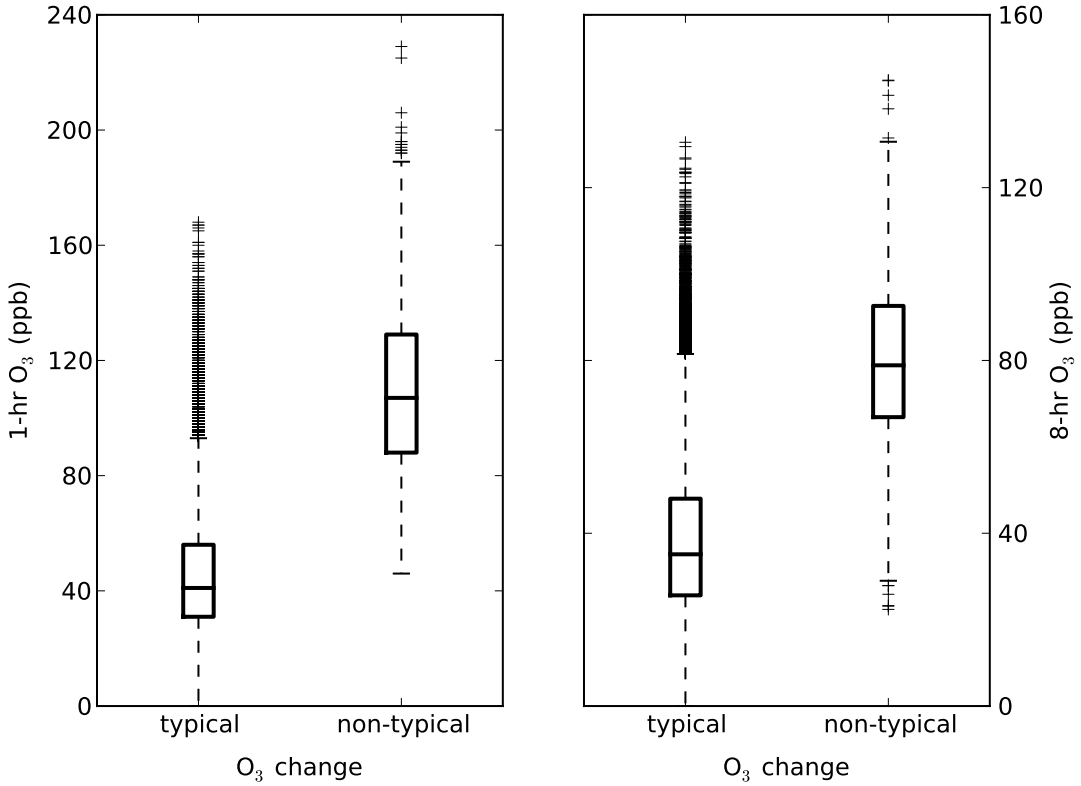

Figure 2.1: Distributions of observed daily maximum 1-hr (left) and 8-hr (right) o_3 concentrations at all regulatory monitors from 2000 to 2009. The data are separated into typical and non-typical days. A typical o_3 change day has observed 1-hr changes in o_3 concentration of less than 40 ppb, or 2-hr changes less than 60 ppb. A non-typical o_3 change day has a 1-hr change of at least 40 ppb, or a 2-hr change of at least 60 ppb. The 25th, 50th, and 75th percentile concentrations are represented by the box bottom, middle, and top.

below 20 ppb, but do extend well above the 85 ppb O_3 standard. All observed 8-hr O_3 values above 131 ppb, though, were from NTOC days.

The exact cause of all observed NTOCs is still an open question and a challenge to answer given the available data. There is considerable evidence, however, that has linked some observed NTOCs to short-term releases of ethene, propene, butene isomers, and 1,3-butadiene (collectively called highly reactive volatile organic compounds [HRVOCs]). Observed NTOCs at monitor sites show coincidental concentrations of HRVOCs, and back trajectories point toward industrial sources in the Houston ship

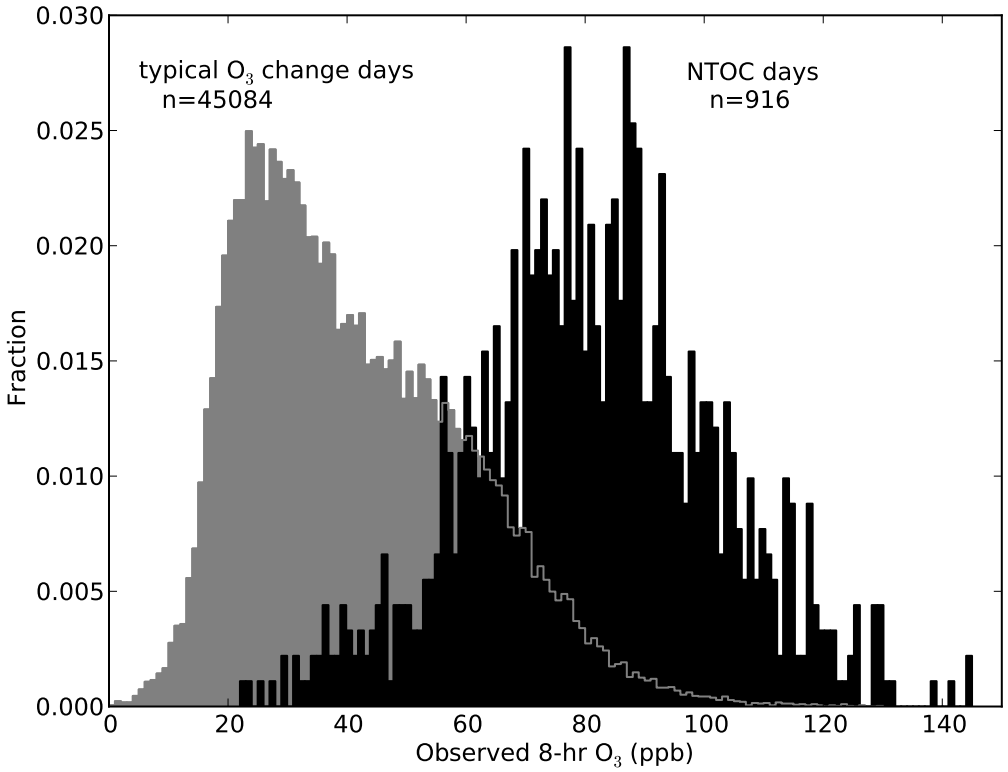

Figure 2.2: Distributions of observed daily maximum 8-hr O_3 concentrations at all regulatory monitors from 2000 to 2009. Only measurement data from May to October are shown (n=46,000 monitor-days). The black columns are daily maximum 8-hr O_3 concentrations that were measured on days that had a non-typical O_3 change (NTOC), i.e., an observed O_3 change of at least 40 ppb/hr, or 60 ppb/2 hr (n=916 monitor-days). The gray columns are 8-hr O_3 concentrations that did not include an observed NTOC (n=45,084 monitor-days).

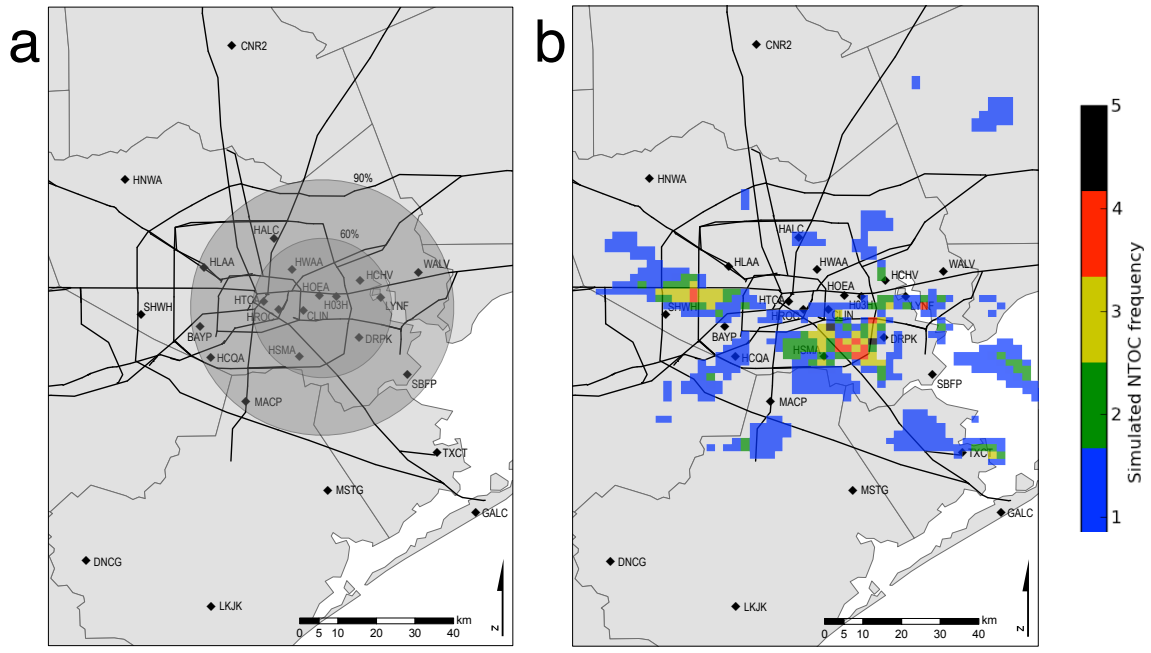

Figure 2.3: The location of the 25 regulatory air quality monitors used in this study. Plot (a) shows ten years of measurements spanning 2000-2009. For those monitors that came online after 2000, data collection began on the deployment date and continued through 2009. For this time period, the inner shaded circle shows the monitors at which 60% of all non-typical O_3 changes (NTOCs) were observed. The outer shaded circle covers the monitors at which 90% of all NTOCs were observed. Both circles are centered on the ship channel. Plot (b) shows the grid cell location and frequency of simulated NTOCs by the base case simulation in the 2-km modeling domain for the entire 120-day modeling episode.

channel (Gan and Hopke, 2003; Vizuete et al., 2008). Using the NTOC criteria and observational monitoring data from 2000 to 2009, it is clear that most NTOCs are observed near the ship channel region in Houston. Figure 2.3a shows all the regulatory monitors in the Houston region and indicates which monitors most frequently measure NTOCs. The circles in the figure are centered on the ship channel. The inner circle shows that less than half of the monitoring stations account for 60% of observed NTOCs. The larger circle includes seven additional monitors and accounts for 90% of NTOC measurements.

Short-term HRVOC emissions from industrial sources occur often and with notable

temporal variability in Houston (Cowling et al., 2007; McCoy et al., 2010; Murphy and Allen, 2005; Webster et al., 2007; Wert et al., 2003). These emissions are random, and, although rare at any one facility, due to Houston's massive industrial network, there were more than 1000 releases reported in 2003 (Murphy and Allen, 2005). Immediately after a release, modeling and observational evidence suggest an initial period of rapid O_3 formation that results in a spatially limited downwind plume of high O_3 (Henderson et al., 2010; Kleinman et al., 2002; Ryerson et al., 2003; Xiao et al., 2010). One study found that targeted episodic HRVOC emissions from the ship channel can correct for low reactivity in models (Byun et al., 2007). Sensitivity to nitrogen oxide (NO_x) emissions, though, was found to be small because NO_x is fairly constant over time and well represented in emission inventories. By design, the largest NO_x point sources (electric generating units and petrochemical facilities) operate continuously so variability in emissions tends to be small. Since NO_x is a byproduct of combustion, it is unlikely that leaks or accidental releases of NO_x occur. Mobile NO_x sources are important to O_3 formation, but evidence to support a relationship between NTOC formation and the predictable changes in NO_x emissions (i.e., daily, weekly, or seasonal variability) has not been found. Furthermore, NTOCs are still observed and impacting attainment metrics despite improvements in Houston's air quality vis-*à*-vis NO_x emissions.

To be sure, Houston's unique meteorology is a major determinant of high O_3, and an emission event must meet several conditions to affect O_3 concentrations. For an HRVOC release event to create a heterogeneous O_3 plume, the release must have sufficient magnitude, occur in the morning, and coincide with O_3 conducive meteorological conditions (Czader et al., 2008; Henderson et al., 2010; Vizuete et al., 2008). These meteorological conditions have been described in detail and are characterized at surface monitors by low wind speeds and a rotational wind field (Banta et al., 2005; Cowling

et al., 2007; Ngan and Byun, 2011). An analysis of winds and NAAQS exceedances in Houston, however, determined that O_3 conducive meteorological conditions are necessary but insufficient to produce high O_3 (Vizuete et al., 2009).

Distinct meteorological conditions, the stochastic nature of the emissions, and the short atmospheric lifetime of the released VOCs have provided a challenge to understand the role these emissions play in contributing to high O_3 in Houston. Although data exist that link some observed NTOCs with reported or measured HRVOC emissions, a vast majority of NTOCs lack any data that can provide a causal explanation. Thus, alternative causes for observed NTOCs are still permissible. Further, observational attainment metrics used in the 2010 SIP are influenced by unexplained NTOCs. Observational metrics are only part of the EPA attainment test. The methodology also requires the use of modeling data to predict future O_3 values for all regulatory air quality monitors. Since NTOCs are found in the observational record, this logically calls into question whether the phenomenon is adequately represented in the regulatory AQM.

Due to the magnitude and narrow spatial extent of the hourly O_3 change, this phenomenon is markedly different from the ‘‘typical,’’ i.e., gradual, concentration changes commonly seen in other cities. Therefore, understanding the cause of these ‘‘non-typical’’ hourly changes becomes critical to developing an effective and defensible regulatory air quality policy in Houston. The regulatory modeling created by the Texas Commission on Environmental Quality (TCEQ) in support of the 2010 SIP provides an opportunity to assess the ability of existing AQMs to simulate the heterogeneity of O_3 concentrations observed in Houston. Here, the regulatory modeling created for the TCEQ's 2010 SIP is used to evaluate the ability of the AQM to simulate the spatial extent and magnitude of observed NTOC behavior and to identify any possible links to large HRVOC emissions.

2.2 Methods

This study combines observational data measured at ground station air quality monitors and regulatory AQM predictions used by the TCEQ to support their 2010 8-hr O_3 SIP. In developing the model simulations, the TCEQ followed the EPA guidance document on attaining the 8-hr O_3 NAAQS (U.S. Environmental Protection Agency, 2007). All measured and simulated data are maintained by the TCEQ and available publicly (Texas Commission on Environmental Quality, 2010a,b).

2.2.1 Observational data

Observed data were obtained from the TCEQ website, which provides hourly averaged measurement data. Twenty-five monitoring stations were used in this study, and they are listed in Table 2.1 with their official names, four-letter abbreviation, Continuous Ambient Monitoring Station (CAMS) number, and Aerometric Information Retrieval System (AIRS) number; these are the same monitors used in the TCEQ's 2010 SIP. Monitor locations are shown in Figure 2.3.

It should be noted that the observational data set spans a period (2000-2009) of substantial changes in precursor emissions. As detailed in the TCEQ's 2010 SIP, measured NO_x, HRVOC, and O_3 concentrations have decreased following emissions control programs. The observational data presented here may not reflect the current state of the Houston airshed, but they are significant nevertheless because they were used to formulate the latest SIP.

2.2.2 Air quality model data

The TCEQ used the Comprehensive Air Quality Model with Extensions (CAMx) version 4.53 (ENVIRON International Corporation, 2008) with the Carbon Bond V chemical mechanism and the fifth generation Penn State/National Center for

Monitor Name	Abbreviation	CAMS No.	AIRS No.
Bayland Park	BAYP	53	48-201-0055
Clinton	CLIN	403	48-201-1035
Conroe Relocated	CNR2	78	48-339-0078
Danciger	DNCG	618	48-039-0618
Deer Park	DRPK	35	48-201-1039
Galveston	GALC	34	48-167-0014
HRM-3 Haden Road	H03H	603	48-201-0803
Aldine	HALC	8	48-201-0024
Channelview	HCHV	15	48-201-0026
Croquet	HCQA	409	48-201-0051
Lang	HLAA	408	48-201-0047
Northwest Harris County	HNWA	26	48-201-0029
Houston East	HOEA	1	48-201-1034
Houston Regional Office	HROC	81	48-201-0070
Monroe	HSMA	406	48-201-0062
Texas Avenue	HTCA	411	48-201-0075
North Wayside	HWAA	405	48-201-0046
Lake Jackson	LKJK	1016	48-039-1016
Lynchburg Ferry	LYNF	1015	48-201-1015
Manvel Croix Park	MACP	84	48-039-1004
Mustang Bayou	MSTG	619	48-039-0619
Seabrook Friendship Park	SBFP	45	48-201-1050
Westhollow	SHWH	410	48-201-0066
Texas City	TXCT	620	48-167-0056
Wallisville	WALV	617	48-201-0617

Table 2.1: The 25 air quality monitors used in this study. The full name and four-letter abbreviation for each monitor are given. Also included are the Continuous Ambient Monitoring Station (CAMS) number and the Aerometric Information Retrieval System (AIRS) number.

Atmospheric Research Mesoscale Model (MM5) version 3.7.3 to generate simulation data. Detailed documentation concerning the development of AQM inputs can be found on the TCEQ website (Texas Commission on Environmental Quality, 2010a). In total, there are 120 modeling days in the 2005 and 2006 episodes. A regional 36-km domain and a 12-km eastern Texas subdomain provide boundary conditions for a 4-km Houston Galveston Brazoria/Beaumont Port Arthur subdomain. A finely resolved 2-km Houston Galveston subdomain was also developed, and all analysis in this study was focused there unless explicitly stated otherwise.

The TCEQ developed, in accordance with EPA guidance, two distinct emission inventories (EIs), named base case and baseline. Using each EI, CAMx generated model predictions of O_3 using identical meteorology. Model predictions made using the base case EI were used to evaluate model performance, whereas model predictions with the baseline EI were used to demonstrate attainment of the O_3 NAAQS. The base case EI includes day-specific emissions, which can be highly variable in the industrial areas of Houston. The baseline EI, however, has day specificity removed and instead relies on spatially and temporally averaged emissions. According to the TCEQ's 2010 SIP documentation, the major difference between the two EIs is the representation of point source emissions. The base case uses hour- and day-specific emission rates for each emissions source, whereas baseline point source emissions are, for each hour, averaged across all simulated days. In other words, baseline point emissions for a given source have some average diurnal variation, but are identical from one day to the next. This is true for both HRVOC and NO_x point sources.

Figure 2.4 provides a detailed comparison of base case and baseline hourly point source HRVOC emissions. The main plot shows hourly emission rates for the subset of point sources that are included in both inventories (not all point sources are included in both inventories). Each data point directly compares the rate in the base case to

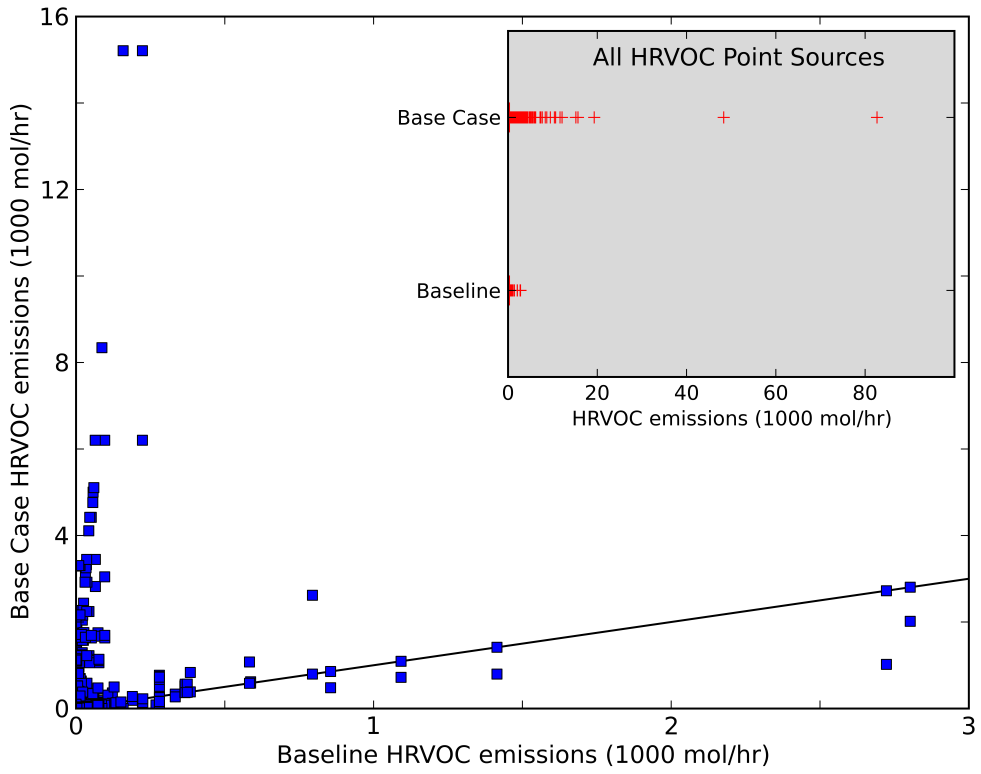

Figure 2.4: Comparison of base case and baseline hourly point source HRVOC emissions. The main plot shows hourly emission rates for the subset of point sources that are included in both inventories (not all point sources are included in both inventories). Each data point directly compares the rate in the base case to that in the baseline at a particular time and location. The solid black line shows where the emission rates in the two emission inventories are equivalent. The inset plot shows distributions of hourly HRVOC emission rates at all point sources in either inventory. Though the inset is more inclusive than the main plot, it does not provide a direct hour-by-hour, source-by-source comparison of the two inventories.

that in the baseline at a particular time and location. Points above the solid black line indicate that the emission rate was greater in the base case; points below the line indicate that the emission rate was greater in the baseline inventory. For most point sources at most times, the base case emission inventory has greater HRVOC emission rates. In a few instances, the differences are extreme. For 3 hr, one point source emitted 15,210 mol/hr HRVOC in the base case, but in the baseline inventory the emission rate is well under 500 mol/hr HRVOC. The inset plot shows distributions of hourly HRVOC emission rates at all point sources in either inventory. Though the inset is more inclusive than the main plot, it does not provide a direct hour-by-hour, source-by-source comparison of the two inventories. In the inset, the major HRVOC emission rate differences are found in the upper extrema. A number of base case emission rates are greater than the maximum found in the baseline inventory, where the maximum rate is 2,803 mol/hr. The maximum base case HRVOC emission rate is 82,660 mol/hr. Analysis of NO_x point sources also showed greater variability in the base case inventory, but the magnitudes of the differences between the base case and the baseline were much smaller. The maximum base case NO_x emission rate is 21,903 mol/hr, and the maximum rate in the baseline is 10,472 mol/hr.

The base case EI is the most accurate representation of a historical episode with hourly variability including reported industrial releases of HRVOCs. Further, considerable resources were used by the TCEQ to increase accuracy of industrial point source emissions. This included the development of an hourly special inventory that was based on reports from 141 facilities in Houston during the period of August 15 to September 15, 2006. The baseline EI does not include the data from the special inventory. Thus, this analysis focuses primarily on predictions made using the base case EI and whether it can replicate observed NTOC behavior.

Specifically for this study, a 1-km subdomain was nested within the 2-km subdo-

main, and the model was rerun for the special inventory period in 2006. Meteorological inputs for the 1-km subdomain were not created, but rather interpolated by CAMx from the 4-km subdomain. Gridded emission inputs were interpolated from the 2-km subdomain, whereas point source emissions retained their specific geographic location. It has been found previously that horizontal grid resolution can affect peak O_3 formation immediately following an imputed HRVOC emission event (Henderson et al., 2010). Considering that many of the O_3 plumes resulting from NTOCs are spatially heterogeneous and believed to be related to HRVOC emissions, it is important to consider the effect of horizontal grid resolution on hourly O_3 increases. The results from the 1-km resolution sensitivity analysis can be found in the last subsection of Results.

HRVOCs are not explicitly represented in the chemical mechanism. To obtain an estimate, the sum of the Carbon Bond V species ETH (ethene), OLE (olefins), and IOLE (internal olefins) was used.

2.3 Results

Investigation of the regulatory model begins by characterizing the frequency, magnitude, and spatial distribution of predicted NTOCs. In this study, the NTOC is a metric that only indicates a gradient in O_3 concentrations. An O_3 change in a grid cell is described as a NTOC if (1) the change in O_3 from hour to hour is equal to or greater than 40 ppb, or (2) the change in O_3 over 2 hr is equal to or greater than 60 ppb.

The following analysis first quantifies the frequency and magnitude of NTOCs in the 120-day modeling episode from both the regulatory model and surface monitors. The days with a predicted NTOC are then classified as either having an upwind industrial emission or not. Representative days from each classification are then

studied in closer detail and evaluated against observational data from the regulatory monitors. All analysis was restricted to the 2-km modeling domain and all predictions are from the base case emission inventory unless otherwise noted.

2.3.1 Predicted and observed non-typical ozone changes

During the 2005 and 2006 modeling episode, a NTOC was predicted at 672 grid cells on 22 days using the base case EI. In the simulation with the baseline EI, there were 460 grid cells over 17 days that predicted a NTOC. Table 2.2 lists the 22 days in the base case simulation that had a NTOC, and the daily maximum 1-hr and 2-hr O_3 changes for that day. Also listed are the daily maximum 1-hr and 2-hr O_3 changes in the baseline simulation for the same day. The base case simulation predicted a maximum hourly O_3 change of 54 ppb on September 12, 2006, and the baseline simulation predicted a maximum of 50 ppb on October 9 and August 20 of 2006. The maximum predicted change over 2 hr was 76 ppb with the base case simulation and 74 ppb with the baseline. The only difference in these two simulations is the emission inventory, meaning that the differences in frequency and magnitude of NTOCs are the result of the removal of variable emissions. For the remainder of the evaluation, focus shifts to the base case simulations and the 22 days when a NTOC was predicted.

The base case simulation predicted NTOCs for 22 days, and, during the same episode time frame, there were 87 observed NTOCs over 36 days. In these two sets of data, only 9 days had both a predicted and observed NTOC, and they are in boldface in Table 2.2. Thus, the AQM was unable to reproduce the observed phenomenon on 27 of the 36 days. The maximum observed hourly O_3 change was 62 ppb at the TXCT monitor at 10:00 a.m. on June 9, 2006. On this day the base case simulation under predicted the hourly O_3 change at TXCT by 46 ppb and the 1-hr concentration by over 40 ppb. The maximum observed 2-hr change was 95 ppb at the HROC monitor at

	Maximum Predicted O_3 Change (ppb)			
	1-hr		2-hr	
Date	Base Case	Baseline	Base Case	Baseline
September 12, 2006	54	49	66	65
August 1, 2005	**51**	**47**	**76**	**69**
August 17, 2006	**49**	**48**	**72**	**74**
October 9, 2006	49	50	66	65
August 21, 2006	48	44	71	67
October 4, 2006	47	46	64	65
August 5, 2005	**46**	**28**	**64**	**54**
May 26, 2005	**45**	**41**	**71**	**70**
August 3, 2005	45	42	59	57
August 8, 2005	44	37	59	57
June 4, 2006	**44**	**42**	**66**	**64**
June 12, 2006	**44**	**36**	**65**	**53**
May 22, 2005	43	37	64	57
June 3, 2006	43	44	54	55
May 28, 2005	42	41	42	43
August 2, 2005	**42**	**40**	**61**	**57**
August 7, 2005	42	41	62	60
August 18, 2006	**42**	**43**	**64**	**65**
August 20, 2006	42	50	56	61
June 25, 2005	41	39	61	59
August 16, 2006	**40**	**38**	**73**	**67**
August 29, 2006	40	40	60	60

Table 2.2: Simulated maximum 1-hr and 2-hr O_3 changes that met non-typical O_3 change (NTOC) criteria at any grid cell in the 2-km domain using the models base case and baseline emission inventories. NTOC criteria are changes in O_3 concentrations of at least 40 ppb/hr, or 60 ppb/2 hr, in any model grid cell within the 2-km domain. Bold rows indicate that there was also an observed change meeting NTOC criteria at any regulatory monitor on that date.

11:00 a.m. on August 1, 2005. On this day the base case simulation under predicted the 2-hr O_3 change at HROC by 48 ppb, but correctly predicts the 1-hr concentration. Recent analysis from the 2009 Study of Houston Atmospheric Radical Precursors showed that a photochemical box model did not simulate O_3 production rates greater than 35 ppb/hr during high O_3 episodes, though measured rates were often between 40 and 80 ppb/hr (Cazorla et al., 2011), which suggests the under predictions in the regulatory AQM are at least partly due to chemistry.

Distributions of observed daily maximum 8-hr O_3 concentrations at all monitors during the modeling episode time frame are shown in Figure 2.5a. Figure 2.5b shows base case simulated daily maximum 8-hr O_3 concentrations from all grid cells where the monitors are located. The black columns are 8-hr O_3 concentrations from days that had a NTOC, and gray columns show data from days without a NTOC. Similar to the distribution using ten years of data shown in Figure 2.2, the highest frequency of 8-hr values with a NTOC occurred at 88 ppb in the observations. The model predicted 8-hr averages in excess of 140 ppb, though the peak observed 8-hr max was 127 ppb.

During the modeling episode, the DRPK, WALV, and LYNF monitors - all located in the ship channel region - observed the greatest number of NTOCs. August 17, 2006, had the greatest number of monitors (seven) that measured a NTOC, though most days had far fewer NTOC measurements. Approximately 75% of the days had observed NTOCs at three or fewer monitors, and 89% of the days had observed NTOCs at four or fewer monitors. When NTOCs were measured at multiple locations, the monitors were often in close proximity to each other, indicating that NTOCs occur over a small spatial scale.

Figure 2.3b shows the locations and frequency of predicted NTOCs during the 120-day modeling episode. The maximum number of predicted NTOCs for a given grid cell was five; most grid cells had no predicted NTOCs. Simulated NTOCs were most

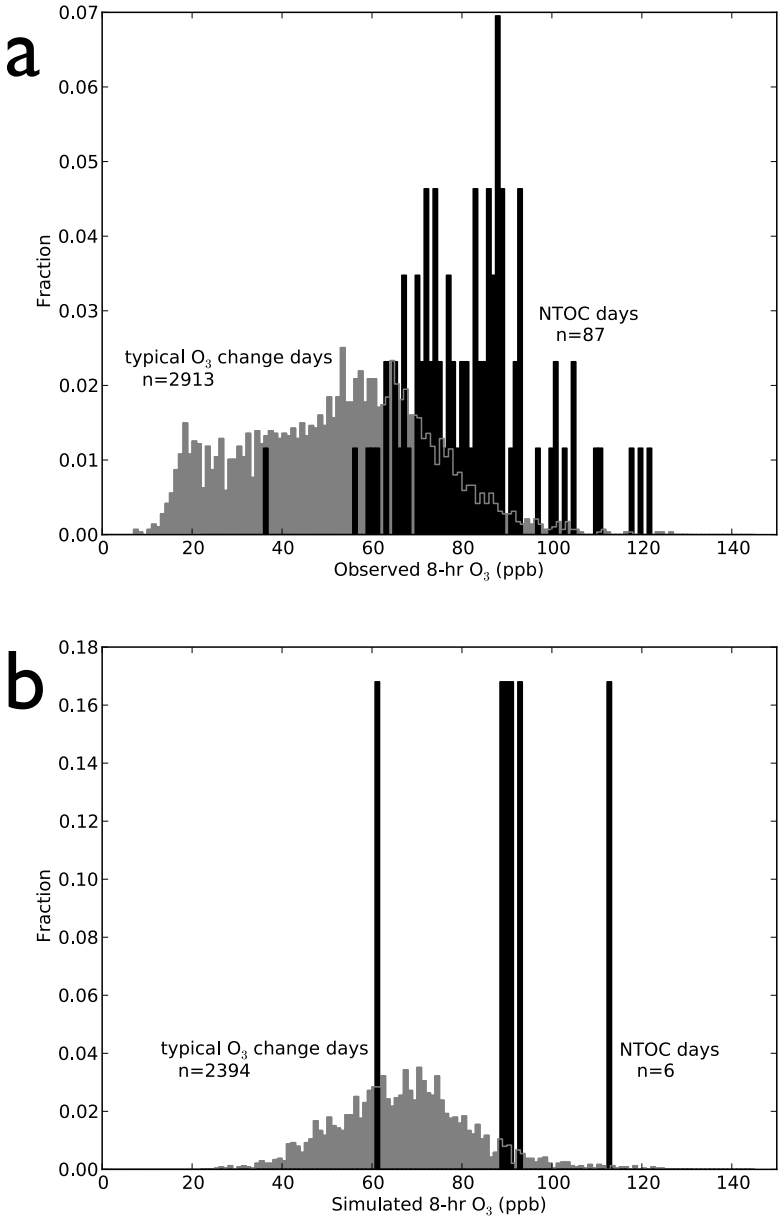

Figure 2.5: Similar to Figure 2.2, but limited to the days during the 120-day modeling episode for the base case simulation. Plot (a) shows distributions of observed daily maximum 8-hr O_3 concentrations at all monitors for days that coincided with the modeling episode (n=3000 monitor-days). The black columns are the concentrations that were measured on days that had a non-typical O_3 change (NTOC), i.e., an observed O_3 change of at least 40 ppb/hr, or 60 ppb/2 hr (n=916 monitor-days). Plot (b) shows distributions of simulated daily maximum 8-hr O_3 concentrations at all grid cells where the regulatory monitors are located (n=2400 grid cell-days). Here, the black columns are concentrations that were predicted on days that had a simulated NTOC. Twenty-four modeling days had incomplete data and are excluded from this plot.

frequent in the ship channel region, which is consistent with measurements shown in Figure 2.3a. At each hour, there may be more than one grid cell with a simulated NTOC. For hours when a NTOC was simulated, the median number of grid cells simulating the NTOC is five. The maximum number of grid cells to predict a NTOC at the same time is 59.

2.3.2 Predicted non-typical ozone changes and industrial emissions

The previous section identified simulation days in the base case when and where a NTOC was predicted. This section investigates whether simulated large industrial emission releases also coincided with a predicted NTOC. In the base case EI, there were six hourly changes of HRVOC emissions in excess of 10,000 mol/hr. Only two of these large increases in HRVOC emissions resulted in a predicted NTOC. The remaining large releases of HRVOCs occurred at night and had little impact on predicted O_3 concentrations.

Only 2 of the 22 days with predicted NTOCs (Table 2.2) also had an upwind release of HRVOCs greater than 10,000 mol/hr. The largest increase in O_3 concentrations resulting from a release was on August 20, 2006. On this day there was a predicted 1-hr increase in HRVOC emissions from 5:00 a.m. to 6:00 a.m. of 32,643 moles. A black "X" in Figure 2.6 marks the location of the emissions increase. The emissions release occurred early in the morning, providing a sufficient number of daylight hours to process and contribute to downwind O_3 formation. Further, the location of the emission release is in the Houston ship channel, a common origin of observed O_3 plumes. This HRVOC release is not included in the baseline EI, thus providing a natural sensitivity run for the release on O_3 concentrations. Ground layer 1-hr O_3 values from the baseline simulation were subtracted from the O_3 values predicted using the base case EI as shown in Figure 2.6. The HRVOC emissions were released

at 6 a.m. (Figure 2.6a) and then carried south where the predicted increase in O_3 concentrations was 25 ppb greater than in the baseline prediction at 8 a.m. (Figure 2.6b) and was spatially limited covering only a few kilometers. This result confirms the model's ability, under the right conditions, to predict an O_3 plume with a limited spatial extent.

The DRPK monitor was the closest monitor to the location of the large O_3 increase, and its location is labeled in Figure 2.6. A time series plot of observed and simulated 1-hr O_3 concentrations is shown in Figure 2.7. The DRPK observations on this day showed a rapid increase from 3 ppb at 6:00 a.m. to 46 ppb in just 2 hr. Predicted values at 8:00 a.m. were 51 ppb with the base case EI and 26 ppb with the baseline EI. The two model runs have nearly identical O_3 predictions except from 6:00 a.m. to 9:00 a.m., which was immediately after the HRVOC release. During those hours, the base case O_3 concentrations are greater than in the baseline simulation. It is clear that model performance improved on this day with the inclusion of the HRVOC release. It is unclear, however, if the measured increase at DRPK was the result of an emission release. Nevertheless, the model is capable of increasing O_3 concentrations under O_3 conducive meteorology if the HRVOC emissions are placed with sufficient magnitude at the right location and time.

2.3.3 Predicted non-typical ozone changes without industrial emissions

There are 20 simulation days with a predicted NTOC and no simulated upwind release of HRVOC emissions greater than 10,000 mol/hr. All 20 days exhibited similar behavior, and two representative days - August 1, 2005, and August 17, 2006 - are analyzed here. On August 1, 2005, the model predicted a NTOC of 51 ppb/hr at 9:00 a.m. in Texas City (southeast of central Houston), and a second NTOC of 46 ppb/hr at 12:00 p.m. near the BAYP monitor. The maximum observed hourly O_3

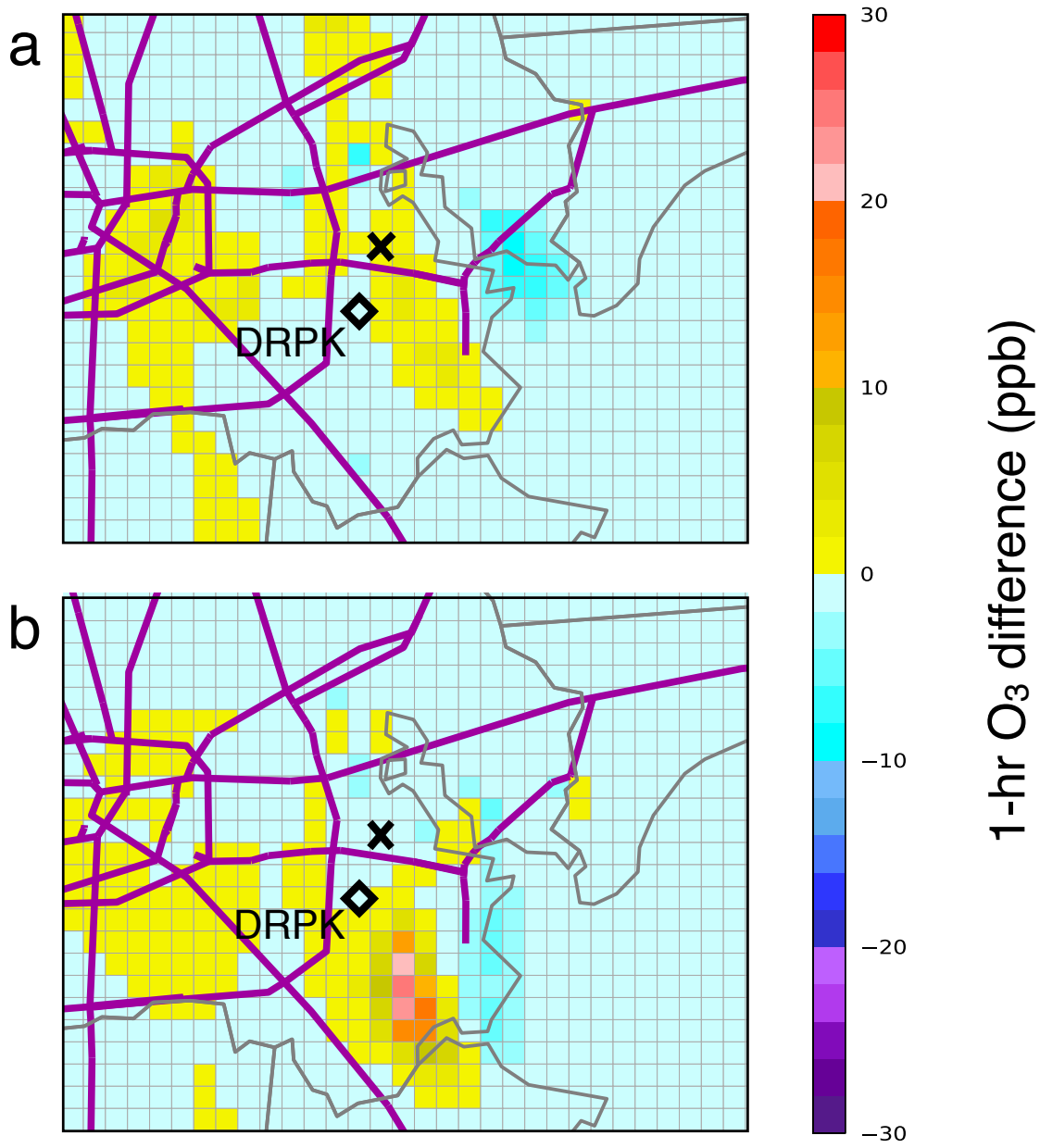

Figure 2.6: Spatial plot showing simulated 1-hr O_3 differences at (a) 6:00 a.m. and (b) 8:00 a.m. on August 20, 2006. The values were obtained by subtracting the baseline O_3 predictions from the base case O_3 predictions. The location of the DRPK monitor is marked by a black diamond. An HRVOC emissions event occurred in the base case EI at 6:00 a.m. in the grid cell marked with a black "X."

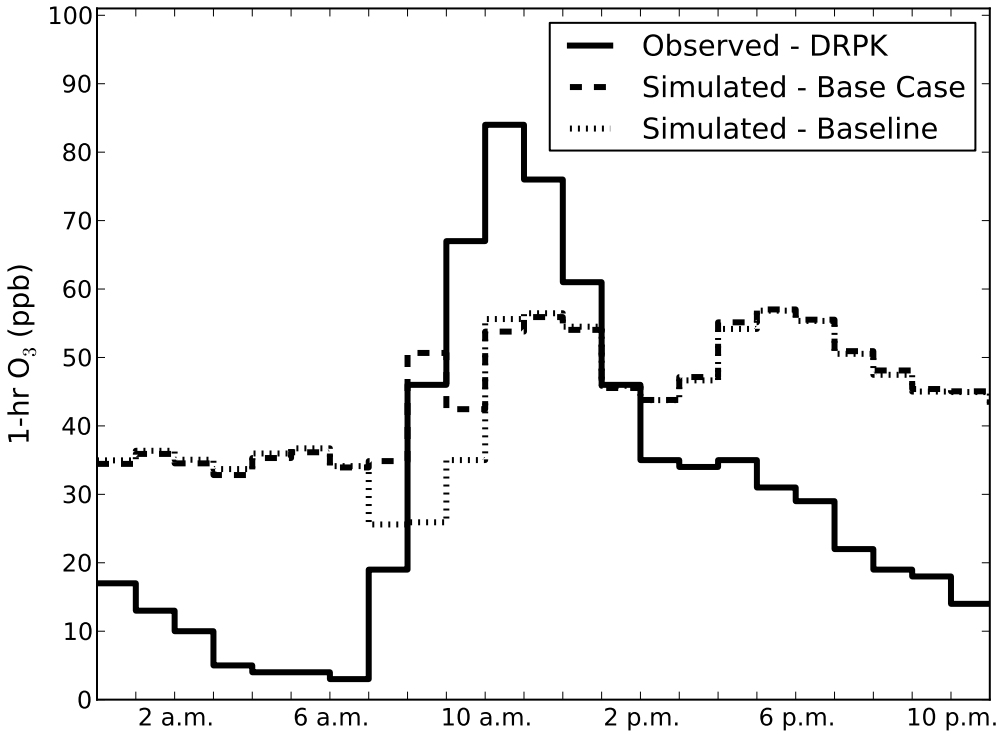

Figure 2.7: Observed and simulated 1-hr O_3 concentrations on August 20, 2006, recorded at the DRPK monitor. Simulated O_3 concentrations are nearly identical for both the base case and baseline simulations except for the 3 hr immediately following the HRVOC release (6:00 a.m.) in the base case simulation.

change for this day was 56 ppb/hr located at BAYP. Figure 2.8 shows, for 9:00 a.m. to 12:00 p.m., the simulated ground layer 1-hr O_3 concentrations (grid cells) for the modeling domain overlaid with measurements from the air quality monitors (diamond markers). A mismatch between the colors of the diamond marker and surrounding grid cells indicates an under or over prediction by the AQM. If no measurement data are available, the marker is a black dot. At 10:00 a.m., a simulated plume of high O_3 greater than 90 ppb covers much of southern Houston, but very few monitors measured values above 90 ppb. By 11:00 a.m., simulated concentrations reach 136 ppb and begin to move westward. Much of southwestern Houston has reached a predicted O_3 value of at least 120 ppb, but only three monitors (CLIN, HROC, and HSMA) measured triple-digit concentrations. Model over predictions continued into the next hour, where predicted concentrations reached 168 ppb. A number of grid cells to the southeast and west of central Houston predicted a NTOC, and they are marked with a black ''X'' in Figure 2.8. The NTOC predictions occurred on the edge of a plume with the highest O_3 values.

On August 1, 2005, at 12:00 p.m., the model predicted 1-hr O_3 concentrations in excess of 120 ppb, but observations show that only the BAYP monitor recorded O_3 levels of that magnitude (Figure 2.8). Figure 2.9a compares observed and simulated O_3 concentrations at 12:00 p.m. for all monitors near downtown Houston that were impacted by the simulated high O_3 plume. The over predictions at HCQA and SHWH are 37 and 56 ppb. The peak observed 1-hr O_3 concentration at BAYP - 140 ppb - came immediately after a 1-hr change of 56 ppb, but the simulated high O_3 at BAYP was not the result of a NTOC; a NTOC was predicted 10 km from the monitor. As shown in Figure 2.9b, the maximum simulated hourly change at BAYP was only 23 ppb. Simulated concentrations over predict measurements by approximately 50 ppb at 10:00 a.m. and 11:00 a.m., but that over prediction is only 10 ppb at 12:00 p.m.

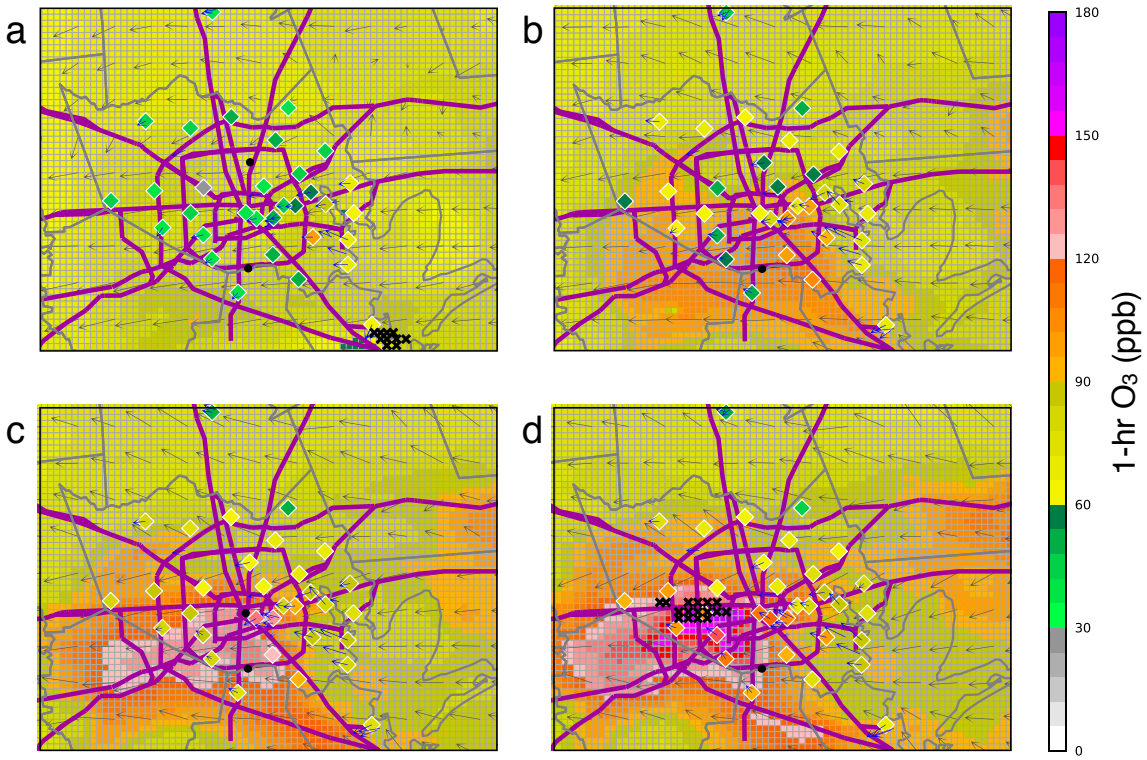

Figure 2.8: Spatial plot showing predictions from the base case simulation of 1-hr O_3 concentrations at (a) 9:00 a.m., (b) 10:00 a.m., (c) 11:00 a.m., and (d) 12:00 p.m. on August 1, 2005. The diamond markers show measurement data from air quality monitors; if no data are available, the marker is a black dot. Color mismatches between the diamond markers (measurements) and grid cells (simulations) indicate model over or under predictions. Gray arrows show the simulated wind vectors at select grid cells. Arrows originating at the center of a diamond marker show measured wind data. Simulated NTOCs are marked with a black "X" (9:00 a.m. and 12:00 p.m. only).

after the observed 1-hr increase of 56 ppb.

When the regulatory AQM does make a prediction that meets some of the NTOC criteria at a monitor, it does so over a large spatial area and does not reproduce the observed limited spatial scale of high O_3 seen in monitor measurements. For example, Figure 2.10 shows for August 17, 2006, the model predicted values from a grid cell 5 km from the DRPK monitor. Figure 2.10 shows that model predictions had similar changes in hourly concentrations and nearly matched the peak 1-hr O_3 measured at the DRPK monitor. The model does not, however, reproduce the narrow spatial extent of high O_3 as observed by the monitors. As shown in Figure 2.11a, the model predicts a high O_3 plume in the southern part of the Houston urban core at 2:00 p.m., causing over predictions at the majority of the monitors in that region. Figure 2.11b shows the amount of over prediction at 2:00 p.m. at five regulatory monitors. Although the model predictions match peak measurements at the HSMA monitor, the model over predicts O_3 concentrations at all other monitors and by more than 40 ppb at the SHWH monitor. On this day the model is able to reproduce observed phenomena at two monitors, but does so over too large a spatial extent. For many of the days where an observed NTOC is measured at a monitor, the model does not reproduce the hourly values or the limited spatial extent of the observed high O_3.

These data show that the model can make high O_3, but the causes in the model are likely not the same causes for producing high O_3 in the observations. The cause of highest O_3 in the observations is spatially and temporally limited, and not like those predicted by the model.

2.3.4 Effect of horizontal grid resolution on non-typical ozone changes

Maximum 1- and 2-hr O_3 changes were 65 ppb/hr and 78 ppb/ 2 hr when the model was rerun with the nested 1-km subdomain. Compared with the 2-km subdomain

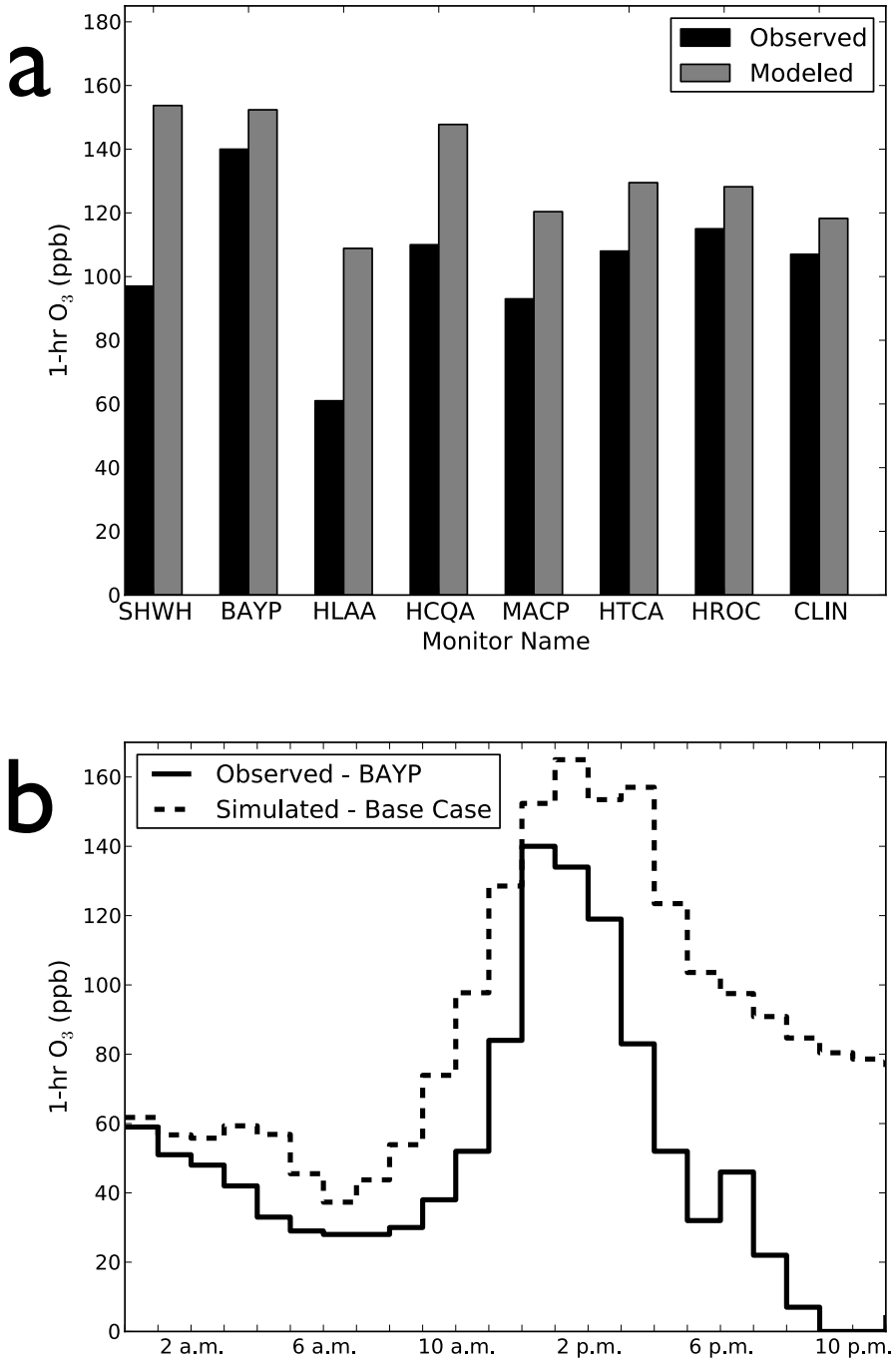

Figure 2.9: (a) Observed and simulated (base case EI) 1-hr O_3 concentrations at 12:00 p.m. on August 1, 2005. (b) Observed and simulated (base case EI) 1-hr O_3 concentrations on August 1, 2005, recorded at the BAYP monitor. A 1-hr increase of 56 ppb was measured at 12:00 p.m.

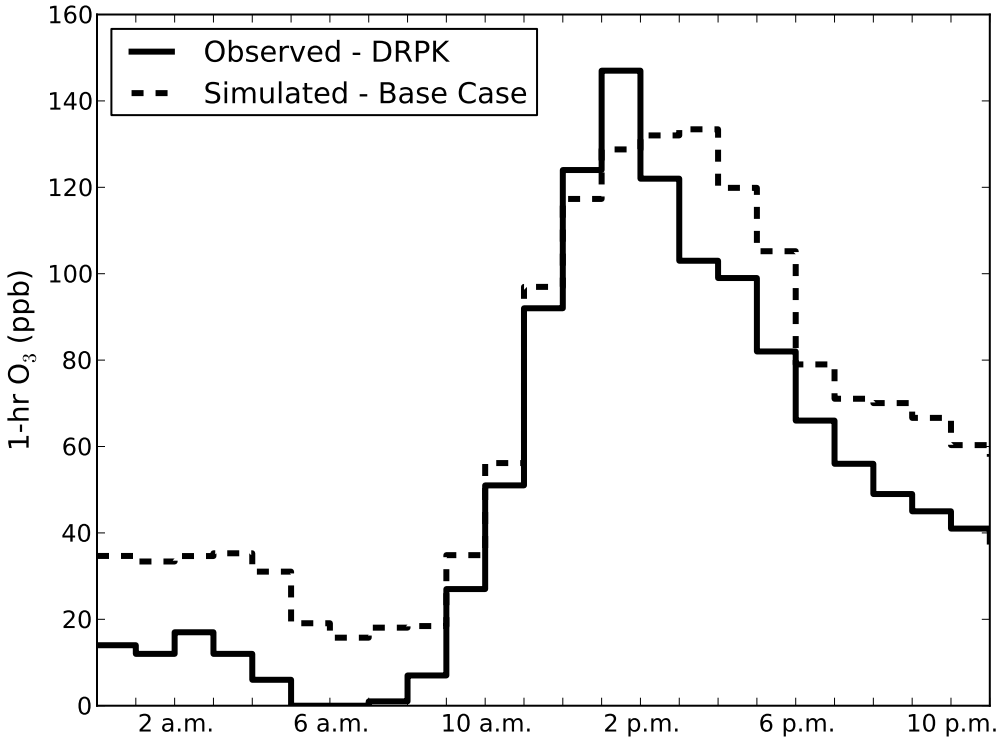

Figure 2.10: Observed and simulated (base case EI) 1-hr O_3 concentrations on August 17, 2006. Observations were recorded at the DRPK monitor. Simulated values were extracted from a grid cell 5 km away from DRPK. A NTOC was measured and simulated at 11:00 a.m.

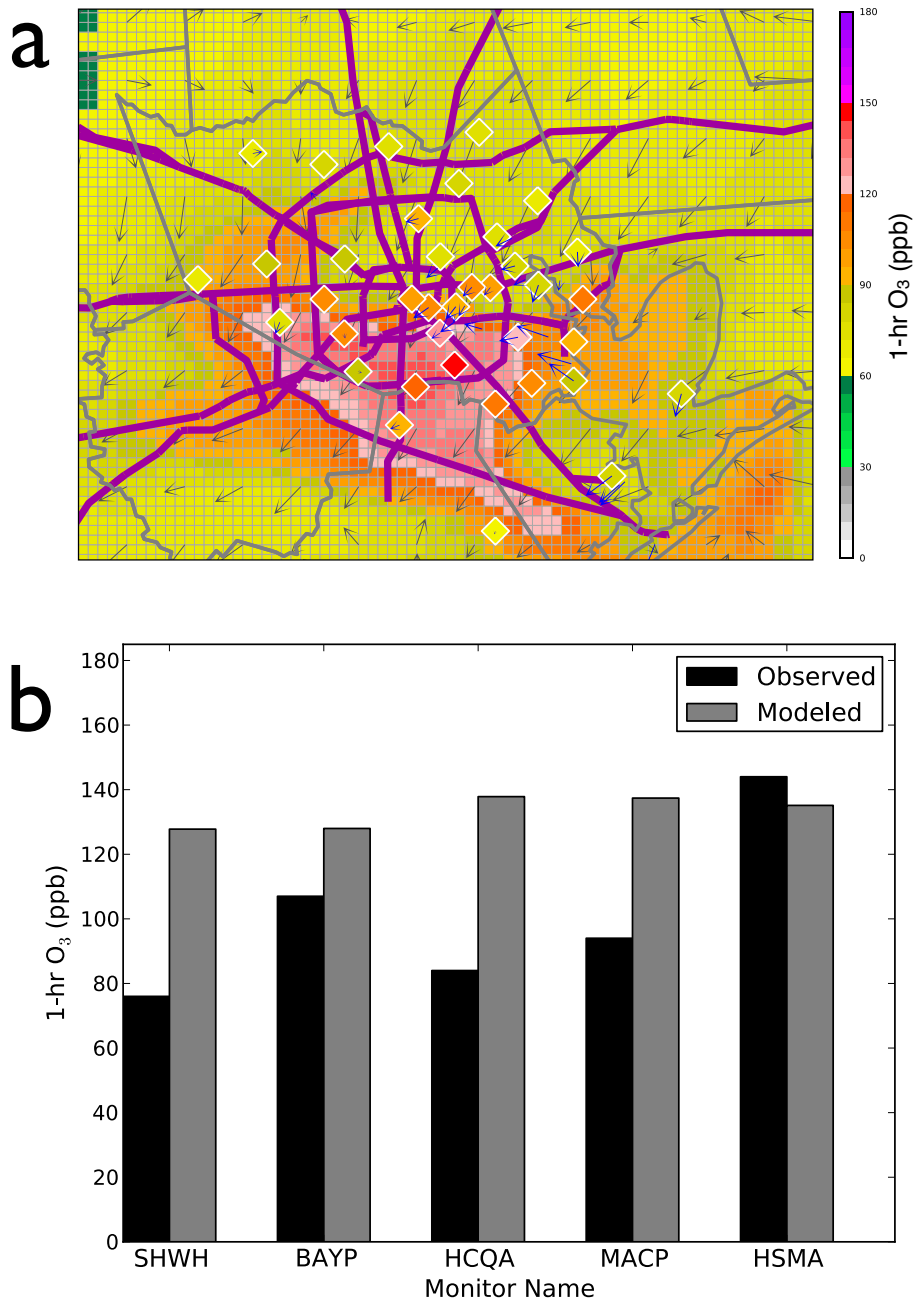

Figure 2.11: Plot (a) is a spatial plot showing simulated (base case EI) 1-hr O_3 concentrations at 2:00 p.m. on August 17, 2006. The diamond markers show measurement data from air quality monitors. Color mismatches between the diamond markers (measurements) and grid cells (simulations) indicate model over or under predictions. Gray arrows show the simulated wind vectors at select grid cells. Arrows originating at the center of a diamond marker show measured wind data. Plot (b) shows observed and simulated (base case EI) 1-hr O_3 concentrations for select monitors.

simulation, the maximum 1-hr change increased by 20% (11 ppb) and the maximum 2-hr change increased by 3% (2 ppb). Grid resolution, therefore, impacts the magnitude of hourly O_3 increases. Although the 2-km subdomain is generally considered to be finely resolved, it may be too coarse to simulate the magnitude of the observed NTOC phenomenon.

It was shown in the previous section that the model failed to predict the spatially limited O_3 plume on August 17, 2006, with the 2-km subdomain. Model simulations using the 1-km subdomain similarly show a large O_3 plume over southern Houston. The persistence of such over predictions suggests that horizontal grid resolution is likely not causing problems with spatial heterogeneity.

2.4 Conclusion

Analysis of Houston O_3 monitoring data from 2000 to 2009 shows that on days when a monitor observed a NTOC, that monitor was also more likely to exceed the 8-hr O_3 NAAQS. Thus, identifying the conditions and sources that produce a NTOC is critical to controlling O_3 violations. The regulatory AQM used to support the 2010 SIP did not reproduce observed behavior on most NTOC days and often under predicted the hourly O_3 change. Simulations also failed to capture the limited spatial extent of high O_3 found on NTOC days. On these days, the AQM often predicted high O_3 concentrations over large regions of Houston, resulting in over predictions at many of the monitors. Thus, a more accurate reproduction of extreme measured behavior at a handful of monitors came at the cost of misrepresenting observations elsewhere. It is important to note that this result is not considered detrimental in the current EPA attainment guidance.

Prior to 2007, the EPA required the use of observations and model predictions under the assumption that simulations were capable of reproducing the specific

observed phenomena. After 2007, the attainment guidance now assumes that models only need to be capable of reproducing a change in ozone concentrations due to changes in precursor emissions, without necessarily reproducing the measurements accurately. In the current approach, the model's predicted change is applied to the baseline simulations to predict a future case. It is still the assumption, however, that the model with its inputs is able to simulate the critical processes driving poor air quality. If random emissions processes are indeed driving these large hourly changes in concentrations, then it is unrealistic to expect a deterministic modeling episode of just 120 days to represent this process accurately. This is especially true if the observational metrics used by the attainment process are averages of observations taken over a 5-year time period.

A necessary next step is to perform a meteorological analysis similar to the studies described above (Byun et al., 2007; Vizuete et al., 2009). It is important to understand the regional meteorology that was present on NTOC days, because high O_3 in Houston is known to be dependent upon wind fields. Understanding whether winds on NTOC days are dissimilar from winds on typical days, and whether modeled winds closely match measurements, will provide key pieces of evidence for determining the cause(s) of NTOCs and model deficiencies. There is also a need for back-trajectory analysis on NTOC days to determine if air parcels that impacted ground monitors passed over industrial facilities.

The modeling presented here was performed by the TCEQ as a requirement of the O_3 attainment process. This model was used to develop and defend future pollution controls and thus represents a real-world application of regulatory modeling. The goal of this study was not to ''fix'' the model's deficiency, but rather to evaluate model performance in an actual regulatory application. It is clear that there is an observed phenomenon in Houston whose cause may not be addressed by current EPA

guidance. Once the cause is better understood, a dual approach could be proposed that would address NTOC phenomena separately from the EPA guidance. Such a dual approach has already been used in Houston and served as the technical foundation of the successful 2004 Houston 1-hr O_3 SIP (Texas Commission on Environmental Quality, 2004). In this SIP, random industrial emission events were addressed with targeted controls, and the regulatory model was used to formulate policy (e.g., NO_x and HRVOC cap and trade programs, reductions of industrial NO_x, mobile source reductions) for the remaining causes of violations. More recently, it has been suggested that peak O_3 may be responsive initially to targeted ship channel VOC emissions, but further O_3 reductions may require NO_x limits (Xiao et al., 2010). This dual approach proved to be effective in reducing ozone before and could be applied in current SIP efforts.

REFERENCES

R. M. Banta, C. J. Senff, J. Nielsen-Gammon, L. S. Darby, T. Ryerson, J. Alvarez, S. Sandberg, E. Williams, and M. Trainer (2005). A bad air day in Houston. *Bull. Am. Meteorol. Soc.*, 86(5):657--669. doi:10.1175/BAMS-86-5-657.

D. W. Byun, S. T. Kim, and S. B. Kim (2007). Evaluation of air quality models for the simulation of a high ozone episode in the Houston metropolitan area. *Atmos. Environ.*, 41:837--853. doi:10.1016/j.atmosenv.2006.08.038.

M. Cazorla, W. H. Brune, X. Ren, and B. Lefer (2011). Direct measurement of ozone production rates in Houston in 2009 and comparison with two estimation methods. *Atmos. Chem. Phys. Discuss.*, 11:27521--27546. doi:10.5194/acpd-11-27521-2011.

E. Cowling, C. Furiness, B. Dimitriades, and D. Parrish (2007). Final rapid science synthesis report: Findings from the second Texas Air Quality study (TexAQS II) - Final report to the Texas Commission on Environmental Quality. TCEQ Contract Number 582-4-65614. http://aqrp.ceer.utexas.edu/docs/RSSTFinalReportAug31.pdf.

B. H. Czader, D. W. Byun, S. T. Kim, and W. Carter (2008). A study of VOC reactivity in the Houston-Galveston air mixture utilizing an extended version of SAPRC-99 chemical mechanism. *Atmos. Environ.*, 42:5733--5742. doi:10.1016/j.atmosenv.2008.01.039.

ENVIRON International Corporation (2008). CAMx Users Guide: Comprehensive Air Quality Model with Extensions, version 4.50. Novato, CA: ENVIRON International Corporation.

F. Gan and P. K. Hopke (2003). Data mining of the relationship between volatile organic compounds and transient high ozone formation. *Anal. Chim. Acta*, 490:153--158. doi:10.1016/S0003-2670(03)00497-5.

B. H. Henderson, H. E. Jeffries, B. U. Kim, and W. Vizuete (2010). The influence of model resolution on ozone in industrial volatile organic compound plumes. *J. Air Waste Manag. Assoc.*, 60:1105--1117. doi:10.3155/1047-3289.60.9.1105.

J. M. Jones, C. Hogrefe, R. F. Henry, J. Y. Ku, and G. Sistla (2005). An assessment of the sensitivity and reliability of the relative reduction factor approach in the development of 8-hr ozone attainment plans. *J. Air Waste Manag. Assoc.*, 55:13--19.

L. I. Kleinman, P. H. Daum, D. Imre, Y. N. Lee, L. J. Nunnermacker, S. R. Springston, J. Weinstein-Lloyd, and J. Rudolph (2002). Ozone production rate and hydrocarbon reactivity in 5 urban areas: A cause of high ozone concentration in Houston. *Geophys. Res. Lett.*, 29:1467. doi:10.1029/2001GL014569.

B. J. McCoy, P. S. Fischbeck, and D. Gerard (2010). How big is big? How often is often? Characterizing Texas petroleum refining upset air emissions. *Atmos. Environ.*, 44:4230--4239. doi:10.1016/j.atmosenv.2010.07.088.

C. F. Murphy and D. T. Allen (2005). Hydrocarbon emissions from industrial release events in the Houston-Galveston area and their impact on ozone formation. *Atmos. Environ.*, 39:3785--3798. doi:10.1016/j.atmosenv.2005.02.051.

F. Ngan and D. Byun (2011). Classification of weather patterns and associated trajectories of high-ozone episodes in the Houston-Galveston-Brazoria area during the 2005/06 TexAQS-II. *J. Appl. Meteorol. Climatol.*, 50:485--499. doi:10.1175/2010jamc2483.1.

T. B. Ryerson, M. Trainer, W. M. Angevine, C. A. Brock, R. W. Dissly, F. C. Fehnsenfeld, G. J. Frost, P. D. Goldan, J. S. Holloway, G. Hubler, R. O. Jakoubek, W. C. Kuster, J. A. Neuman, D. K. Nicks, Jr., D. D. Parrish, J. M. Roberts, D. T. Sueper, E. L. Atlas, S. G. Donnelly, F. Flocke, A. Fried, W. T. Potter, S. Schauffler, V. Stroud, A. J. Weinheimer, B. P. Wert, C. Wiedinmyer, R. J. Alvarez, R. M. Banta, L. S. Darby, and C. J. Senff (2003). Effect of petrochemical industrial emissions of reactive alkenes and NOx on tropospheric ozone formation in Houston, Texas. *J. Geophys. Res. Atmos.*, 108:4249. doi:10.1029/2002JD003070.

G. Sistla, C. Hogrefe, W. Hao, J. Y. Ku, E. Zalewsky, R. F. Henry, and K. Civerolo (2004). An operational assessment of the application of the relative reduction factors in demonstration attainment of the 8-hr ozone National Ambient Air Quality Standard. *J. Air Waste Manag. Assoc.*, 54:950--959.

Texas Commission on Environmental Quality (2004). Revisions to the State Implementation Plan (SIP) for the control of ozone air pollution: Houston/Galveston/Brazoria ozone nonattainment area. Austin, TX. Project No. 2004-042-SIP-NR.

Texas Commission on Environmental Quality (2010a). Houston-Galveston-Brazoria 8-hour ozone SIP modeling (2005/2006 episodes). http://www.tceq.texas.gov/airquality/airmod/data/hgb8h2 (accessed October 10, 2009).

Texas Commission on Environmental Quality (2010b). Ozone data. http://www.tceq.texas.gov/agency/data/ozone_data.html (accessed April 28, 2010).

Texas Commission on Environmental Quality (2010c). Revisions to the State Implementation Plan for the control of ozone air pollution: Houston-Galveston-Brazoria ozone nonattainment area. Austin, TX. Project No. 2009-017-SIP-NR.

U.S. Environmental Protection Agency (2007). Guidance on the use of models and other analyses for demonstrating attainment of air quality goals for O_3, PM and regional haze. EPA-454/B-07-002. Washington, DC: U.S. Environmental Protection Agency.

W. Vizuete, L. Biton, H. E. Jeffries, and E. Couzo (2010). Evaluation of relative response factor methodology for demonstrating attainment of ozone in Houston, Texas. *J. Air Waste Manag. Assoc.*, 60:838--848. doi:10.3155/1047-3289.60.7.838.

W. Vizuete, H. E. Jeffries, T. W. Tesche, E. P. Olaguer, and E. Couzo (2011). Issues with ozone attainment methodology for Houston, TX. *J. Air Waste Manag. Assoc.*, 61:238--253. doi:10.3155/1047-3289.61.3.238.

W. Vizuete, H. E. Jeffries, A. Valencia, E. Couzo, E. Christoph, J. Wilkinson, B. Henderson, H. Parikh, and J. Kolling (2009). HARC Project H97: Multi-model, multi-episode process analysis to investigate ozone formation and control sensitivity in the 2000/2005/2006 Houston SIP episode models. The Woodlands, TX: Houston Advanced Research Center. http://projects.tercairquality.org/AQR/H097.

W. Vizuete, B. U. Kim, H. E. Jeffries, Y. Kimura, D. T. Allen, M. A. Kioumourtzoglou, L. Biton, and B. Henderson (2008). Modeling ozone formation from industrial emission events in Houston, Texas. *Atmos. Environ.*, 42:7641--7650. doi:10.1016/j.atmosenv.2008.05.063.

M. Webster, J. Nam, Y. Kimura, H. E. Jeffries, W. Vizuete, and D. T. Allen (2007). The effect of variability in industrial emissions on ozone formation in Houston. *Atmos. Environ.*, 41:9580--9593. doi:10.1016/j.atmosenv.2007.08.052.

B. P. Wert, M. Trainer, A. Fried, T. B. Ryerson, B. Henry, W. Potter, W. M. Angevine, E. Atlas, S. G. Donnelly, F. C. Fehnsenfeld, G. J. Frost, P. D. Goldan, A. Hansel, J. S. Holloway, G. Hubler, W. C. Kuster, D. K. Nicks, Jr., J. A. Neuman., D. D. Parrish, S. Schauffler, J. Stutz, D. T. Sueper, C. Wiedinmyer, and A. Wisthaler (2003). Signatures of terminal alkene oxidation in airborne formaldehyde measurements during TexAQS 2000. *J. Geophys. Res. Atmos.*, 108(D3):4104. doi:10.1029/2002JD002502.

X. Xiao, D. S. Cohan, D. W. Byun, and F. Ngan (2010). Highly nonlinear ozone formation in the Houston region and implications for emission controls. *J. Geophys. Res. Atmos.*, 115(D23309). doi:10.1029/2010JD014435.

CHAPTER 3
HOUSTON'S RAPID OZONE INCREASES: PRECONDITIONS AND GEOGRAPHIC ORIGINS[1]

3.1 Introduction

In 2004, the Texas Commission on Environmental Quality (TCEQ) proposed a novel emissions control strategy to address ozone (O_3) pollution in Houston (Texas Commission on Environmental Quality, 2004). This strategy placed limits on emissions of ethene, propene, 1,3-butadiene and butene isomers, collectively called highly reactive volatile organic compounds (HRVOCs), which are released from petrochemical facilities in the industrial ship channel region. The TCEQ's analysis of Houston's O_3 problem - detailed in their 2004 State Implementation Plan (SIP) - showed that many of the highest O_3 peaks were measured following brief periods of concentration increases greater than 40 ppb/hr and sometimes greater than 100 ppb/hr (Texas Commission on Environmental Quality, 2004). These large increases were associated with reactive plumes of HRVOC emissions measured by aircraft in several studies during the Texas Air Quality Study field campaign in 2000 (Kleinman et al., 2002; Daum et al., 2003; Ryerson et al., 2003). The TCEQ's proposed HRVOC emissions controls limited both routine emissions and short-term, or ''upset,'' releases at facilities with the potential to emit more than 10 tons ($\sim$ 9.07 Mg) of HRVOCs per year. Exempting all but the largest industrial facilities assumed that smaller HRVOC sources do not have a large

[1]E. Couzo, H.E. Jeffries, W. Vizuete, Houston's rapid ozone increases: preconditions and geographic origins. *Environ. Chem.* **2013**, 10, 260-268, doi: 10.1071/EN13040.

This is the pre-publication version of an article that appears in *Environmental Chemistry*, 2013, copyright CSIRO, available online at: http://www.publish.csiro.au/?paper=EN13040. The article has been reformatted to meet the dissertation standards of the UNC graduate school.

effect on rapid O_3 production. The Environmental Protection Agency approved the TCEQ's SIP, and the emissions controls became Texas state law in 2005.

The 2004 SIP highlighted the significance of rapid O_3 increases to violations of the 1-hr federal standard, but these increases also contribute greatly to violations of the 8-hr O_3 standard. Many of Houston's highest 8-hr O_3 peaks are characterized by sudden increases in concentrations of at least 40 ppb in 1 hr, or 60 ppb in 2 hr (Vizuete et al., 2011). Measurements from 2000 to 2009 show that these increases, called non-typical O_3 changes (NTOCs), increase the likelihood of a monitor violating the 1997 0.08-ppm 8-hr O_3 standard (Couzo et al., 2012). Nearly 60% of days with NTOC measurements violated the 8-hr O_3 standard, but just 1% of typical O_3 days exceeded the federal limit.

The cause(s) of every NTOC is an open question, but evidence linking them to HRVOC emissions has accumulated since the TCEQ's 2004 SIP (Daum et al., 2004; Berkowtiz and Doskey, 2005; Washenfelder et al., 2010). Speciated hydrocarbon measurements found ethene and propene among the most likely VOCs to contribute significantly to rapid O_3 production (Gan and Hopke, 2003). A recent study found that some chemical flares operate at combustion and destruction efficiencies lower than required by regulation, and that these flares are significant sources of alkenes (Wood et al., 2012). Furthermore, it is known that large-scale, short-term HRVOC emissions from industrial sources occur often and with notable temporal variability in Houston (Wert et al., 2003; Murphy and Allen, 2005; Cowling et al., 2007; Webster et al., 2007; de Gouw et al., 2009; McCoy et al., 2010). It is these emissions, in addition to routine HRVOC emissions, that the TCEQ primarily targeted in 2004. Unfortunately, emission upsets are not predictable, and the emissions event database maintained by the TCEQ (http://www11.tceq.texas.gov/oce/eer/index.cfm, accessed October 23, 2012) contains reports from facilities that are often just best estimates of the VOC

releases. At any single facility, HRVOC upsets are rare, and it has been difficult to link specific NTOCs to reported emissions upsets. Although HRVOC emissions and NTOCs have received increased attention, there has not been a comprehensive effort to look at all NTOCs over a long time frame. The studies mentioned above have generally had short windows of data collection corresponding with field campaigns. The limited spatial and temporal scales of most field campaigns reduce the chance of measuring a NTOC and tracing it back to a particular emission event.

The number of ground monitors in Houston has increased since the early 2000s when the NTOC phenomenon was first observed. In 2000, for example, there were 14 monitors and a total of 218 NTOCs measured. By 2011, the number of NTOCs dropped to 39, although the number of monitors increased to 25. The frequency and magnitude of NTOCs have declined markedly despite this increase in spatial coverage. The most dramatic declines occurred just after the TCEQ implemented targeted HRVOC controls for short-term and routine emissions. NO_x and mobile source reductions also took effect during this period, however, so it is difficult to disentangle the benefits directly attributable to the HRVOC controls. Notwithstanding the improvements, NTOCs still occur in Houston at monitors that have yet to achieve the 2008 0.075-ppm 8-hr O_3 standard. One possible explanation is that the smaller industrial facilities that were exempted from the 2004 HRVOC limits do, in fact, contribute to the NTOC problem. Other potential causes could be meteorological. Air mass recirculation, a stalled sea breeze and entrainment from a rapidly rising planetary boundary layer are all possible explanations for NTOCs. A closer examination of the problem and the factors that lead to NTOC formation is required.

This work considers local meteorological conditions and ambient pollutant concentrations in an attempt to determine the necessary preconditions for the large hourly O_3 increases found in the observational record. The data used in this study date back to

2000, which provides a wide time frame during a dynamic period in which aggressive emission control strategies were implemented. This provides built-in observational sensitivity experiments to help understand how varying meteorological conditions and industrial emissions affect NTOCs. Using over ten years of measurement data, we have identified candidate days with unusually large hourly O_3 increases. We combine wind field measurements with pollutant observations from a dense network of ground station monitors to determine the necessary conditions and likely geographic origins of the NTOCs. Our analysis examines the assumption made in the TCEQ's 2004 SIP - that HRVOC emissions are responsible for many NTOCs and O_3 violations. Ultimately, a description of the conditions that can lead to NTOCs may help environmental regulators develop effective control strategies that efficiently bring ambient O_3 levels in Houston below the federal standard.

3.2 Experimental

Twenty-five ground station monitors were used in this study, and they are listed in Table 3.1 with their official names, four-letter abbreviation, Continuous Ambient Monitoring Station (CAMS) number, Aerometric Information Retrieval System (AIRS) number and measured parameters. These are the same monitors that were used in the TCEQ's 2010 SIP. Monitor locations are shown in Figure 3.1. Each of these monitors measures a variety of chemical (e.g. O_3, SO_2) and meteorological parameters (e.g. wind speed, wind direction) with a time resolution of 1 hr. The red star marks the Sam Houston Tollway Bridge, which is approximately the center of the ship channel region. These data are maintained by the TCEQ and are available publicly (http://www.tceq.texas.gov/airquality/monops/hourly_data.html, accessed January 13, 2013). The data record spans 2000-2011, although not all monitors have data that begins in 2000.

Monitor Name	Abbreviation	CAMS No.	AIRS No.	
Bayland Park	BAYP	53	48-201-0055	O_3, CH_2O, ws/wd
Clinton	CLIN	403	48-201-1035	O_3, SO_2, ws/wd
Conroe Relocated	CNRt	78	48-339-0078	O_3, ws/wd
Danciger	DNCG	618	48-039-0618	O_3, ws/wd
Deer Park	DRPK	35	48-201-1039	O_3, CH_2O, ws/wd
Galveston	GALC	34	48-167-0014	O_3, ws/wd
HRM-3 Haden Road	H03H	603	48-201-0803	O_3, ws/wd
Aldine	HALC	8	48-201-0024	O_3, ws/wd
Channelview	HCHV	15	48-201-0026	O_3, CH_2O, ws/wd
Croquet	HCQA	409	48-201-0051	O_3, SO_2, ws/wd
Lang	HLAA	408	48-201-0047	O_3
Northwest Harris County	HNWA	26	48-201-0029	O_3, ws/wd
Houston East	HOEA	1	48-201-1034	O_3, ws/wd
Houston Regional Office	HROC	81	48-201-0070	O_3, SO_2, ws/wd
Monroe	HSMA	406	48-201-0062	O_3, SO_2
Texas Avenue	HTCA	411	48-201-0075	O_3
North Wayside	HWAA	405	48-201-0046	O_3, SO_2
Lake Jackson	LKJK	1016	48-039-1016	O_3, ws/wd
Lynchburg Ferry	LYNF	1015	48-201-1015	O_3, ws/wd
Manvel Croix Park	MACP	84	48-039-1004	O_3, ws/wd
Mustang Bayou	MSTG	619	48-039-0619	O_3, ws/wd
Seabrook Friendship Park	SBFP	45	48-201-1050	O_3, SO_2, ws/wd
Westhollow	SHWH	410	48-201-0066	O_3, ws/wd
Texas City	TXCT	620	48-167-0056	O_3, ws/wd
Wallisville	WALV	617	48-201-0617	O_3, ws/wd

Table 3.1: Air quality monitors and measured parameters. AIRS, Aerometric Information Retrieval System; CAMS, Continuous Ambient Monitoring Station. Measurement abbreviations are O_3, ozone; CH_2O, formaldehyde; SO_2, sulfur dioxide; ws/wd, wind speed and wind direction

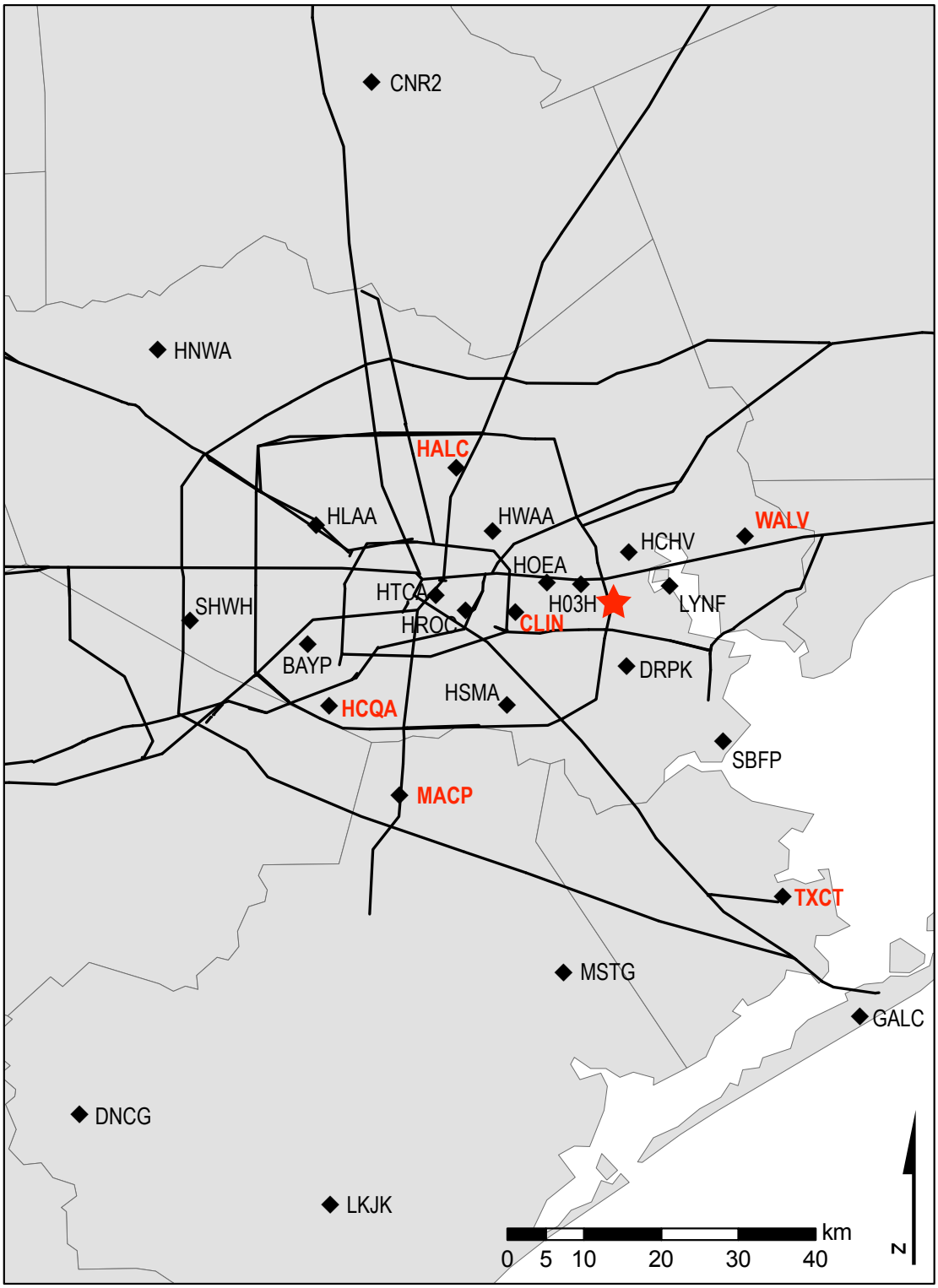

Figure 3.1: The locations and abbreviations of the 25 ground monitoring stations used in this study. The ship channel region is marked with a red star. The six monitors shown in Figure 3.2 are labeled with red text.

Hourly CH_2O concentrations for three monitors are available for select days from 2003 to 2011. CH_2O values were reported from 6 a.m. to 8 a.m. and 1 p.m. to 3 p.m. These data were obtained from the EPA's Air Quality System (http://www.epa.gov/ttn/airs/airsaqs/, accessed April 1, 2012), which is a repository for ambient air quality data.

A NTOC is defined as an increase in O_3 concentrations of at least 40 ppb in 1 hr, or 60 ppb in 2 hr. This definition is consistent with our earlier work on NTOCs (Vizuete et al., 2011; Couzo et al., 2012).

3.3 Results

This study analyzed local wind conditions and concentrations of O_3, CH_2O, and SO_2. The following subsections - meteorology, formaldehyde, and sulfur dioxide - show our analysis of each parameter and how it relates to O_3 and NTOCs.

3.3.1 Meteorological analysis

Couzo et al. (2012) found that most NTOCs are measured at monitors near the ship channel. In Figure 3.2, we expand on that finding. These plots show the wind speed and direction that were measured during NTOCs between 2000 and 2011. Each black marker shows a unique event, so the figure also shows the number of NTOCs that were observed at each monitor. These six monitors (CLIN, HALC, HCQA, MACP, TXCT and WALV) were chosen because they represent a full range of geographic diversity in Houston. CLIN is on the western end of the ship channel and near downtown, WALV is north-east of the ship channel and far from downtown, HALC is north-west of the ship channel and north of downtown, HCQA and MACP are southwest of the ship channel and south of downtown, and TXCT is south of the ship channel and far from downtown. Although there is some scatter in each plot, the NTOC data generally

show strong preference for a narrow range of wind directions. The black markers are clustered in the direction of the ship channel, which indicates NTOCs almost always occur when winds are blowing from Houston's industrial center to the monitor. The red arrow points toward the red star in Figure 3.1 and, thus, shows the direction of the ship channel relative to each monitor. The grey markers in Figure 3.2 show the wind speed and direction that were measured at the time of peak 1-hr O_3 levels on all days. Only data from April to October is shown here. These data do not cluster in the direction of the ship channel meaning that peak O_3 comes from a diversity of directions. In some cases (e.g. HALC and HCQA), peak O_3 levels often occur when the monitor is upwind of the ship channel.

The histograms in Figure 3.2 show the distribution of peak 1-hr O_3 levels on typical days (grey) and NTOC days (black) for all available data during the O_3 season (April - October) from 2000 to 2011. The distributions show that peak 1-hr O_3 levels on NTOC days are shifted towards higher concentrations.

Meteorology is also a critical component of O_3 formation in Houston. The meteorological conditions necessary for high O_3 levels are well known. They have been described in detail and are characterized at surface monitors by low wind speeds and a rotational wind field (Cowling et al., 2007; Banta et al., 2005; Ngan and Byun, 2011). Despite the unquestionable importance of meteorology on O_3 formation, an analysis of winds and 8-hr O_3 violations in Houston determined that O_3-conducive meteorological conditions are necessary but insufficient to produce high O_3 levels and NTOCs (Vizuete et al., 2009).

NTOCs tend to happen under stagnant or near-stagnant conditions. This is also true for typical high O_3 levels. Distributions of 3-hr average wind speed are shown in Figure 3.3 for NTOC days (left), days that violated the 1997 0.08-ppm 8-hr O_3 standard (middle) and days that did not violate the standard (right). To obtain

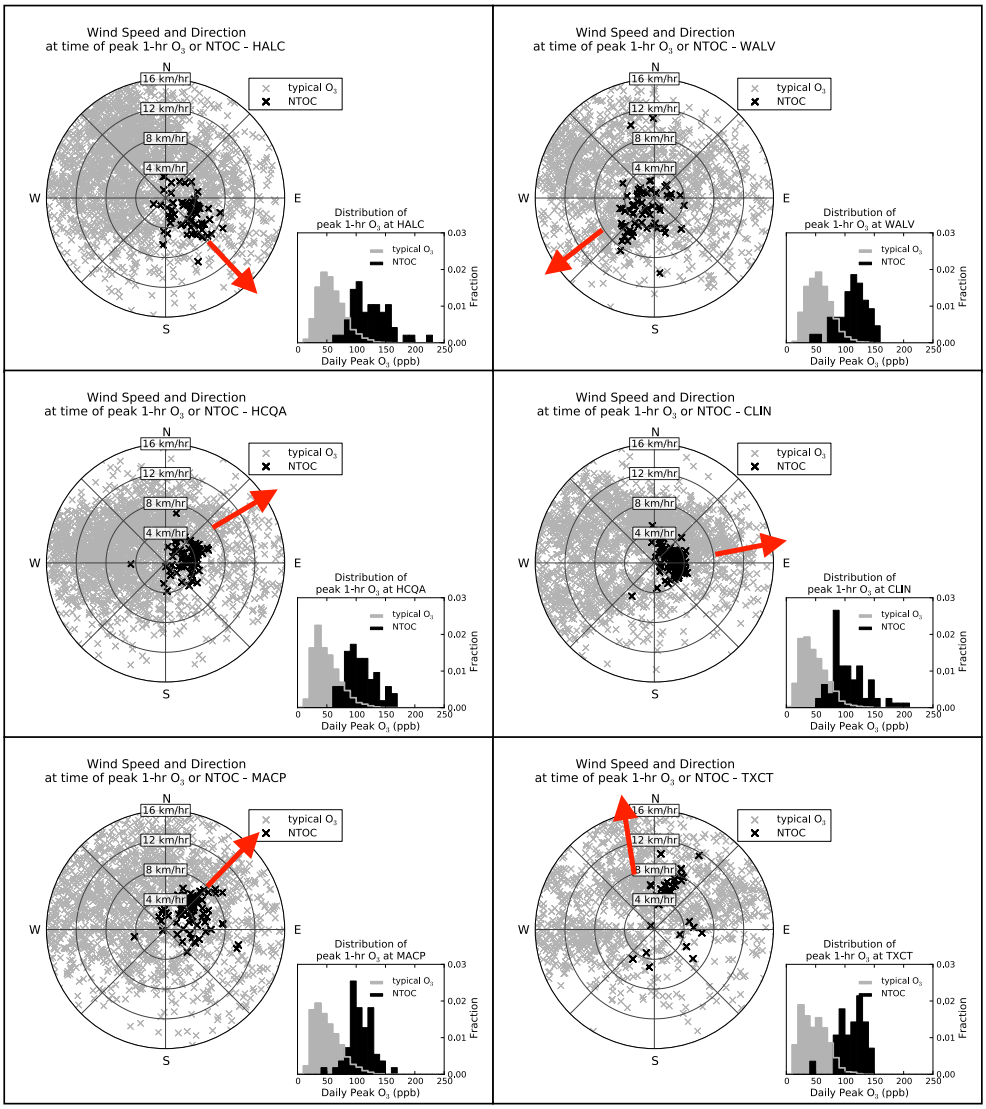

Figure 3.2: Wind speed, wind direction, and peak 1-hr O_3 levels on all typical and non-typical O_3 change (NTOC) days for six monitors (see Figure 3.1 for location). The grey markers in the radar plot give the wind speed and direction at the time the peak 1-hr O_3 level was measured on typical days. The black markers give the wind speed and direction at the time a NTOC was measured. The red arrow points toward the red star (ship channel marker) in Figure 3.1. The histogram shows the distribution of peak 1-hr O_3 levels on typical days (grey) and NTOC days (black). All available data during the O_3 season (April - October) from 2000 to 2011 is included in this figure.

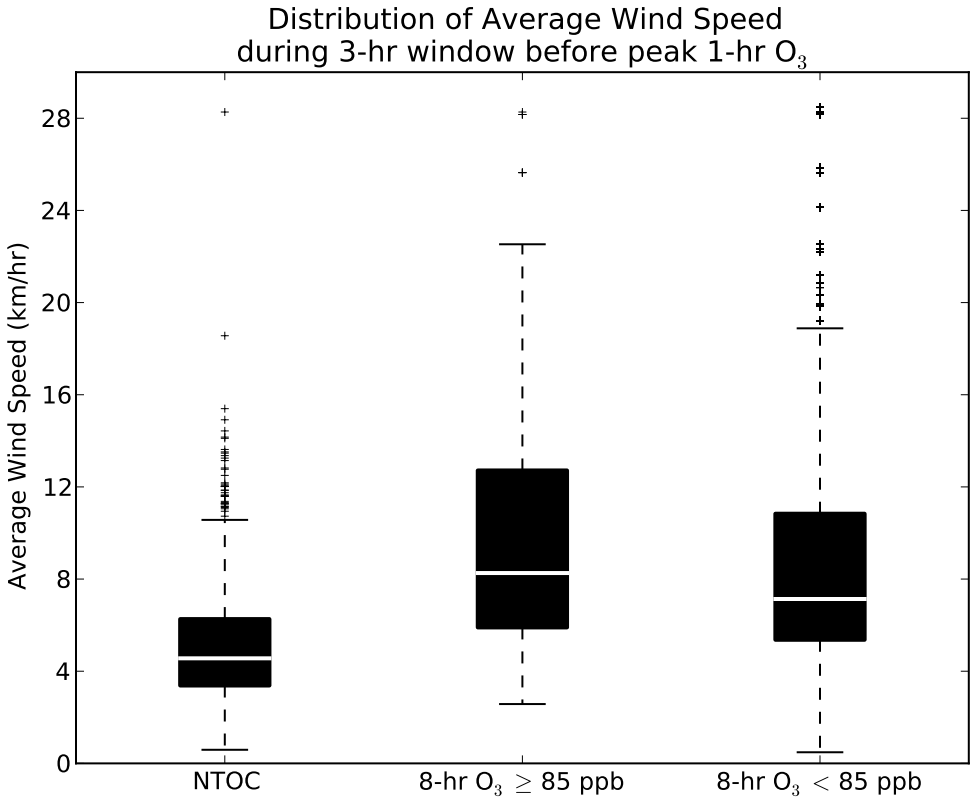

Figure 3.3: Box and whisker plots of 3-hr average wind speed measurements on non-typical O_3 change (NTOC) days (left), days that violate the 85-ppb federal standard (middle) and days below the federal standard (right). Box tops, middles and bottoms give the 75th, 50th and 25th percentile values. Whiskers extend to the most extreme data point within 1.5 times the inner quartile range. The 3-hr average wind speed was obtained by averaging the 1-hr wind speed measurement during the hour of peak O_3 level with the wind speed measurements from the 2 hr before the peak O_3 level. Available data from all monitors and years are included in this figure.

this average, we used the wind speed from the hour during which peak O_3 levels (or NTOCs) were observed and measurements from the previous 2 hr. A 3-hr average was used because it has the effect of smoothing out the hour-to-hour variability and longer averages are a poor indicator of local effects. It is clear that NTOCs occur on days with low wind speeds, lower even than typical high O_3 level days. The 25th, 50th, and 75th percentile 3-hr average wind speeds preceding NTOCs are 3.4, 4.6, and 6.3 km/hr. For typical days that violate the 1997 O_3 standard, those values are 5.9, 8.3, and 12.7 km/hr. Days that did not reach the 0.08-ppm standard generally had wind speeds that were slightly lower than violation days. The 25th, 50th, and 75th percentile values for non-violation days were 5.4, 7.1, and 10.8 km/hr.

Figure 3.4 shows, on a fractional basis, the time of day when all NTOCs and peak 1-hr O_3 levels are measured for all monitors. NTOCs generally occur in the late morning and into the early afternoon. NTOCs peak at 9 a.m. and 10 a.m. with 78% occurring before 1 p.m. Peak 1-hr O_3 levels occur later in the day; 2 p.m. is the most frequent time for peak 1-hr O_3 levels. More than half (56%) of all peak 1-hr O_3 levels occur at 12:00 p.m. or later.

3.3.2 Formaldehyde analysis

CH_2O is a known marker for photochemical oxidation reactions that lead to O_3 formation; it is also, itself, a precursor to O_3. Oxidation of HRVOCs produces substantial yields of CH_2O. For example, each ethene molecule that is attacked by the hydroxyl radical ($^{\cdot}OH$) produces 1.44 molecules of CH_2O (Seinfeld and Pandis, 2006). Two monitors had 1-hr CH_2O measurements on NTOC days - CLIN and DRPK. For each monitor, CH_2O measurements were separated into two groups according to whether they occurred before or after the measured NTOC. CH_2O concentrations were greater following a NTOC. The Mann-Whitney non-parametric statistical test

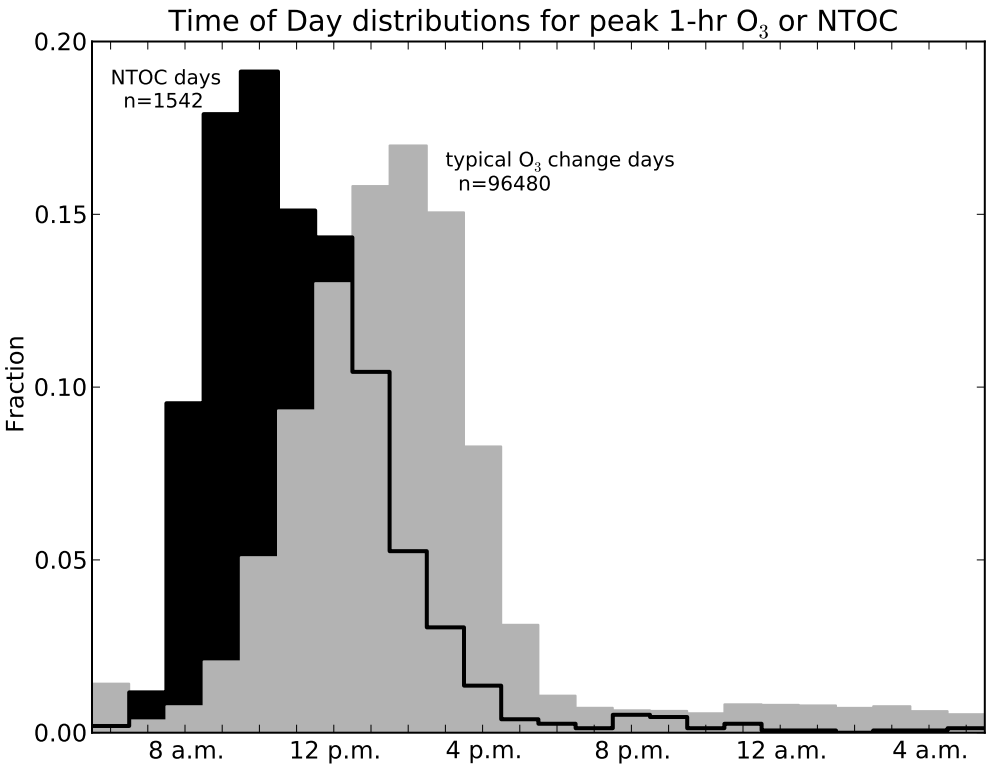

Figure 3.4: Distributions of the time of day during which non-typical O_3 changes (NTOCs) and peak 1-hr O_3 levels occur. Available data from all 25 monitors and twelve years are included in this figure.

was used to determine whether the differences between CH_2O values before and after a NTOC are statistically significant. For both monitors, these differences were statistically significant (CLIN: U=2, $P \ll 0.01$; DRPK: U=36, $P \ll 0.01$). This is not a surprising finding because most NTOCs occur in the late morning. It is expected that CH_2O concentrations will rise throughout the photochemical day because it is a product of VOC oxidation. Elevated CH_2O concentrations in the morning, though, could be indicative of primary emissions.

Next, we compared distributions of hourly CH_2O values on typical and NTOC days at each monitor again using the Mann Whitney non-parametric test. The test results are shown in Figure 3.5. Distributions of 1-hr CH_2O measurements for NTOC days are shown in black and the distributions for typical O_3 days are shown in grey. For each monitor, CH_2O measurements did not differ significantly in the morning. Results of the Mann-Whitney test show statistical significance in the afternoon, however. At CLIN (Figure 3.5a), CH_2O concentrations on NTOC days are significantly greater at 1 p.m. (U=3, P=0.032) and 2 p.m. (U=39, P=0.012). At DRPK (Figure 3.5b), CH_2O concentrations on NTOC days are significantly greater at 2 p.m. (U=80.5, P=0.003) and 3 p.m. (U=54, P=0.014).

We also looked at O_3 and CH_2O levels on specific NTOC days. Figure 3.6a shows measured time series data at the CLIN monitor on October 23, 2003. The black line shows 1-hr O_3 concentrations, and the black dots show 1-hr CH_2O values. The shaded regions extend up to the 90th (dark grey) and 95th percentile (light grey) CH_2O concentrations for all typical O_3 days. In Figure 3.6a, there is a 156-ppb increase in O_3 at 11 a.m. Before this NTOC, the morning CH_2O measurements were less than the 90th (6 a.m.) and 95th percentile (7 a.m.) CH_2O concentrations. After the NTOC, though, 1-hr CH_2O values are well outside these distributions reaching 27 ppb at 1 p.m. These results are consistent with Figure 3.5a.

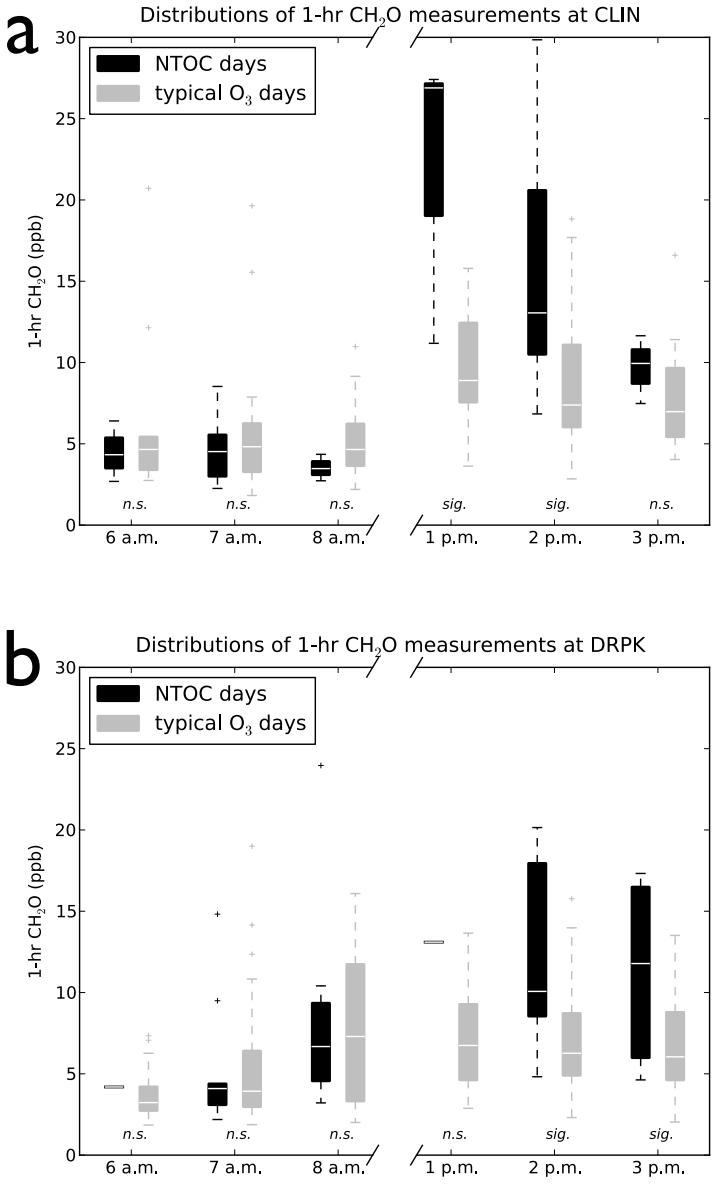

Figure 3.5: Box and whisker plots of 1-hr CH_2O measurements at CLIN (a) and DRPK (b) for non-typical O_3 change (NTOC) days (black) and typical O_3 level days (grey). Box tops, middles and bottoms give the 75th, 50th and 25th percentile values. Whiskers extend to the most extreme data point within 1.5 times the inner quartile range. The distributions are not significantly different (n.s.) in the morning before most NTOCs occur. Immediately following a NTOC, CH_2O concentrations often increase substantially. Using the MannWhitney non-parametric test it was determined that differences between the typical and NTOC distributions are statistically significant (sig.) for CLIN at 1:00 p.m. (U=3, P=0.032) and 2:00 p.m. (U=39, P=0.012) and for DRPK at 2:00 p.m. (U=80.5, P=0.003) and 3:00 p.m. (U=54, P=0.014).

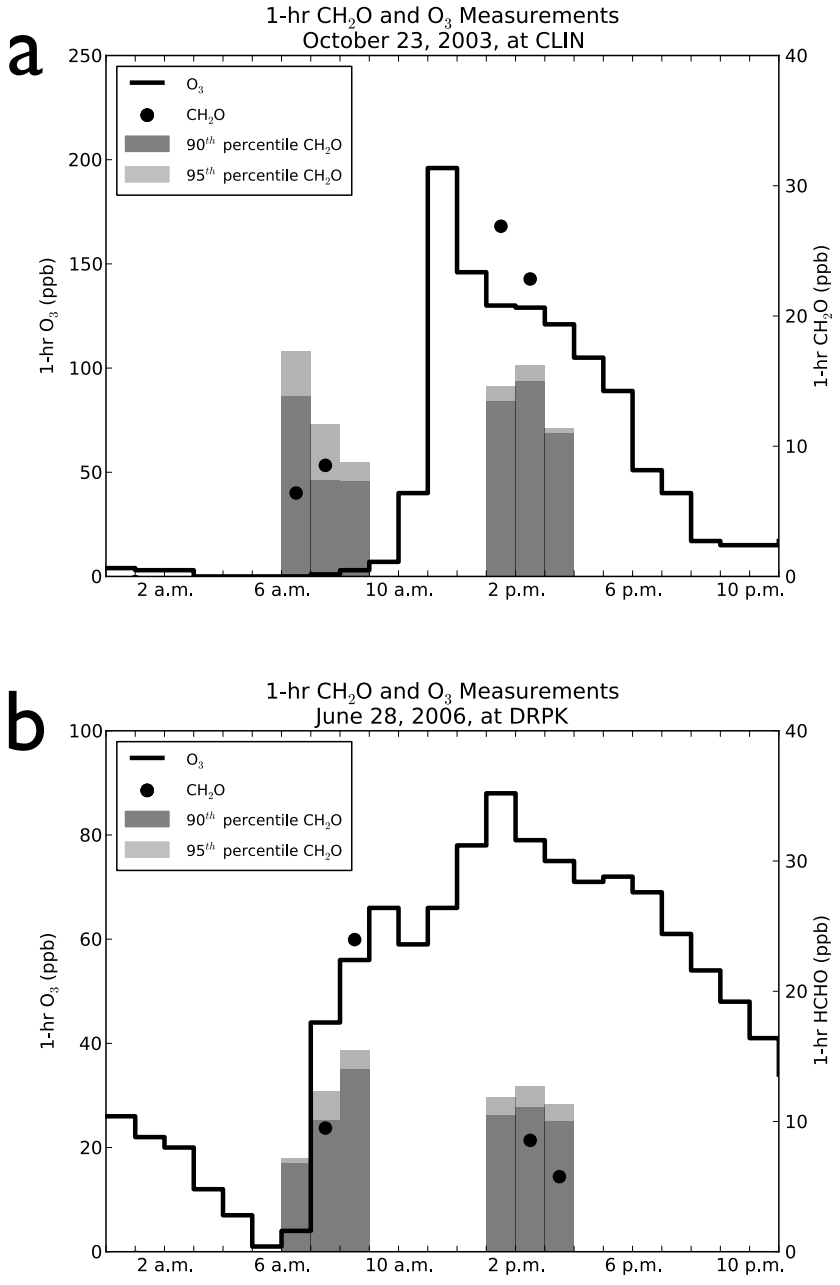

Figure 3.6: O_3 time series plot on October 23, 2003, at CLIN (a) and June 28, 2006, at DRPK (b). The black line shows 1-hr O_3 concentrations, and the black dots show 1-hr CH_2O measurements for the stated date. The shaded boxes extend up to the 90th (dark grey) and 95th percentile (light grey) CH_2O values on all typical O_3 level days for each hour when measurements were taken at both stations. (Note the different y-axis scales for 1-hr O_3.)

Figure 3.6b shows measured time series data at the DRPK monitor on June 18, 2006. This NTOC (40-ppb increase) occurred at 7 a.m., then 1 hr later, the CH_2O concentration was 24ppb, which is well above the 95th percentile for all DRPK CH_2O measurements at that hour. CH_2O values for all other times, however, are within shaded regions. Taken together, Figures 3.5 and 3.6 indicate that CH_2O concentrations rise substantially for a short period following a NTOC, and that this rise is significantly greater than the routine diurnal CH_2O cycle.

3.3.3 Sulfur dioxide analysis

Many SO_2 measurements exhibit behavior that looks similar to NTOCs. That is, concentrations of SO_2 increase dramatically from one hour to the next. These non-typical SO_2 increases often occur just before or during the exact hour a NTOC is measured. Figure 3.7 shows such an instance at the HROC monitor on July 9, 2005. The figure shows an O_3 (black line) increase of 52 ppb at 11 a.m. During the same hour, SO_2 (red line) values increase from 8.7 to 35.9 ppb. The shaded regions extend up to the 90th (dark grey) and 95th percentile (light grey) SO_2 concentrations on all typical O_3 days. At the time of the sudden increase in pollutant concentrations, the SO_2 value is well above the 95th percentile for all HROC SO_2 measurements at that hour. Also in Figure 3.7, we show the wind measurements that were taken at HROC on July 9, 2005. The wind barbs along the top of the figure show wind speed and direction for each hour. Half barbs indicate 5 km/hr and full barbs indicate 10 km/hr winds; the barbs are additive. Circles indicate stagnant conditions. Leading up to the NTOC, the winds were blowing from the southeast with low speeds. Just before the O_3 and SO_2 increase, the winds shift and blow due west. Interestingly, the industrial ship channel is east of the HROC monitor. Thus, the NTOC and sudden increase in SO_2 occurred when the monitor was downwind of Houston's industrial region.

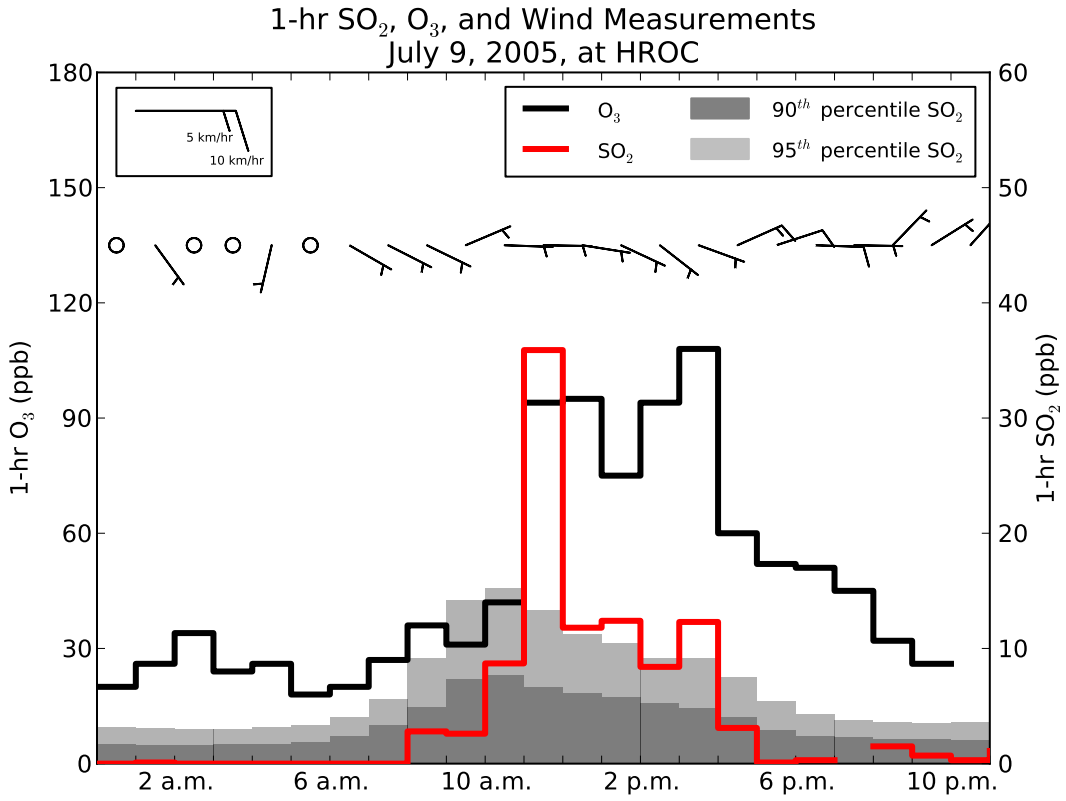

Figure 3.7: O_3 (black) and SO_2 (red) time series plot on July 9, 2005, at HROC. The wind barbs along the top of the figure show the hourly wind speed and direction for this date. The shaded boxes extend up to the 90th (dark grey) and 95th percentile (light grey) SO_2 values on all days for each hour when measurements were taken.

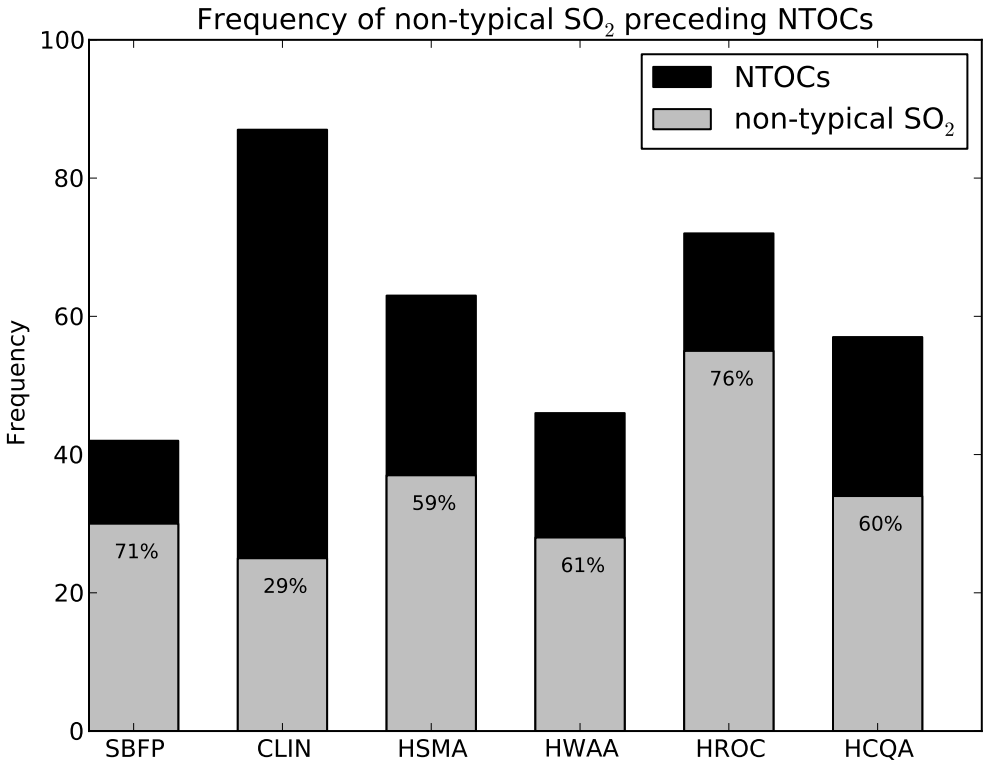

Figure 3.8: Frequency of non-typical SO_2 concentrations preceding non-typical O_3 changes (NTOCs) at six monitors. The black bars show the number of NTOCs measured at each monitor from 2000 to 2011; the grey bars show the number of NTOCs that had an SO_2 concentration above the 95th percentile up to 5 hr before the NTOC.

Figure 3.7 is not an isolated occurrence; SO_2 concentrations above the 95th percentile preceded 209 NTOCs out of a total of 367 NTOCs at the six monitors that measure both O_3 and SO_2. Figure 3.8 shows this analysis for these six monitors. The height of the black bars shows the number of NTOCs that were measured at each monitor. The height of the grey bars shows the number of those NTOCs that had an SO_2 concentration above the 95th percentile up to 5 hr before the NTOC. With the exception of CLIN a majority of NTOCs were preceded by large SO_2 values. At HROC for example, 55 out of 72 NTOCs were preceded by a significant increase in SO_2 concentrations.

3.4 Discussion

This study benefitted from a long, continuous measurement record from a large number of monitoring stations across Houston. During this period, 2000 - 2011, there have been significant changes to emissions in the region, and much progress has been made in lowering O_3 concentrations. Figure 3.9 shows design values (grey markers) for each monitor from 2002 - 2011. (A monitor's design value is the 3-year average of the annual fourth highest daily maximum 8-hr average O_3 level as defined by Title 40, Section 50.15, Appendix P of the Code of Federal Regulations, 73 FR 16511, 27 March 2008.) Beginning in 2007, design values began to decline, and, by 2009, all monitors were below the 0.08-ppm 8-hr O_3 federal standard (dashed line). Emissions reductions described in the TCEQ's 2004 SIP, especially the HRVOC restrictions, likely played a substantial part in the lower O_3 design values.

In Vizuete et al. (2011) we described a method for determining the influence of NTOCs on the attainment process by removing or ''filtering'' NTOC days from the design value calculation. The black markers in Figure 3.9 show the filtered design values for each monitor. Looking ahead to the 2008 0.075-ppm standard (solid line), removing NTOC days brings ten additional monitors into attainment. The individual monitors are not labeled in Figure 3.9, but the monitors with design values below 0.075 ppm in 2011 only after filtering are CLIN, CNR2, HCHV, HLAA, HTCA, HWAA, LYNF, SBFP, SHWH, and TXCT. Thus, NTOCs are still a policy-relevant phenomenon despite their reduced frequency and magnitude.

With that in mind, this study has characterized some major differences between typical O_3 days and NTOC days. We have described meteorological preconditions and geographic origins, and found evidence for heightened photochemical O_3 production on NTOC days.

Most NTOCs occur when monitors are directly downwind of the industrial ship

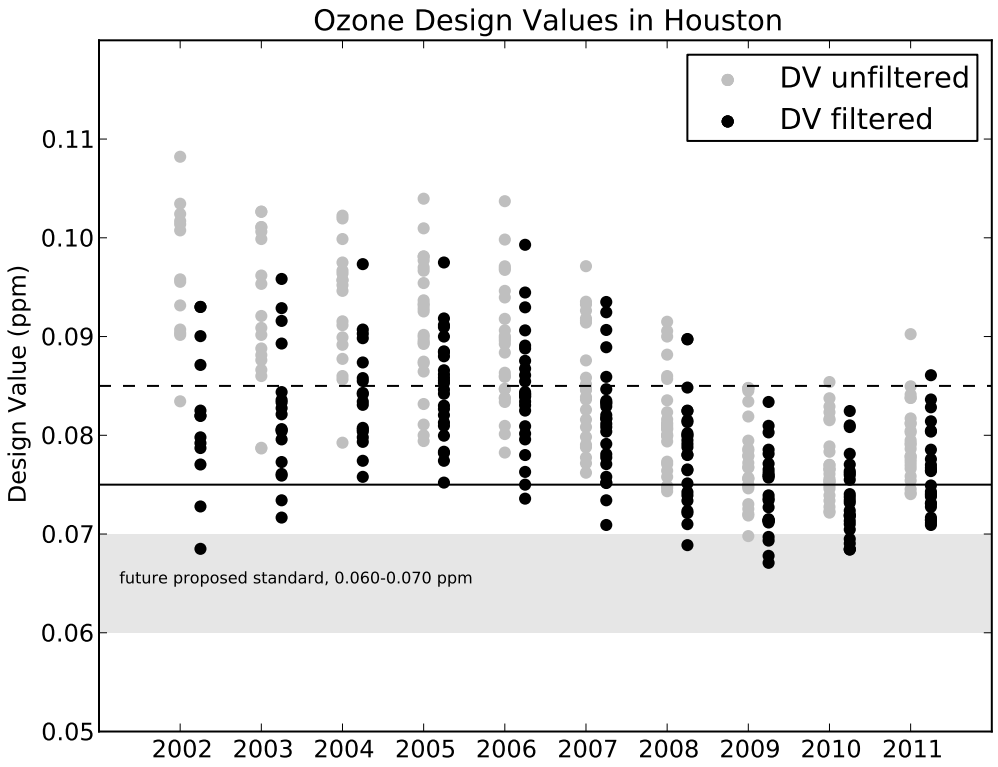

Figure 3.9: O_3 design values for the monitors used in this study from 2002 to 2011. Each grey marker shows the design value for a different monitor. The black markers show the design values for each monitor after all NTOCs have been removed ("filtered") from the calculation. The dotted black line marks the 1997 0.08-ppm 8-hr O_3 standard; the solid black line marks the 2008 0.075-ppm 8-hr O_3 standard; the grey shaded region marks the range of proposed future standards.

channel. Figure 3.2 shows that air masses originating in the ship channel produce NTOCs that are measured at the monitors. The NTOCs are usually measured in the late morning before the meteorological recirculation that is commonly seen on high O_3 level days. In fact, peak O_3 levels generally occur later in the day and are often measured when the winds are not blowing from the ship channel to the monitor. This indicates that some of the processes that lead to NTOC formation do not fit perfectly within the accepted paradigm of typical high O_3 formation. That paradigm holds that high O_3 levels typically occur in the afternoon following the recirculation of photochemically aged air masses. NTOC formation in the late morning is potentially due to the accumulation of O_3 precursors overnight, although 1-hr automated gas chromatograph data (not shown) did not reveal meaningful differences of HRVOC concentrations on NTOC days compared to typical O_3 days. Another plausible explanation for late morning NTOC formation is entrainment from the free troposphere as the planetary boundary layer rises. This finding merits further study and will be a focus of a future 3-D modeling simulation.

We have suggested the importance of industrial HRVOC emissions previously (Vizuete et al., 2011; Couzo et al., 2012), and the results presented here provide evidence for that position. Short-term releases of HRVOCs are known to occur in the ship channel (Wert et al., 2003; Murphy and Allen, 2005; Cowling et al., 2007; Webster et al., 2007; de Gouw et al., 2009; McCoy et al., 2010), and modeling has shown that these releases can lead to rapid O_3 increases (Vizuete et al., 2008; Henderson et al., 2010). Given the low wind speeds observed on NTOC days, there is sufficient time for these HRVOC releases to produce the observed O_3 increases. Even routine emissions could accumulate and oxidize in sufficient quantity as they are slowly advected to the monitors.

Figure 3.5 shows statistically significant increases of CH_2O concentration in the

hours immediately following NTOCs. This suggests that the increases in O_3 levels on some NTOC days are due at least in part to heightened chemical production above usual levels. Although there is some debate about the exact ratio of primary to secondary CH_2O production in Houston (Garcia et al., 2006; Olaguer et al., 2009; Guven and Olaguer, 2011; Parrish et al., 2012; Zhang et al., 2013), the nature of the CH_2O has little bearing on the conclusion that the NTOCs are the result of chemical production. If the CH_2O is primary, this is direct evidence for an emission event as CH_2O could be emitted, for example, from an overactive and inefficient industrial process flare. If the CH_2O is secondary, this is indirect evidence for the importance of HRVOC emissions because both elevated secondary CH_2O and O_3 levels have been found in industrial plumes.

We also found interesting SO_2 behavior on most NTOC days, as exhibited in Figure 3.7. High SO_2 concentrations have been used as a marker for certain types of industrial activity (Rappengluck et al., 2010), especially combustion processes and fluidized catalytic cracking units. In fact, a previous study found that a large industrial source in Texas City co-emitted large amounts of SO_2 and CH_2O (Stutz et al., 2011). That many NTOCs are preceded by high concentrations of SO_2 and followed by high CH_2O values points to industrial emissions as an important variable in NTOC formation.

This study provides further evidence that NTOC formation is different from typical high O_3 in Houston. In their 2004 SIP, the TCEQ proposed controlling routine and short-term HRVOC emissions from industrial facilities with the potential to release more than 10 tons ($\sim$ 9.07 Mg) of HRVOCs per year. The frequency and magnitude of NTOCs has decreased dramatically since the emission controls took effect, but NTOCs still occur at some monitors. In fact, ten monitors have 2011 design values below the federal 0.075-ppb 8-hr O_3 standard only after NTOCs are filtered from the calculation. The industrial ship channel is consistently upwind of these O_3 events, so it is possible

that smaller emission sources not affected by the HRVOC limits are contributing to the phenomenon, especially given the large number of petrochemical facilities in the region. Another round of targeted emission controls may further reduce the frequency of NTOCs and continue the downward trend in Houston's O_3 design values.

REFERENCES

R. M. Banta, C. J. Senff, J. Nielsen-Gammon, L. S. Darby, T. Ryerson, J. Alvarez, S. Sandberg, E. Williams, and M. Trainer (2005). A bad air day in Houston. *Bull. Am. Meteorol. Soc.*, 86(5):657--669. doi:10.1175/BAMS-86-5-657.

C. M. Berkowtiz and C. W. S. P. V. Doskey (2005). Hydrocarbon observations and ozone production rates in Western Houston during the Texas 2000 Air Quality Study. *Atmos. Environ.*, 39:3383. doi:10.1016/J.ATMOSENV.2004.12.007.

E. Couzo, A. Olatosi, H. E. Jeffries, and W. Vizuete (2012). Assessment of a regulatory model's performance relative to large spatial heterogeneity in observed ozone in Houston, Texas. *J. Air Waste Manag. Assoc.*, 62:696--706. doi:10.1080/10962247.2012.667050.

E. Cowling, C. Furiness, B. Dimitriades, and D. Parrish (2007). Final rapid science synthesis report: Findings from the second Texas Air Quality study (TexAQS II) - Final report to the Texas Commission on Environmental Quality. TCEQ Contract Number 582-4-65614. http://aqrp.ceer.utexas.edu/docs/RSSTFinalReportAug31.pdf (Verified April 29, 2013).

P. H. Daum, L. I. Kleinman, S. R. Springston, L. J. Nunnermacker, Y. N. Lee, J. Weinstein-Lloyd, J. Zheng, and C. M. Berkowitz (2003). A comparative study of O_3 formation in the Houston urban and industrial plumes during the 2000 Texas Air Quality Study. *J. Geophys. Res.*, 108(D23):4715. doi:10.1029/2003JD003552.

P. H. Daum, L. I. Kleinman, S. R. Springston, L. J. Nunnermacker, Y. N. Lee, J. Weinstein-Lloyd, J. Zheng, and C. M. Berkowitz (2004). Origin and properties of plumes of high ozone observed during the Texas 2000 Air Quality Study (TexAQS 2000). *J. Geophys. Res.*, 109(D17306). doi:10.1029/2003JD004311.

J. A. de Gouw, S. T. Hekkert, J. Mellqvist, C. Warneke, E. L. Atlas, F. C. Fehnsenfeld, A. Fried, G. J. Frost, F. J. Harren, J. S. Holloway, B. Lefer, R. Lueb, J. F. Meagher, D. D. Parrish, M. Patel, L. Pope, D. Richter, C. Rivera, T. B. Ryerson, J. Samuelsson, J. Walega, R. A. Washenfelder, P. Wibring, and X. Zhu (2009). Airborne measurements of ethene from industrial sources using laser photo-acoustic spectroscopy. *Environ. Sci. Technol.*, 43:2437. doi:10.1021/ES802701A.

F. Gan and P. K. Hopke (2003). Data mining of the relationship between volatile organic compounds and transient high ozone formation. *Anal. Chim. Acta*, 490:153--158. doi:10.1016/S0003-2670(03)00497-5.

A. R. Garcia, R. Volkamer, L. T. Molina, M. J. Molina, J. Samuelson, J. Mellqvist, B. Galle, S. C. Herndon, and C. E. Kolb (2006). Separation of emitted and photochemical formaldehyde in Mexico City using a statistical analysis and a new pair of gas-phase tracers. *Atmos. Chem.*, 6:4545. doi:10.5194/ACP-6-4545-2006.

B. B. Guven and E. P. Olaguer (2011). Ambient formaldehyde source attribution in Houston during TexAQS II and TRAMP. *Atmos. Environ.*, 45:4272. doi:10.1016/J.ATMOSENV.2011.04.079.

B. H. Henderson, H. E. Jeffries, B. U. Kim, and W. Vizuete (2010). The influence of model resolution on ozone in industrial volatile organic compound plumes. *J. Air Waste Manag. Assoc.*, 60:1105--1117. doi:10.3155/1047-3289.60.9.1105.

L. I. Kleinman, P. H. Daum, D. Imre, Y. N. Lee, L. J. Nunnermacker, S. R. Springston, J. Weinstein-Lloyd, and J. Rudolph (2002). Ozone production rate and hydrocarbon reactivity in 5 urban areas: A cause of high ozone concentration in Houston. *Geophys. Res. Lett.*, 29:1467. doi:10.1029/2001GL014569.

B. J. McCoy, P. S. Fischbeck, and D. Gerard (2010). How big is big? How often is often? Characterizing Texas petroleum refining upset air emissions. *Atmos. Environ.*, 44:4230--4239. doi:10.1016/j.atmosenv.2010.07.088.

C. F. Murphy and D. T. Allen (2005). Hydrocarbon emissions from industrial release events in the Houston-Galveston area and their impact on ozone formation. *Atmos. Environ.*, 39:3785--3798. doi:10.1016/j.atmosenv.2005.02.051.

F. Ngan and D. Byun (2011). Classification of weather patterns and associated trajectories of high-ozone episodes in the Houston-Galveston-Brazoria area during the 2005/06 TexAQS-II. *J. Appl. Meteorol. Climatol.*, 50:485--499. doi:10.1175/2010jamc2483.1.

E. P. Olaguer, B. Rappengluck, B. Lefer, J. Stutz, J. Dibb, R. Griffin, W. H. Brune, M. Shauck, M. Buhr, H. E. Jeffries, W. Vizuete, and J. P. Pinto (2009). Deciphering the role of radical precursors during the Second Texas Air Quality Study. *J. Air Waste Manag. Assoc.*, 59:1258. doi:10.3155/1047-3289.59.11.1258.

D. D. Parrish, T. B. Ryerson, J. Mellqvist, J. Johansson, A. Fried, D. Richter, J. G. Walega, R. A. Washenfelder, J. A. de Gouw, J. Peischl, K. C. Aikin, S. A. McKeen, G. J. Frost, F. C. Fehsenfeld, and S. C. Herndon (2012). Primary and secondary sources of formaldehyde in urban atmospheres: Houston, Texas, region. *Atmos. Chem. Phys.*, 12:3273. doi:10.5194/ACP-12-3273-2012.

B. Rappengluck, P. K. Dasgupta, M. Leuchner, Q. Li, and W. Luke (2010). Formaldehyde and its relation to CO, PAN, and SO_2 in the Houston-Galveston airshed. *Atmos. Chem. Phys.*, 10:2413. doi:10.5194/ACP-10-2413-2010.

T. B. Ryerson, M. Trainer, W. M. Angevine, C. A. Brock, R. W. Dissly, F. C. Fehnsenfeld, G. J. Frost, P. D. Goldan, J. S. Holloway, G. Hubler, R. O. Jakoubek, W. C. Kuster, J. A. Neuman, D. K. Nicks, Jr., D. D. Parrish, J. M. Roberts, D. T. Sueper, E. L. Atlas, S. G. Donnelly, F. Flocke, A. Fried, W. T. Potter, S. Schauffler, V. Stroud, A. J. Weinheimer, B. P. Wert, C. Wiedinmyer, R. J. Alvarez, R. M. Banta, L. S. Darby, and C. J. Senff (2003). Effect of petrochemical

industrial emissions of reactive alkenes and NOx on tropospheric ozone formation in Houston, Texas. *J. Geophys. Res. Atmos.*, 108:4249. doi:10.1029/2002JD003070.

J. H. Seinfeld and S. N. Pandis (2006). *Atmospheric Chemistry and Physics*. Wiley, Hoboken, NJ, 2nd edition. Ch. 6, p. 248.

J. Stutz, O. Pikelnaya, G. M. E. Spinei, S. Herndon, E. Wood, O. Oluwole, W. Vizuete, and E. Couzo (2011). Quantification of hydrocarbon, NOx, and SO_2 emissions from petrochemical facilities in Houston: Interpretation of 2009 FLAIR dataset. Air Quality Research Program, The University of Texas: Austin, TX. Available at http://aqrp.ceer.utexas.edu/viewprojects.cfm?Prop_Num=10-045.

Texas Commission on Environmental Quality (2004). Revisions to the State Implementation Plan (SIP) for the control of ozone air pollution: Houston/Galveston/Brazoria ozone nonattainment area. Austin, TX. Project No. 2004-042-SIP-NR.

W. Vizuete, H. E. Jeffries, T. W. Tesche, E. P. Olaguer, and E. Couzo (2011). Issues with ozone attainment methodology for Houston, TX. *J. Air Waste Manag. Assoc.*, 61:238--253. doi:10.3155/1047-3289.61.3.238.

W. Vizuete, H. E. Jeffries, A. Valencia, E. Couzo, E. Christoph, J. Wilkinson, B. Henderson, H. Parikh, and J. Kolling (2009). HARC Project H97: Multi-model, multi-episode process analysis to investigate ozone formation and control sensitivity in the 2000/2005/2006 Houston SIP episode models. The Woodlands, TX: Houston Advanced Research Center. http://projects.tercairquality.org/AQR/H097.

W. Vizuete, B. U. Kim, H. E. Jeffries, Y. Kimura, D. T. Allen, M. A. Kioumourtzoglou, L. Biton, and B. Henderson (2008). Modeling ozone formation from industrial emission events in Houston, Texas. *Atmos. Environ.*, 42:7641--7650. doi:10.1016/j.atmosenv.2008.05.063.

R. A. Washenfelder, M. Trainer, G. J. Frost, T. B. Ryerson, E. L. Atlas, J. A. de Gouw, F. M. Flocke, A. Fried, J. S. Holloway, D. D. Parrish, J. Peischl, D. Richter, S. M. Schauffler, J. G. Walega, C. Warneke, P. Weibring, and W. Zheng (2010). Characterization of NOx, SO_2, ethene, and propene from industrial emission sources in Houston, Texas. *J. Geophys. Res. - Atmos.*, 115(D16311). doi:10.1020/2009JD013645.

M. Webster, J. Nam, Y. Kimura, H. E. Jeffries, W. Vizuete, and D. T. Allen (2007). The effect of variability in industrial emissions on ozone formation in Houston. *Atmos. Environ.*, 41:9580--9593. doi:10.1016/j.atmosenv.2007.08.052.

B. P. Wert, M. Trainer, A. Fried, T. B. Ryerson, B. Henry, W. Potter, W. M. Angevine, E. Atlas, S. G. Donnelly, F. C. Fehnsenfeld, G. J. Frost, P. D. Goldan, A. Hansel, J. S. Holloway, G. Hubler, W. C. Kuster, D. K. Nicks, Jr., J. A. Neuman., D. D. Parrish, S. Schauffler, J. Stutz, D. T. Sueper, C. Wiedinmyer,

and A. Wisthaler (2003). Signatures of terminal alkene oxidation in airborne formaldehyde measurements during TexAQS 2000. *J. Geophys. Res. Atmos.*, 108(D3):4104. doi:10.1029/2002JD002502.

E. C. Wood, S. C. Herndon, E. C. Fortner, T. B. Onasch, J. Wormhoudt, C. E. Kolb, W. B. Knighton, B. H. Lee, M. Zavala, L. Molina, and M. Jones (2012). Combustion and destruction/removal efficiencies of in-use chemical flares in the greater Houston area. *Ind. Eng. Chem. Res.*, 51:12685. doi:10.1021/IE202717M.

H. Zhang, J. Li, Q. Ying, B. B. Guven, and E. P. Olaguer (2013). Source apportionment of formaldehyde during TexAQS 2006 using a source-oriented chemical transport model. *J. Geophys. Res. - Atmos.*, 118:1525.

CHAPTER 4
IMPLEMENTATION AND EVALUATION OF NEW NITROUS ACID FORMATION MECHANISMS IN A THREE-DIMENSIONAL CHEMICAL TRANSPORT MODEL

4.1 Introduction

Gas phase radical molecules are critical to the photochemical production of air pollution. The hydroxyl radical ($^{\cdot}\mathsf{OH}$) initiates volatile organic compound (VOC) oxidation reactions that lead to the hydroperoxy radical ($\mathsf{HO_2^{\cdot}}$) (Seinfeld and Pandis, 2006). $\mathsf{HO_2^{\cdot}}$ is key to converting nitric oxide (NO) to nitrogen dioxide ($\mathsf{NO_2}$), which can photolyze to produce ozone ($\mathsf{O_3}$). Nitrous acid (HONO) is known to affect radical budgets in urban environments by serving as an $^{\cdot}\mathsf{OH}$ source via the photolysis reaction

$$\mathsf{HONO} + h\nu \xrightarrow{\lambda<400nm} \mathsf{NO} + {}^{\cdot}\mathsf{OH} \tag{4.1}$$

Reaction 4.1 provides an early morning $^{\cdot}\mathsf{OH}$ source before more dominant sources such as formaldehyde ($\mathsf{CH_2O}$) and $\mathsf{O_3}$ are present in high concentrations (Harris et al., 1982; Harrison et al., 1996; Platt et al., 2002; Alicke et al., 2003). Despite its importance to gas-phase oxidant chemistry, HONO formation is not understood completely.

Two chemical mechanisms commonly used in photochemical modeling - Carbon Bond and Statewide Air Pollution Research Center (SAPRC) - include only homogenous chemical HONO formation (Yarwood et al., 2005; Carter, 2010). The gas-phase reactions - Reactions 4.2 and 4.3 - are the most important homogeneous HONO formation pathways.

$$NO + {}^{\cdot}OH \rightarrow HONO \tag{4.2}$$

$$NO + NO_2 + H_2O \rightarrow 2HONO \tag{4.3}$$

Recent modeling studies used the Community Multiscale Air Quality (CMAQ) model with the Carbon Bond 5 and SAPRC-99 chemical mechanisms, both of which include Reactions 4.2 and 4.3 (Sarwar et al., 2008; Czader et al., 2012; Concalves et al., 2012; Zhang et al., 2012). The models consistently showed HONO under predictions compared to measurements. Czader et al. (2012), for example, reported biases of up to 2 ppb. Additional 3-D and 1-D modeling systems using only homogeneous HONO formation also under predict HONO substantially, oftentimes by a factor of ten (Li et al., 2010, 2011; Wong et al., 2011). It is clear from these efforts that homogeneous formation of HONO is not sufficient to match observed concentrations. The authors in the above modeling studies concluded that key sources of HONO exist in addition to Reactions 4.2 and 4.3.

Two field campaigns in Houston, Texas, have provided HONO observations that support the possibility of a source of HONO. Measurements taken during the 2006 Texas Air Quality Study and the 2009 Study of Houston Atmospheric Radical Precursors (SHARP) showed strong vertical HONO concentration gradients during the day with higher values near the ground - something modeled homogeneous chemistry did not predict (Czader et al., 2012; Wong et al., 2012). Wong et al. (2012) hypothesized that the missing HONO formation pathways are photolytic and occur on or near the ground.

Observations in laboratory and field experiments over the past decade have uncovered two important heterogeneous HONO formation mechanisms that occur on surfaces (e.g. ground, aerosols) and involve photolysis. The first is the photolysis of surface adsorbed nitric acid (HNO_3) (Zhou et al., 2002; Beine et al., 2002; Dibb et al.,

2002; Zhou et al., 2003; Ramazan et al., 2004; He et al., 2006; Zhou et al., 2007, 2011). Together, Reactions 4.4 and 4.5 produce surface adsorbed HONO which can volatilize into the gas-phase.

$$\mathsf{HNO_{3}}_{ads} + h\nu \rightarrow \ \mathsf{NO_{2}}_{ads} + \mathsf{{}^{\cdot}OH} \tag{4.4}$$

$$2\mathsf{NO_{2}}_{ads} + \mathsf{H_{2}O}_{ads} \rightarrow \ \mathsf{HONO}_{ads} + \mathsf{HNO_{3}}_{ads} \tag{4.5}$$

The second HONO formation pathway is the photo-enhanced conversion of gas-phase $\mathsf{NO_2}$ on organic films or surfaces commonly found on the ground or aerosols (George et al., 2005; Stemmler et al., 2006, 2007). Reactions 4.6-4.8 show the HONO formation described by Stemmler et al. (2006).

$$HA + h\nu \rightarrow \ A_{red} + X \tag{4.6}$$

$$A_{red} + X \rightarrow \ A' \tag{4.7}$$

$$A_{red} + \mathsf{NO_2} \ \rightarrow \ A'' + \mathsf{HONO} \tag{4.8}$$

In the above reactions, HA is humic acid, A_{red} and X are the reduced and oxidized products of the photolyzed HA, and A' and A'' are derivatives of A_{red}. In urban environments with abundant nitrogen oxide $\mathsf{NO_x}$ concentrations, the rate-limiting step is Reaction 4.7 because both $\mathsf{NO_2}$ and the oxidized HA product, X, compete for the reduced HA product, A_{red}.

In addition to photo-enhanced heterogeneous chemical formation, HONO is directly emitted during combustion. The emitted HONO to emitted $\mathsf{NO_x}$ ratio has been estimated to be about 0.8% for a variety of vehicle types (Pitts et al., 1984; Kurtenbach et al., 2001).

Modeling efforts in recent years have attempted to include these new heterogeneous

reactions and emission-based HONO sources. A number of studies have accomplished this using 3-D Eulerian grid models such as CMAQ (Sarwar et al., 2008; Czader et al., 2012; Concalves et al., 2012; Zhang et al., 2012), which is often used by state environmental agencies to demonstrate future attainment of the federal O_3 standard. Li et al. (2010) and Li et al. (2011) used the Weather Research and Forecasting model coupled with Chemistry (WRF-CHEM). In all cases, adding the photolytic, heterogeneous, and directly emitted HONO formation pathways increased simulated HONO concentrations and improved agreement with HONO measurements. Sarwar et al. (2008) showed a normalized mean bias decrease from -98% to -42% when direct emissions and photo-enhanced heterogeneous HONO formation were included; Zhang et al. (2012) reported normalized mean bias improvement from -95% to -54%; for Li et al. (2011), mean normalized bias decreased from -97% to -39%; and Czader et al. (2012) found that the additional HONO sources increased morning HONO concentrations nearly ten-fold and improved correlation between simulated and measured values. These studies confirm that direct emissions and photo-enhanced heterogeneous formation are important contributors to atmospheric HONO concentrations. None of the modeling studies, however, considered separately direct emissions of HONO and heterogeneous chemistry, thus making it difficult to assess the individual impacts of emissions and heterogeneous formation.

Czader et al. (2012) employed the process analysis (PA) utility that is useful in determining which physical processes and chemical reactions are dominant. PA can explain *how* the new HONO formation pathways have affected the simulated environment, not simply *that* it has been affected. The findings of Czader et al. (2012) provide insight into the origin and fate of $^{\cdot}OH$ and how O_3 concentrations are impacted by additional HONO formation. From 6 a.m. to 9 a.m., the fractional contribution of HONO to $^{\cdot}OH$ production increased to 81% from 45% when direct emissions and

photo-enhanced heterogeneous chemistry are included. Concentrations of $^{\cdot}OH$ in the morning were, on average, 35% greater when the additional HONO sources are included. Increases in O_3 concentrations of up to 11 ppb were also reported.

Much of the analysis in Czader et al. (2012), however, is limited to the model's surface layer from which they found large vertical HONO fluxes. Convection transports vertically much of the HONO formed near the ground, thus removing it from the analysis volume. Tracking changes to the oxidative chemical environment of the entire mixed planetary boundary layer (PBL) can elucidate more completely how new sources of HONO affect air quality. For example, chemical HONO loss pathways can be obtained. Restricting analysis to a sub-layer within the PBL can lead to the conclusion that such losses are due to physical processes like vertical transport. While that may be true for a particular model layer, it is not true for the entire volume of air within the PBL.

While each modeling study implemented the new HONO sources differently, the various approaches taken to represent HONO formation can be generalized as one that parameterizes heterogeneous rate coefficients as a function of surface area to volume. The surfaces could include aerosols, buildings, and/or the ground. This type of parameterization is a useful approximation, but it is not an accurate representation of the physical and chemical processes. In this study, a more accurate approach to photo-enhanced heterogeneous HONO formation on surfaces is taken. A surface model has been developed that uses fluxes of HNO_3 and NO_2 to accumulate a surface inventory via dry deposition. The surface model allows the ground to act as a reservoir for deposited species and simulates chemical deposition to the surface, adsorption and penetration into soils and vegetation, photochemical degradation and transformation, and volatilization back into the air (re-emission). For the first time, dry deposition is not simply a removal process, but rather a dynamic process that makes deposited

species available for further chemical processing.

The surface model is added to version (v6.1) of the Comprehensive Air quality Model with extensions (CAMx), which, like CMAQ, is a 3-D air quality model routinely used for regulatory purposes. This study implements missing HONO formation pathways into a previously unreleased version of CAMx. This is the first time the new HONO sources have been added to CAMx, and it is the first time the surface model approach has been implemented to manage photo-enhanced heterogeneous HONO formation. With the surface model and PA implemented, HONO re-emission is quantified, and the chemical effects of the additional HONO are analyzed throughout the PBL. Model performance is evaluated using the extensive set of measurements that were taken during the 2009 SHARP campaign in Houston. The SHARP dataset provides the latest and most complete continuous measurements of radicals and radical precursors, and this is the first time they have been used to parameterize and evaluate HONO formation mechanisms in a 3-D air quality model.

The main goals of this study are to (1) assess separately the importance of direct HONO emissions and photo-enhanced heterogeneous HONO formation, and (2) quantify the impacts of the new HONO sources on $^{\cdot}OH$ cycles and O_3 production in Houston. This study builds on our previous work (Couzo et al., 2012, 2013) by addressing a known problem with regulatory modeling in Houston, namely, low reactivity. The critical examination of radical budgets, and enriched understanding of the reasons for predicted differences, will result in the identification of the most influential chemical processes. This will guide recommendations for their improved representation in regulatory air quality models.

4.2 Methods

4.2.1 CAMx setup

For the Houston 8-hr Ozone Coalition, Alpine Geophysics LLC (AG) and Climate & Atmospheric Research Associates developed multi-model ensembles for 2008-2010 focusing primarily on the Houston O_3 non-attainment area. Four ensemble members were constructed with alternative science configurations of the 5^{th} generation National Center for Atmospheric Research/Pennsylvania State University Mesoscale Model (MM5, v3.7), Weather Research and Forecasting model (WRF, v3.2.1), Global Biosphere Emissions and Interactions System (Glo-BEIS, v3.1), Model of Emissions of Gases and Aerosols from Nature (MEGAN, v2.04), and CAMx (v5.4.1) platforms. Thorough description of the model algorithms, data base development procedures, simulation strategy, and performance evaluation methods are given in the modeling protocol (Tesche et al., 2010). Results of the multi-species, multi-scale evaluations are publicly available.

Input databases for the best performing 2009 ensemble member were used in this study. This ensemble used Advanced Research WRF dynamics, the Carbon Bond 6 chemical kinetic mechanism, GlobEIS for biogenic emissions over Texas, MEGAN for biogenics elsewhere in the domain, Motor Vehicle Emission Simulator (MOVES) for mobile sources, the Texas Commission on Environmental Quality's (TCEQ) point source inventory, and the U.S. Environmental Protection Agency's (EPA) National Emission Inventory (NEI 2008). Lateral boundary conditions were developed from a 2009 Model for Ozone and Related Chemical Tracers 4 (MOZART-4) global simulation performed at the National Center for Atmospheric Research.

Modeling in this study was performed with CAMx version 6.1. Previously unreleased, this version of CAMx includes a surface model that allows for heterogeneous HONO formation. Many of the inputs (meteorology, landuse, albedo/haze/ozone,

and photolysis rates) were converted for use in CAMx version 6. ENVIRON developed the necessary conversion tools, and they are publicly available on the CAMx website (www.camx.com). See the CAMx v6.0 documentation for details (ENVIRON International Corporation, 2013).

The modeling episode spans the 2009 SHARP campaign (April 15-May 31) and has an output time resolution of one hour. Figure 4.1a shows the nested 36/12/4 km domain. Figure 4.1b shows a portion of the 4-km domain centered on Houston. SHARP measurements were taken at the Moody Tower site, which is shaded black in Figure 4.1b.

4.2.2 Surface model

The surface model processes are displayed in Figure 4.2, and Table 4.1 defines parameters that are referred to in Figure 4.2. While core model algorithms are used to deposit compounds to the surface and re-emit them to the atmosphere, the surface model tracks the accumulation of mass on terrestrial surface media (soil and vegetation) for subsequent physical removal (leaching into soil and penetration into plant tissue), chemical transformation (both heterogeneous and photolysis), and re-emission to the atmosphere. Deposition to water surfaces is assumed to be irreversible and is not tracked by the surface model.

After deposition to each surface grid cell at each time step, the newly deposited mass increment is divided among soil and vegetation according to landuse-dependent split factors and added to total surface mass accumulated during the model run. The fractional coverage of 11 landuse categories in each grid cell is an existing input to CAMx. For each grid cell, the net soil/vegetation split is determined by the combination of landuse-dependent split factors and the fractional coverage of each landuse type. The soil/vegetation splits for each of the 11 landuse categories

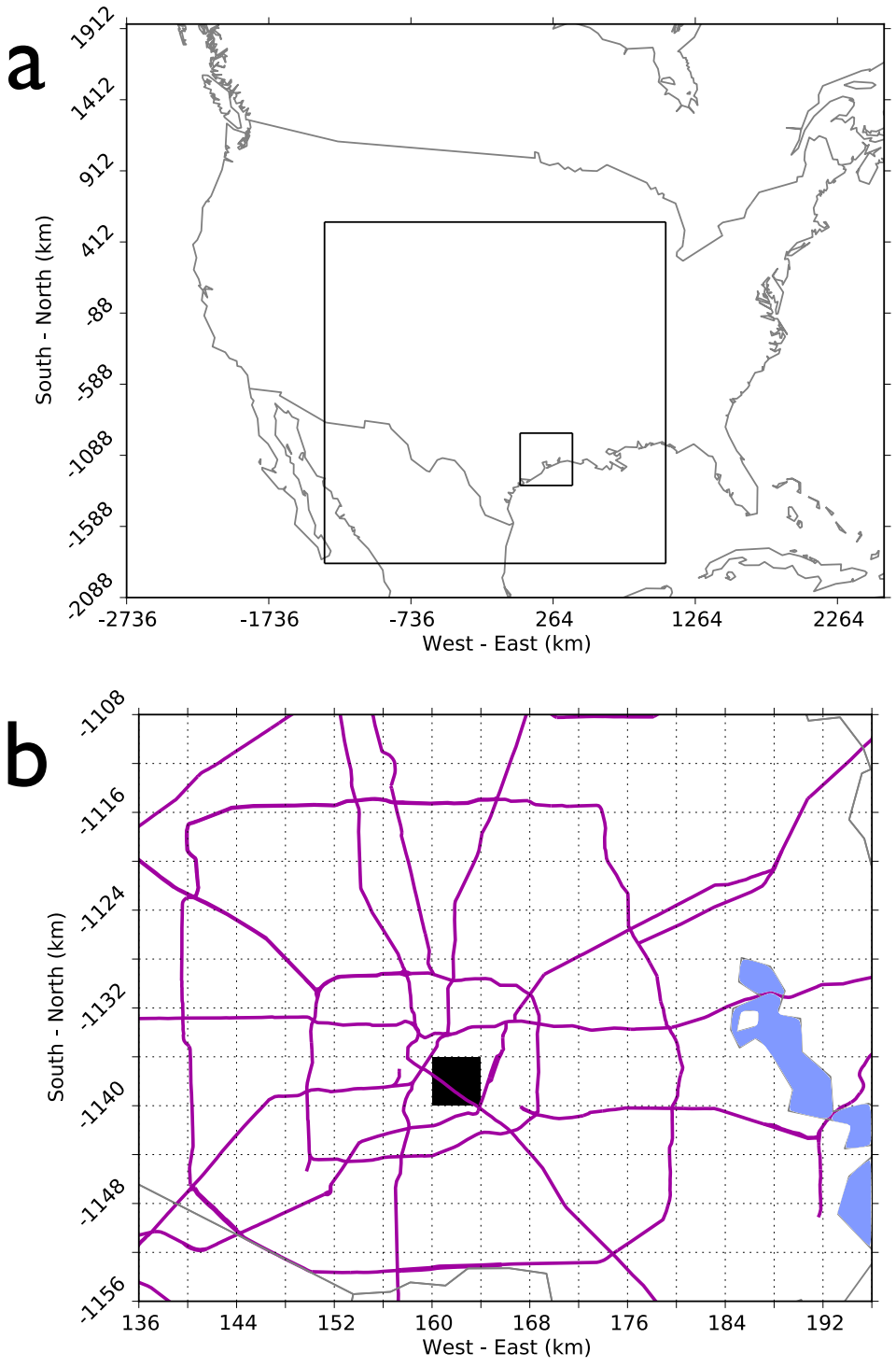

Figure 4.1: Nested 36/12/4 km CAMx modeling domain (a). A subset of the 4 km domain over downtown Houston (b). The black grid cell shows the location of Moody Tower.

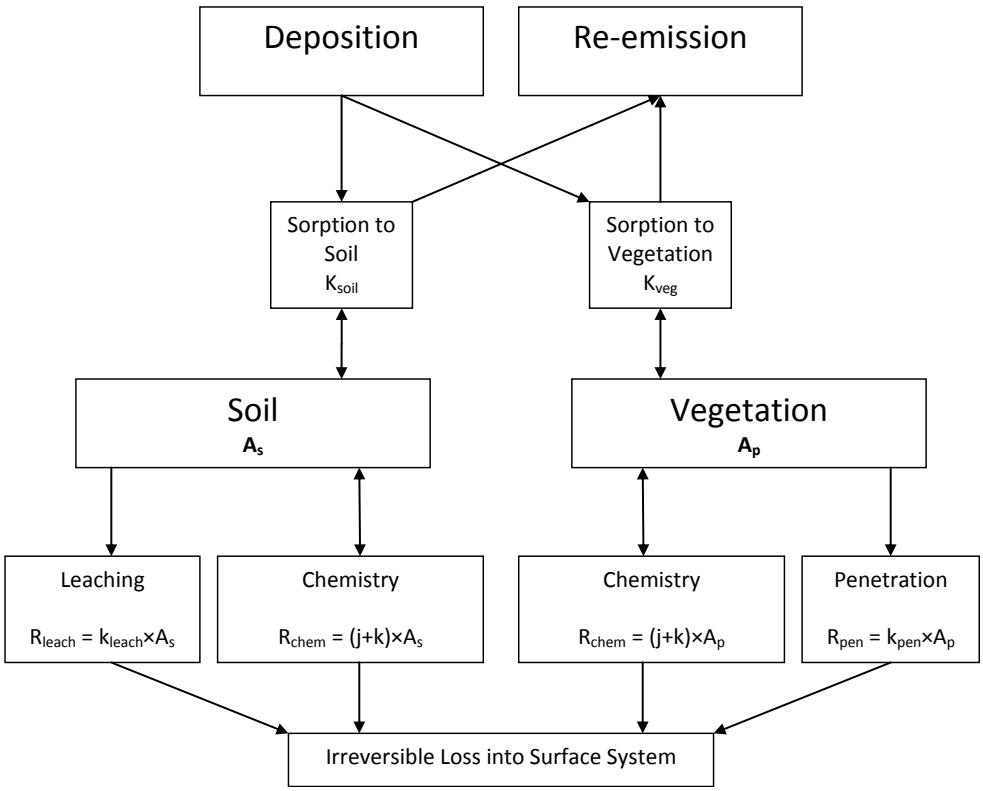

Figure 4.2: Schematic of the CAMx surface model. See Table 4.1 for explanations of each parameter.

Variable	Definition	Units
A_p	areic mass of compound on vegetation	$mol\ ha^{-1}$
A_s	areic mass of compound on soil	$mol\ ha^{-1}$
K_{veg}	vegetation-air partitioning coefficient	unitless
K_{soil}	soil-air partitioning coefficient	unitless
k_{leach}	leaching rate coefficient	min^{-1}
k_{pen}	leaf penetration rate coefficient	min^{-1}
j	photolysis chemistry rate coefficient	min^{-1}
R_{leach}	leaching rate	$mol\ ha^{-1}$
R_{pen}	penetration rate	$mol\ ha^{-1}$
R_{chem}	chemistry rate	$mol\ ha^{-1}$

Table 4.1: Description of CAMx surface model parameters.

		Surface Parameters	
Category No.	Land Cover Category	Soil Fraction	Shade Fraction
1	urban	0.7	0.2
2	agricultural	0.4	0.3
3	rangeland	0.7	0.2
4	deciduous forest	0.3	0.4
5	coniferous forest, wetland	0.2	0.5
6	mixed forest	0.3	0.4
7	water	n/a	n/a
8	barren land	0.9	0.0
9	non-forested wetlands	0.5	0.3
10	mixed agricultural/range	0.5	0.3
11	rocky (with low shrubs)	0.7	0.2

Table 4.2: CAMx landuse categories and associated default annual-averaged soil/vegetation split factors and shade factors.

are assumed to be seasonally constant, and values were estimated based on simple conceptual considerations of the amount of annual-averaged vegetation (i.e., leaf area index) typical of each category (Table 4.2).

The surface model uses partitioning (equilibrium) coefficients to calculate the amount of accumulated material adsorbed to soil and vegetation. The adsorbed fraction is subject to chemical reactions and physical removal associated with leaching deep into the soil and penetration into plant tissue. Chemistry can simply decay deposited material as a removal process, or it can generate products that may be subsequently re-emitted. All surface removal processes are assumed to be irreversible and result in a permanent removal of mass. The fraction not adsorbed to the surface media is subject to a volatilization flux (i.e., re-emission). Separate chemical-specific soil-air and vegetation-air partitioning coefficients are set in the CAMx chemistry parameters file. They represent the equilibrium ratio of chemical on a surface to chemical in air at the air-surface interface. For example, a compound with a partitioning coefficient of 10,000 (unitless) has an equilibrium concentration on the surface that is 10,000

Class	$t_{\frac{1}{2}}$	k	
very fast	0.04 d	17 d^{-1} =	1.2×10^{-2} min^{-1}
fast	0.21 d	3.3 d^{-1} =	2.3×10^{-3} min^{-1}
moderate	1.0 d	0.69 d^{-1} =	4.8×10^{-4} min^{-1}
slow	5.0 d	0.14 d^{-1} =	0.14×10^{-5} min^{-1}
very slow	25 d	0.03 d^{-1} =	0.03×10^{-5} min^{-1}

Table 4.3: Generalized classes of substance half-lives and process rates used in the CAMx surface model.

times more than that in air.

Chemistry, soil leaching, and plant penetration are dependent on chemical properties of the compounds and also on numerous site-specific factors such as soil and vegetation properties, highly transient meteorological conditions, etc. Often, these factors are unknown or fall within a range. The rates of these processes are defined as the process rate coefficient (k) times the mass on the surface area, or areic mass (A):

$$R_{process} = k_{process} \times \ A_{surface} \tag{4.9}$$

When the actual rate coefficients (or inversely the half-lives, $t_{\frac{1}{2}}$) are unknown for the substance, they are generalized by five classes shown in Table 4.3. A sixth class can be added by setting the k-value to zero or a *de minimis* value to effectively remove the process from consideration. In this manner chemicals can be modeled with an estimated half-life that is unique for each process.

Note that all portioning coefficients and reaction rates other than photolysis are fixed and ignore dependence on various environmental conditions (e.g., temperature, pressure, surface type, surface moisture). The user specifies photolysis rates to represent peak clear-sky values at zero zenith (solar noon) and are internally adjusted for solar angle, cloud attenuation, and shade fraction as a function of landuse type (Table 4.2).

The approach for re-emission of volatilized (un-adsorbed) mass is consistent with the CAMx dry deposition algorithm. Specifically, the surface model is tied to the Wesely (1989) option. Since the surface model does not consider water surfaces, re-emission fluxes from water are ignored in this implementation. In CAMx, dry deposition of material from the lowest model layer to the surface is treated as an irreversible first-order flux through the use of a dry deposition velocity. Deposition velocity is calculated similarly to an electric circuit according to Equation 4.10.

$$v_d = \frac{1}{r_a + r_b + r_s} \tag{4.10}$$

The r values represent transfer ‘‘resistances’’ for various components of the circuit path: turbulent transfer through the surface layer and into the canopy (r_a); diffusive transfer through the thin laminar layer in contact with the surface (r_b); and an effective adsorption resistance to a particular surface type (r_s). The deposition velocity is thus dependent on atmospheric conditions, species characteristics (e.g., diffusivity, reactivity, solubility), and surface characteristics (e.g., landuse type). Dry deposition includes adsorption to the surface, so it is considered a one-way irreversible process in CAMx.

Re-emission of volatilized mass is also treated as a first-order one-way flux using an ‘‘effective’’ velocity that is similar in form to v_d.

$$v_e = \frac{1}{r_a + r_b} \tag{4.11}$$

The r_s term is missing since only the pre-determined un-adsorbed fraction of surface mass is considered for surface-to-air transfer. The r_a and r_b terms are calculated by the surface model in exactly the same manner as the values used for dry deposition to ensure consistency.

Table 4.4 shows the species and reactions rate constants that were added to the

Species	K_{soil}	k_{leach}	K_{veg}	k_{pen}
NO_2	1.00×10^{10}	1.00×10^{-2}	1.00×10^{10}	1.00×10^{-2}
HNO_3	1.00×10^{10}	4.80×10^{-4}	1.00×10^{10}	4.80×10^{-4}
HONO	1.00×10^{0}	4.80×10^{-4}	1.00×10^{0}	4.80×10^{-4}
Precursor	Product	K_{rate}	J_{rate}	
NO_2	HONO	1.00×10^{-2}	1.00×10^{-2}	
HNO_3	HONO	0.0	4.80×10^{-5}	

Table 4.4: Surface model parameters and values that were added to CAMx in this study. Units are min^{-1}.

surface model in this study. This is a new feature of CAMx, and Table 4.4 summarizes the modifications to the base chemistry that were made. Three species, NO_2, HNO_3, and HONO, can now partition to soil or vegetation. The residence time for these species is about 1.5 days. Once on the surface, NO_2 and HNO_3 are converted to HONO. The photolysis rate for the NO_2 reaction, 1.0×10^{-2} min^{-1}, is three orders of magnitude greater than the photolysis rate for the HNO_3 reaction. These photolysis rates scale with total solar radiation. The kinetic reaction rate for HNO_3 is zero, which means surface adsorbed HNO_3 only forms HONO via photolysis. In addition to the permanent removal rates, k_{leach} and k_{pen}, all surface adsorbed species are removed following precipitation events. The reaction rate constants in Table 4.4 are estimates based upon extensive measurements from the 2009 SHARP campaign. They can and should be refined.

4.2.3 Process analysis

The CAMx simulations were run with the PA option turned on. When the PA option is enabled, CAMx creates a set of files during runtime that contains all simulated chemical and physical processes that influence O_3. See ENVIRON International Corporation (2013) for details regarding PA implementation in CAMx.

The use of PA outputs for analysis has been limited in its ability to characterize the transformations that occur within a changing PBL height, thus restricting investigations to a fixed height. The Python-based PA (pyPA) post-processing tool can aggregate multiple model layer heights permitting an hour-by-hour tracking of the PBL (Vizuete et al., 2008; Henderson et al., 2010, 2011). As the simulated PBL rises and falls, the analysis volume increases and decreases. It is useful to consider the entire column of grid cells within the simulated PBL because many of the model processes couple vertically adjacent cells on time scales shorter than one hour. The process analysis in this study aggregates all layers below the moving PBL.

4.2.4 SHARP measurements

From April 15 to May 31, 2009, continuous chemical and meteorological measurements were conducted as part of the SHARP campaign. The measurements were made atop Moody Tower on the downtown University of Houston campus. The measurement devices are 70 meters above ground level (a.g.l.), and were installed during the 2006 Texas Air Quality Study Radical Measurement Program (TRAMP). Lefer et al. (2010) describes in detail the *in situ* measurements. Remote sensing measurements were taken using long-path differential optical absorption spectroscopy (LP-DOAS) University of California, Los Angeles (Stutz et al., 2010). The LP-DOAS measurements provide vertically resolved HONO concentrations at three different height intervals: 20-70 meters a.g.l., 70-130 meters a.g.l., and 130-300 meters a.g.l. These heights are referred to as ‘‘lower,’’ ‘‘middle,’’ and ‘‘upper.’’

4.2.5 Simulation scenarios

Three different model runs were performed to determine the model's sensitivity to increased HONO concentrations. These runs are shown in Table 4.5 and described

Scenario	Emission Inventory	Surface Model
Run A	base	no
Run B	base + 0.8% $HONO:NO_x$	no
Run C	base	yes

Table 4.5: CAMx simulation scenarios

below. All runs used CAMx version 6.1 and used the same inputs unless otherwise noted.

- **Run A** is the basecase simulation. There were no changes to any of the inputs, and the new surface model was not implemented.

- **Run B** included direct $HONO$ emissions, but did not use the new surface model. $HONO$ is emitted directly and was added to the area (i.e. gridded low-level) emissions files in each of the three grids such that the $HONO:NO_x$ ratio is 0.8% (Pitts et al., 1984; Kurtenbach et al., 2001). The new emissions files were developed by ENVIRON and used in place of the area emissions files developed by AG.

- **Run C** utilized the new surface model described above, but did not include direct $HONO$ emissions. The area emissions files used were the same as those in Run A.

4.3 Results and Discussion

This study evaluated the impacts of new sources of $HONO$ in a 3-D air quality model. Simulated concentrations of NO_x, $HONO$, and O_3 were compared to measurements at Moody Tower. One day was selected to analyze in detail. This day, April 21, 2009, was chosen because it had high measured $HONO$ and O_3 concentrations.

Maximum measured *in situ* 1-hr HONO was 0.34 ppb, maximum 1-hr O_3 was 72 ppb, and maximum 8-hr O_3 was 69 ppb. These HONO and O_3 concentrations are the greatest that were measured during April, and among the highest recorded values during the entire SHARP campaign. Additionally, this day was recommended as a good candidate for analysis by researchers who are familiar with the the SHARP measurement dataset (Drs. Barry Lefer [University of Houston] and Jochen Stutz [UCLA], personal communication), and it has been studied in detail by Wong et al. (2012).

Model data was analyzed at the grid cell in which Moody Tower is located (see Figure 4.1b). The Moody Tower location is well suited for testing model performance because it is near the ship channel, which is the source region of many high O_3 events and non-typical O_3 changes. *In situ* measurements from the top of Moody Tower were compared to simulated concentrations in the second vertical layer. LP-DOAS measurements in the upper, middle and lower paths were compared to the fourth, third, and second vertical layers in the model. Normalized mean error (NME) was used as a metric to evaluate model performance and was calculated according to Equation 4.12.

$$NME = \frac{\sum_{i=1}^{N} |C_{m,i} - C_{o,i}|}{\sum_{i=1}^{N} C_{o,i}} \tag{4.12}$$

$C_{m,i}$ are modeled concentrations and $C_{o,i}$ are observed concentrations. $C_{m,i}$ and $C_{o,i}$ are space- and time-paired; if one is missing, the other is not considered. N is the total number of space- and time-paired concentrations.

Due to poor NO_x performance at the Moody Tower grid cell, we also analyzed simulation data from the grid cell directly southwest of Moody Tower. HONO formation

is strongly coupled to NO_2 concentrations, and, as shown in the following subsection, NO_2 performance is significantly better southwest of Moody Tower. Shifting to this grid cell removes unrealistic model behavior caused by artificially high NO_x and allows for a clearer understanding of the impacts of direct HONO emissions and heterogeneous formation on surfaces.

4.3.1 Nitrogen dioxide

Time-paired simulated and measured NO_2 concentrations are shown in Figure 4.3. Modeled NO_2 concentrations are over predicted at the Moody Tower grid cell as can be seen in Figures 4.3a, c, and e. Daytime (10 a.m. to 6 p.m.) concentrations are shown in red, and nighttime (7 p.m. to 9 a.m.) concentrations are shown in black. Daytime values are lower because of NO_2 photolysis. Figure 4.3a shows results from Run A, Figure 4.3c shows results from Run B, and Figure 4.3e shows results from Run C. NO_2 concentrations from Run B are nearly identical to those in Run A. Daytime values have a higher bias than do nighttime values. NME for Runs A and B (356% day, 197% night) were marginally lower than for Run C (363% day, 202% night). Clearly NO_2 performance is bad at Moody Tower. This is a known issue with the AG 2009 ensemble modeling. The high concentrations are the result of elevated NO_x emissions coming from ship channel activity (shipping, fork lifts, cranes, etc.) 6 km east of Moody Tower. The emissions are restricted to the row of grid cells in which the Moody Tower grid cell is located.

The grid cell directly to the southwest of Moody Tower had much better NO_x performance. Figures 4.3b, d, and f compare NO_2 concentrations simulated in this grid cell to *in situ* measurements taken at Moody Tower. Maximum simulated NO_2 concentrations in the grid cell southwest of Moody Tower are 31 ppb, which is 30 ppb less than maximum NO_2 predictions at Moody Tower. NME is significantly lower,

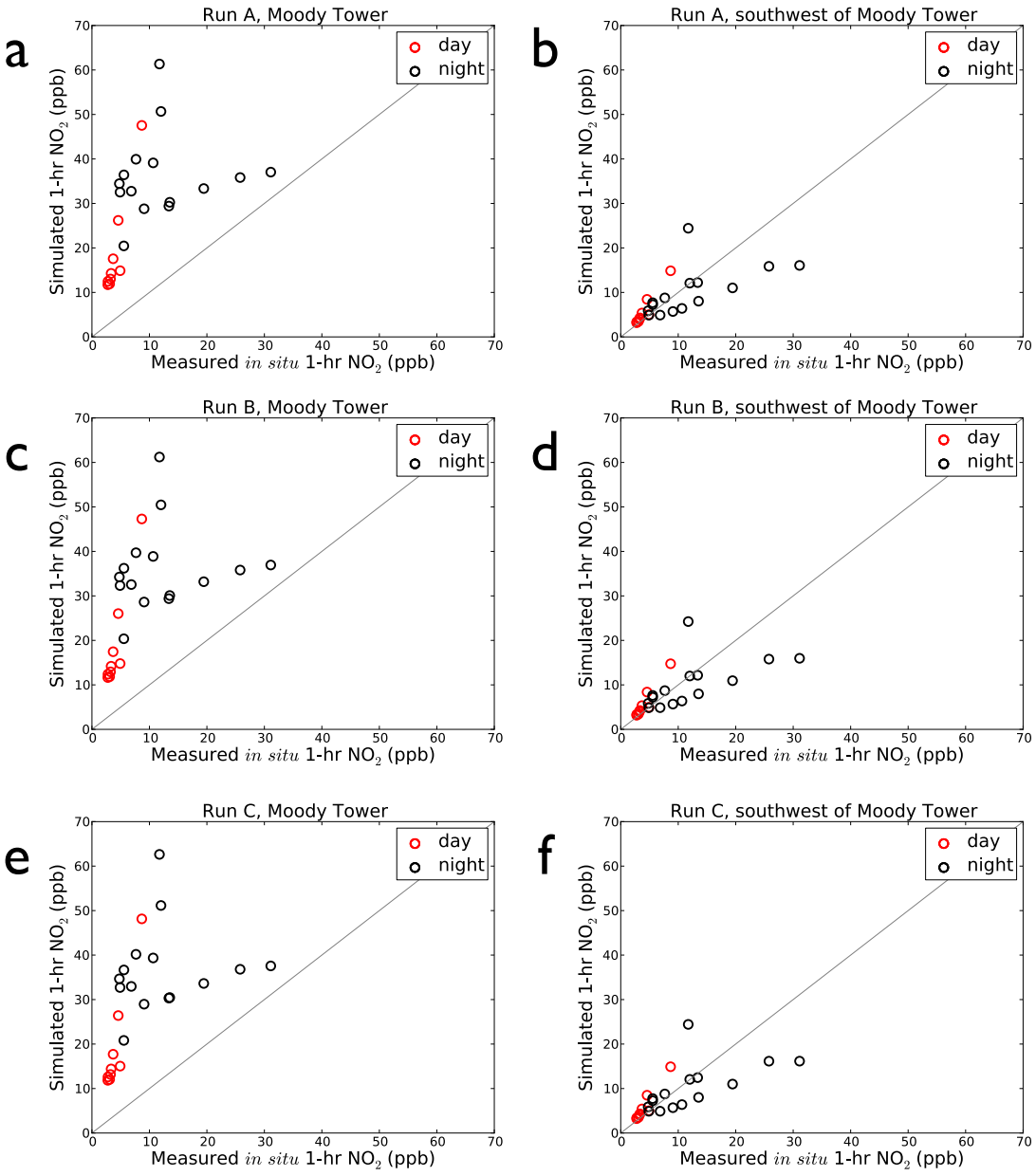

Figure 4.3: April 21, 2009, NO_2 model performance for Run A (top), Run B (middle), and Run C (bottom) at Moody Tower (left) and the grid cell to the southwest of Moody Tower (right). Daytime (10 a.m. to 6 p.m.) values are shown in red; nighttime (7 p.m. to 9 a.m.) values are shown in black.

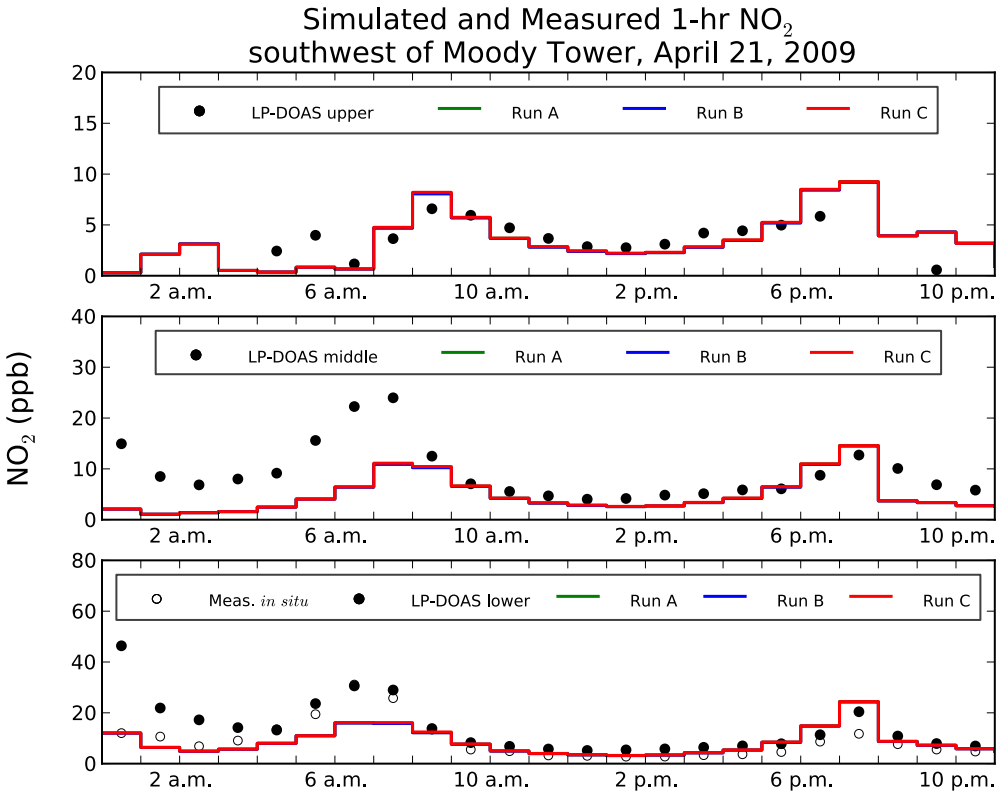

Figure 4.4: April 21, 2009, NO_2 time series for LP-DOAS and *in situ* measurements (black circles and open circles), Run A (green line), Run B (blue line), and Run C (red line) at the grid cell southwest of Moody Tower. The upper, middle, and lower LP-DOAS paths are shown and are paired with the fourth, third, and second vertical model layers.

too. Daytime and nighttime error in all three scenarios is 40% and 38% .

NO_2 time series at the grid cell southwest of Moody Tower are shown in Figure 4.4. The shaded circles show vertically resolved measurements taken with UCLA's LP-DOAS, and the open circles are *in situ* measurements taken at the top of Moody Tower. Simulation data are taken from model layers two through four. In all layers, differences between the three model runs are very small; the maximum NO_2 difference is less than 0.4 ppb. NO_2 concentrations decrease vertically because it is emitted at the ground level mainly from automobiles. Model concentrations are biased low in the morning, but improve during the day and at night.

Modeled NO concentrations exhibit similar behavior (not shown). Over predictions exist in both grid cells for Runs A, B, and C, but model performance is better in the grid cell southwest of Moody Tower because of the elevated NO_x ship channel emissions mentioned above.

4.3.2 Nitrous acid

HONO performance for the three model runs varies substantially. Figure 4.5 compares time-paired HONO concentrations to *in situ* measurements. Plots on the left hand side of the figure shows simulated concentrations from the Moody Tower grid cell; the righthand side shows predictions from the grid cell to the southwest of Moody Tower where NO_x performance was better. Run A (Figures 4.5a and b) indicates a low bias especially at night. This is consistent with previous modeling studies that found homogeneous HONO formation insufficient to produce measured concentrations. There is little difference between the two grid cells in Run A, though the grid cell southwest of Moody Tower has slightly lower HONO values. NO_x concentrations are lower in this grid cell, and HONO formation in Run A is directly dependent upon NO_x (see Reactions 4.2 and 4.3). Daytime NME at Moody Tower and the grid cell

southwest of Moody Tower is 39% and 66% ; nighttime NME is 87% and 94% .

HONO is over predicted at Moody Tower in Run B (Figure 4.5c). In this scenario, HONO is directly emitted as a fraction of NO_x. Since NO_x concentrations are biased high, it follows that HONO should be as well. NME in the Moody Tower grid cell is 127% during the day and 75% at night. Figure 4.5d shows HONO performance in the grid cell southwest of Moody Tower. HONO performance is greatly improved in this grid cell. NME drops to 31% during the day and 64% at night.

Run C HONO nighttime performance at the grid cell southwest of Moody Tower (Figure 4.5f) is better than at Moody Tower (Figure 4.5d), but daytime performance is slightly worse. Daytime NME is 37% and 22% southwest of and at Moody Tower, while nighttime NME is 161% and 277%. Over predictions at night suggest the surface model is making too much HONO. The only nighttime HONO formation mechanism is thermal conversion of NO_2. Thus, it is likely that the $K_{NO_2 \rightarrow HONO}$ in Table 4.4 is too large.

Figure 4.6 shows hourly simulated and measured HONO concentrations. One set of measurements was taken with UCLA's LP-DOAS and is vertically resolved at three different heights (shaded circles); the other (*in situ*) was taken atop Moody Tower (open circles). Only simulation data from the grid cell southwest of Moody Tower is shown. HONO values decrease with height because most HONO formation occurs near the ground where NO_x concentrations are greatest. In the bottom plot, maximum daytime (10 a.m. to 6 p.m.) HONO concentrations are 0.06 ppb, 0.10 ppb, and 0.11 ppb for Runs A, B, and C. Each of these is below the maximum observed daytime value of 0.14 ppb.

Run A (green line) under predicts HONO, especially in the early morning. Accuracy improves during the middle of the day when $^{\cdot}OH$ concentrations reach maximum levels indicating the importance of homogeneous HONO formation (e.g. Reaction 4.2).

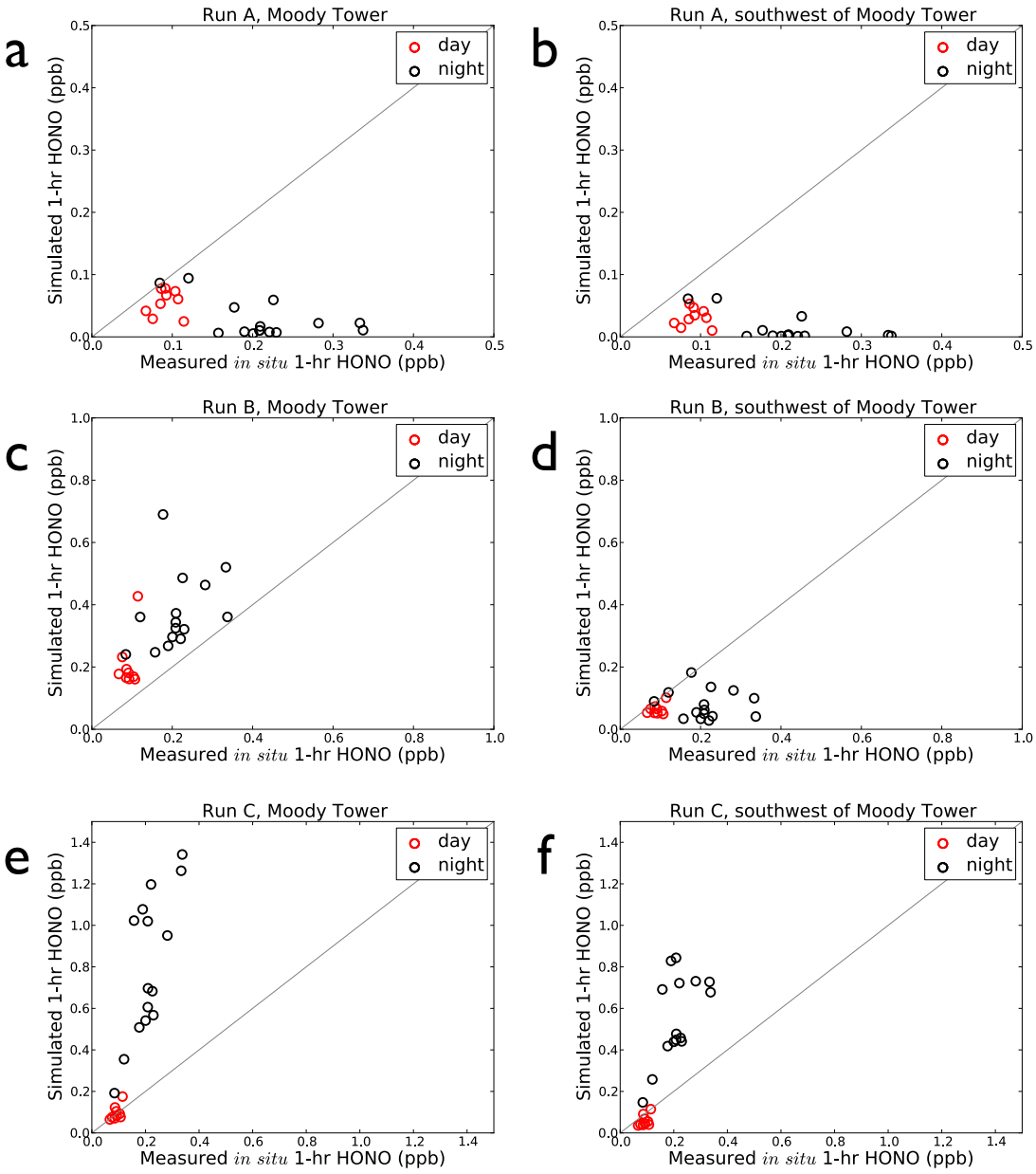

Figure 4.5: April 21, 2009, HONO model performance for Run A (top), Run B (middle), and Run C (bottom) at Moody Tower (left) and the grid cell to the southwest of Moody Tower (right). Daytime (10 a.m. to 6 p.m.) values are shown in red; nighttime (7 p.m. to 9 a.m.) values are shown in black.

Run B (blue line) under predicts HONO during the morning and at night, though noticeable increases coincide with rush hour traffic (April 21, 2009, was a Tuesday). In Run C, HONO values increase in the early morning suggesting the photolytic conversion of adsorbed HNO_3 and NO_2 (Reactions 4.4 - 4.8). Similar to Figures 4.5e and f, nighttime HONO concentrations are over predicted. All three scenarios fail to match the measurements before sunrise and after sunset. Runs A and B under predict during these times, which indicates that direct emissions and homogeneous HONO formation are not sufficient to produce observed concentrations. Run C over predicts HONO during the early morning and night. As mentioned above, this is likely because the reaction rate constant for thermal NO_2 conversion is too large.

In Figure 4.7, HONO concentrations are plotted agains NO_2 concentrations for all three model runs and *in situ* measurements. Simulation data is taken from the grid cell southwest of Moody Tower. HONO:NO_2 ratios can be used to evaluate model performance, but error in both variables - HONO and NO_2 - must be considered. During the day, Figure 4.7 shows the ratio is under predicted in the model. Figures 4.4 and 4.6 (lower plots) show why. The three model runs have similar HONO and NO_2 concentrations from about 10 a.m. to 6 p.m. Daytime NO_2 values are over predicted with respect to the *in situ* measurements, but HONO is under predicted. The low HONO:NO_2 ratios for Runs A and B in the early morning and night are due to low HONO concentrations. Run C has opposite behavior. Ratios are over predicted because too much HONO is created before sunrise and after sunset.

4.3.3 Ozone production and hydroxyl radical cycling

O_3 concentrations for both sets of measurements (at Moody Tower) and all model scenarios (southwest of Moody Tower) are shown in Figure 4.8. The three model runs have similar O_3 concentrations, though Run C is 1-2 ppb higher at every hour in the

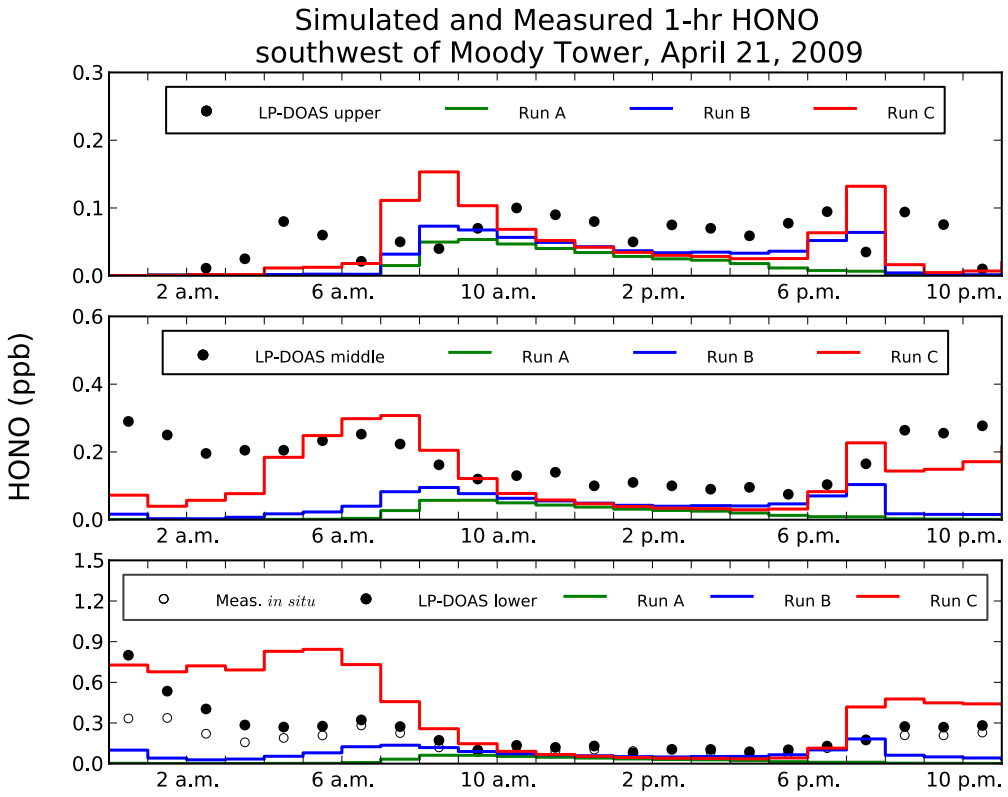

Figure 4.6: April 21, 2009, HONO time series for LP-DOAS and *in situ* measurements (black circles and open circles), Run A (green line), Run B (blue line), and Run C (red line) at the grid cell southwest of Moody Tower. The upper, middle, and lower LP-DOAS paths are shown and are paired with the fourth, third, and second vertical model layers.

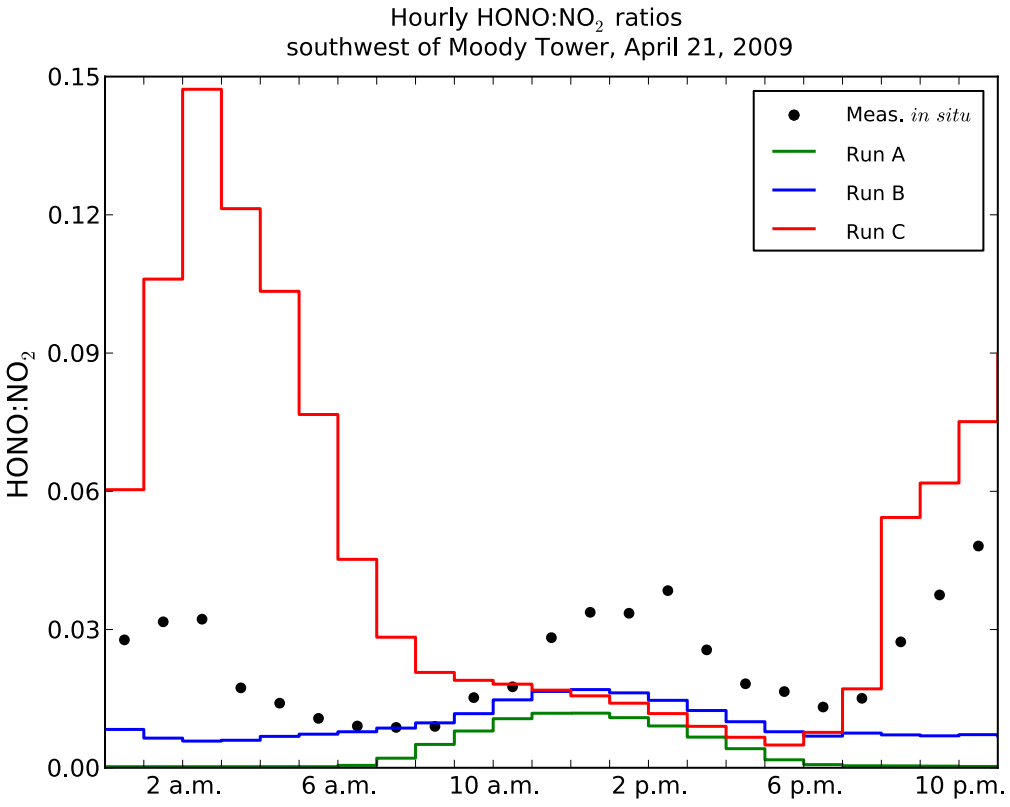

Figure 4.7: April 21, 2009, HONO:NO_2 time series for all three model runs and *in situ* measurements at Moody Tower.

second model layer (bottom plot). At 8 a.m. and 9 a.m., O_3 in second-layer Run B is 0.3 ppb greater than in Run A. These are the hours following rush hour traffic during which HONO is directly emitted in Run B. As the sun rises, this additional HONO quickly photolyzes creating the $^{\cdot}OH$ radical. O_3 in Run C is 2.5 ppb greater than Run A at 8 a.m. and 9 a.m. (and, therefore, 2.2 ppb greater than Run B) because of the immediate photolysis of the heterogeneously formed ground-layer HONO.

All three scenarios under predict O_3 from 12 p.m. to 7 p.m., especially in the lower (second) model layer. Daytime under predictions for Run C range from 7 ppb to 23 ppb when compared to the *in situ* measurements during this window. A sudden drop in O_3 occurs at 7 p.m. because modeled NO concentrations increase almost threefold from 9.7 ppb to 26.1 ppb. (NO is readily oxidized by O_3.) This is clearly due to rush hour emissions because the O_3 decrease is muted in the middle (third) or upper (fourth) layers, which are less affected by ground layer emissions. Overall, however, O_3 performance is good. Lower layer NME for all three runs is 12-13% regardless of which set of measurements is used.

O_3 PA time series plots are shown in Figure 4.9 for the grid cell southwest of Moody Tower. In these plots, all model layers below the PBL have been aggregated using pyPA, which creates a column of grid cells whose height varies with the rising and falling PBL. Four net processes are shown: chemistry, horizontal transport (advection and diffusion), vertical transport (advection and diffusion), and the net effect of vertical dilution (increased volume due to rising PBL) and entrainment (pollutant gain/loss due to height of column rising/falling). The black diamonds show modeled O_3 concentrations at the beginning of each hour. The hourly O_3 increase or decrease is the net contribution of all model processes.

Figure 4.9a shows model O_3 processes for Run C. Before 9 a.m. and after 5 p.m., chemistry has a net destructive effect on O_3. The magnitude of chemical destruction

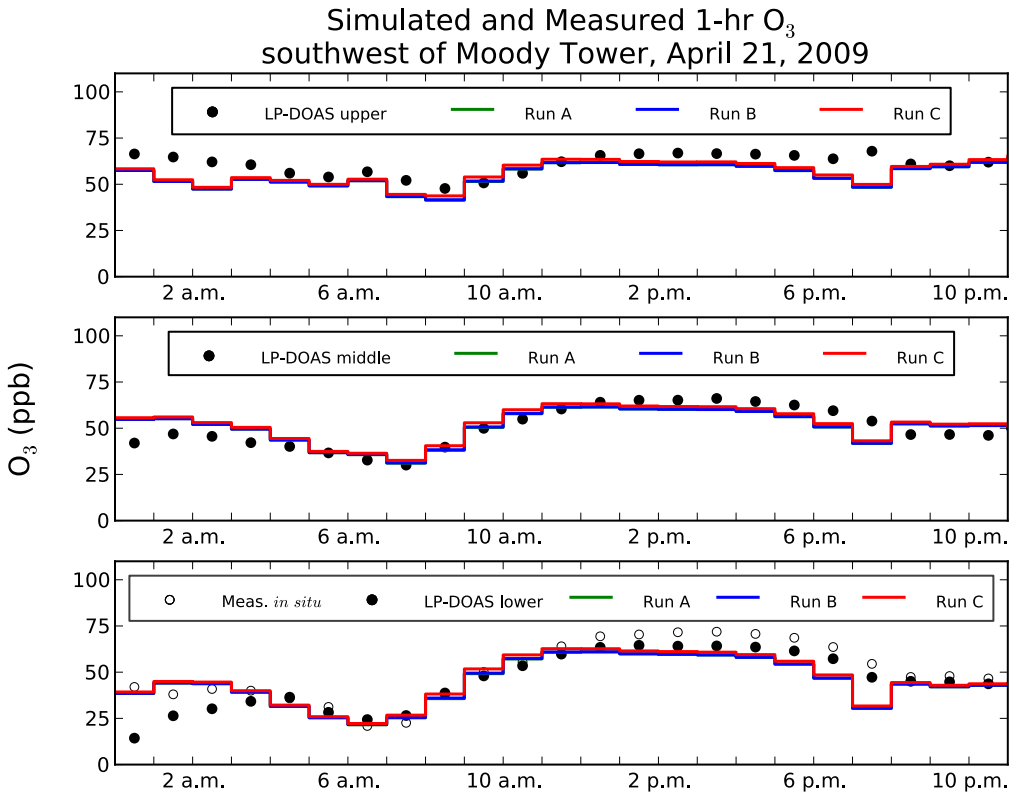

Figure 4.8: April 21, 2009, O_3 time series for LP-DOAS and *in situ* measurements (black circles and open circles) at the Moody Tower grid cell. Run A (green line), Run B (blue line), and Run C (red line) predictions are shown for the grid cell southwest of Moody Tower. The upper, middle, and lower LP-DOAS paths are shown and are paired with the fourth, third, and second vertical model layers.

is at a maximum during morning and evening rush hour traffic when large amounts of NO are emitted at the surface. Most of the O_3 increase occurs from 7 a.m. (27 ppb) to 10 a.m. (58 ppb). During this three hour period, horizontal transport adds 53 ppb, vertical dilution/entrainment adds 20 ppb, chemistry removes 11 ppb, and vertical transport removes 30 ppb. The net contribution of these four processes explains the 31 ppb rise in O_3. (There are other model processes that contribute to changes in O_3 concentration, e.g., dry deposition, but their effect is minor and not shown.) O_3 values remain relatively constant from 11 a.m. to 6 p.m. During this period, horizontal transport and vertical dilution/entrainment serve to remove O_3, but chemical production is positive. Thus, the net effect is little change in O_3 concentrations. Vertical transport is negligible during from 11 a.m. to 6 p.m. The O_3 decrease at 7 p.m. is due to chemical destruction, vertical transport, and vertical dilution/entrainment (as the PBL collapses, O_3 is ''left behind'' in upper model layers). Some, but not all, of the O_3 lost is replaced by horizontal transport.

Model process differences between Runs C and A are shown in Figure 4.9b. Here, O_3 concentrations and model process rates from Run A were subtracted from those in Run C. The differences show the model's response to HONO production from the surface model since heterogeneous HONO formation is the only difference between the model runs. From midnight to 6 a.m., Run C O_3 values are nearly 1 ppb greater. From 6 a.m. to 9 a.m., this difference increases to almost 3 ppb. During this time chemical production and horizontal transport in Run C was 2 ppb and 1 ppb greater than in Run A; vertical transport and vertical dilution/entrainment in Run C were each about 0.5 ppb less than in Run A. The net effect, then, was to increase O_3 concentrations by about 2 ppb in Run C relative to Run A. The hours after sunrise show large O_3 concentration and model process differences. This is expected because the ''new'' HONO created by the surface model in Run C photolyzes quickly in the

morning and immediately impacts radical budgets.

An integrated reaction rate analysis was performed to find out how direct HONO emissions and heterogeneous formation affect radical budgets and oxidative chemistry. Figure 4.10 shows the $^{\cdot}OH$ cycle for the three model scenarios. This diagram shows how $^{\cdot}OH$ behavior changes as a result of additional HONO. Initiation is the genesis of a new $^{\cdot}OH$ and often occurs via photolysis as in Reaction 4.1. The new $^{\cdot}OH$ then enters the oxidation cycle where it can be terminated or propagated. During propagation, $^{\cdot}OH$ is temporarily lost through VOC oxidation, but is recreated within the same reaction chain. The recreated $^{\cdot}OH$ reenters the oxidation cycle and, again, can terminate or propagate. $^{\cdot}OH$ propagation also involves NO to NO_2 conversion. An example of this process is illustrated in Reactions 4.13 - 4.16.

$$^{\cdot}OH + HC(=O)H \rightarrow HC(=O)^{\cdot} + H_2O \tag{4.13}$$

$$HC(=O)^{\cdot} + O_2 \rightarrow HO_2^{\cdot} + CO \tag{4.14}$$

$$HO_2^{\cdot} + NO \rightarrow NO_2 + {}^{\cdot}OH \tag{4.15}$$

$$^{\cdot}OH + NO_2 \rightarrow HNO_3 \tag{4.16}$$

Reactions 4.13 - 4.15 show how the oxidation of a VOC - in this case CH_2O - consumes $^{\cdot}OH$, converts NO to NO_2, and recreates $^{\cdot}OH$. This process is propagation. If $^{\cdot}OH$ reacted with NO_2 as in Reaction 4.16, it would be removed from the system permanently, i.e., terminated.

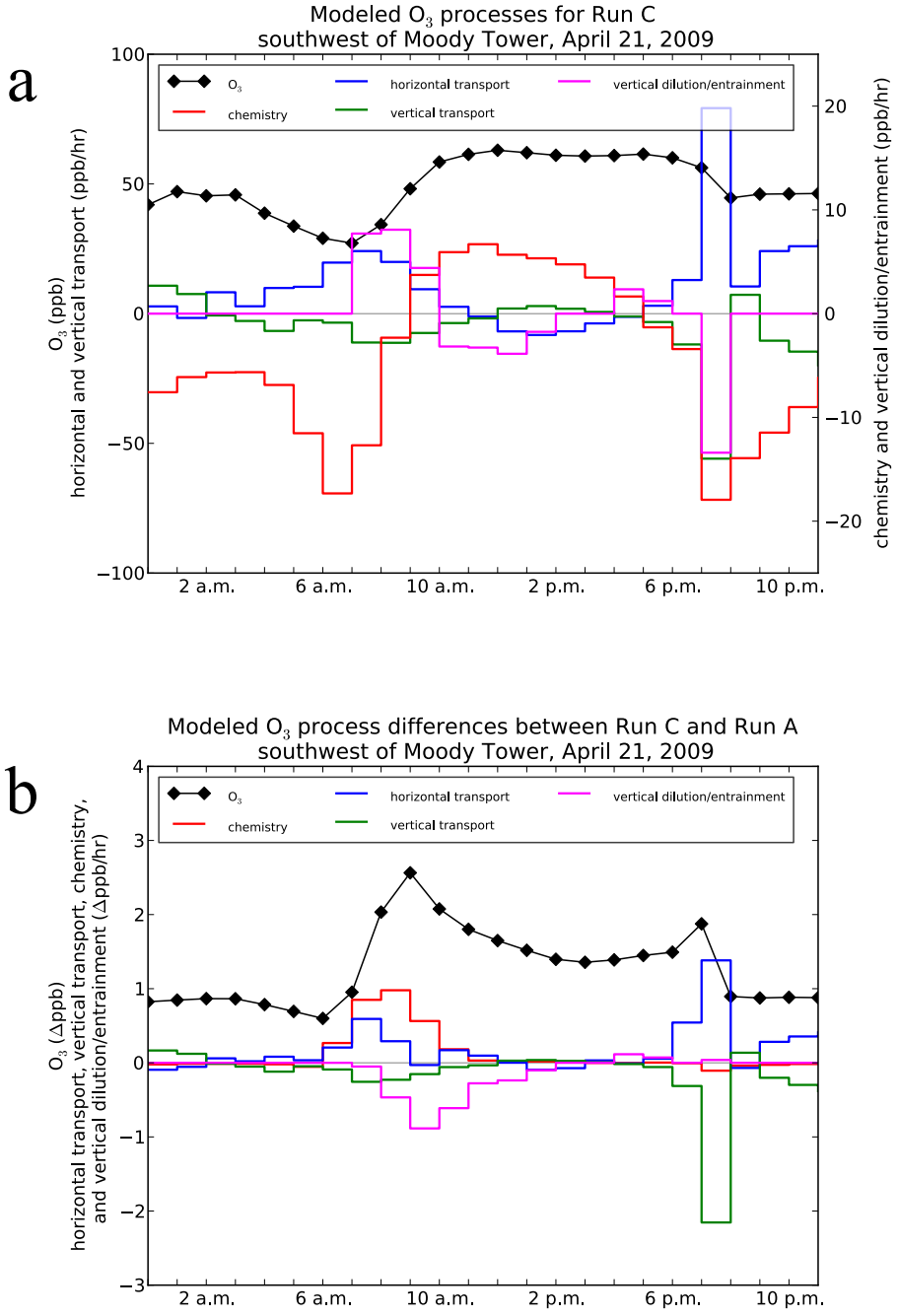

Figure 4.9: (a) April 21, 2009, O_3 process analysis plot for Run C at the grid cell southwest of Moody Tower. (b) Like plot (a), but values from Run A have been subtracted from Run C. In both plots, data is vertically aggregated up to the PBL. Black diamonds show modeled O_3 concentrations at the beginning of each hour. Contributions from chemistry (red), horizontal transport (blue), vertical transport (green), and the net effect of vertical dilution and entrainment (magenta) are shown.

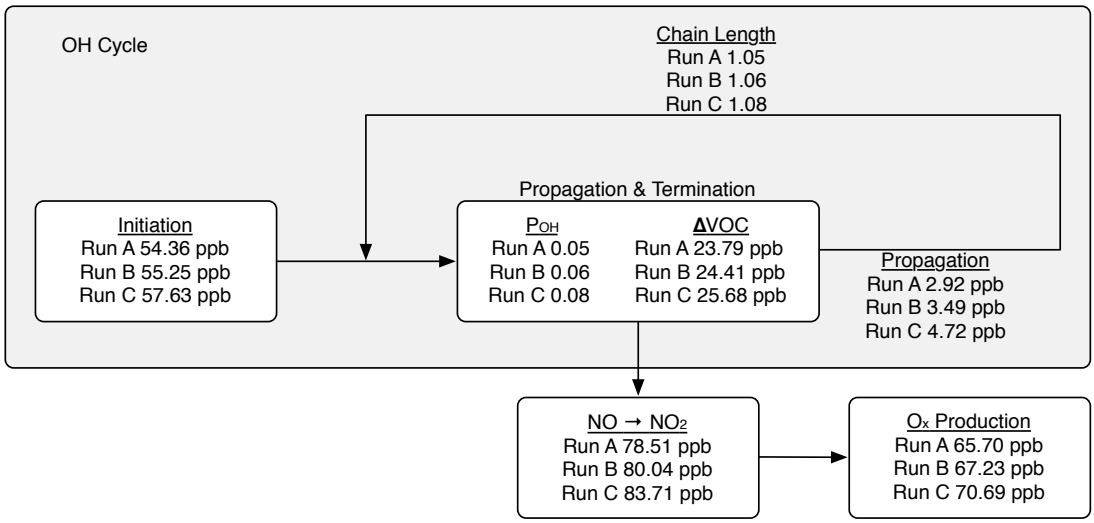

Figure 4.10: ·OH cycle diagram for the process analysis column (i.e., aggregation of all model layers up to the PBL) in the grid cell southwest of Moody Tower. Initiation represents new creation of new ·OH; propagation represents recreation of ·OH; chain length represents the average number of times an ·OH molecule is propagated before it is removed permanently (terminated); $P_{\cdot OH}$ is the propagation factor, $\frac{Propagation}{Propagation+Initiation}$; ΔVOC represents the amount of VOC that was oxidized by ·OH; NO $\rightarrow$ NO_2 represents the total oxidation of NO to NO_2; and O_x production represents the net production of O_x. Values are the 24-hour sum of hourly integrated reaction rates. VOC is the sum of the following Carbon Bond 6 species: PAR, ETHA, MEOH, ETOH, ETH, OLE, IOLE, ISOP, TERP, FORM, ALD2, ALDX, TOL, XYL, PRPA, ETHY, BENZ, ACET, KET. O_x is the sum of the following Carbon Bond 6 species: O_3, O, $O(^1D)$, NO_2, $2{\cdot}NO_3^*$, $3{\cdot}N_2O_5$, HNO_3, $2{\cdot}$PNA, PAN.

Figure 4.10 indicates that Run C had the most active $^{\cdot}OH$ cycle. The values in the figure are 24-hour sums of hourly integrated reaction rates taken from the aggregation of all model layers below the PBL at the grid cell southwest of Moody Tower. $^{\cdot}OH$ initiation was 57.63 ppb. A molecule of $^{\cdot}OH$ entering the oxidation cycle had an 8% chance of being recreated. A total of 4.72 ppb $^{\cdot}OH$ was propagated through the system, which gives a chain length of 1.08. Overall, 25.68 ppb VOC[1] were oxidized by $^{\cdot}OH$, 83.71 ppb NO was converted to NO_2, and 70.69 O_x[2] was produced. NO to NO_2 conversion values do not consume O_x, e.g., $NO + O_3 \rightarrow NO_2$ is not included.

The values for Runs A and B in Figure 4.10 are all less than those for Run C. Less $^{\cdot}OH$ was initiated and propagated, fewer molecules of VOC were oxidized, less NO was converted to NO_2, and O_x production was lower. Values in Run B were greater than Run A. This means that additional HONO sources had a measurable effect on radical budgets, and heterogeneous formation on the surface had a greater effect than direct emissions.

Hourly $^{\cdot}OH$ initiation and VOC oxidation are shown in Figure 4.11. The values in the figure are the hourly integrated reaction rates taken from the aggregation of all model layers below the PBL at the grid cell southwest of Moody Tower. The largest differences between the model runs occur at the start of the photochemical day. Beginning at 6 a.m., there is a four hour period during which $^{\cdot}OH$ initiation from HONO photolysis is significantly greater in Run C because there is more HONO available (see Figure 4.6). During this four hour period, 1.89 ppb $^{\cdot}OH$ is created from HONO photolysis , which is 67% of the daily total $^{\cdot}OH$ initiated from this

[1] VOC is the sum of the following Carbon Bond 6 species: PAR, ETHA, MEOH, ETOH, ETH, OLE, IOLE, ISOP, TERP, FORM, ALD2, ALDX, TOL, XYL, PRPA, ETHY, BENZ, ACET, KET.

[2] Odd oxygen, O_x, is a measure of the oxidative capacity of the atmosphere. It contains species with an oxygen atom available to serve as an oxidizing agent. Here, O_x is the sum of the following Carbon Bond 6 species: O_3, O, $O(^1D)$, NO_2, $2{\cdot}NO_3^{\cdot}$, $3{\cdot}N_2O_5$, HNO_3, $2{\cdot}$PNA, PAN. $NO_3^{\cdot}$, N_2O_5, and PNA contain more than one reactive oxygen atoms and are counted multiple times to represent the total number of reactive oxygen atoms.

reaction. In Runs A and B that percentage is only 35% and 45%. By 11 a.m., HONO concentrations are about equal in Runs B and C, and it is during this hour that the integrated reaction rates for HONO photolysis in the two model runs become similar. At this point, the excess HONO in Run C has photolyzed and generated new ·OH. HONO photolysis rates in Run A are always below Runs B and C because Run A only has gas-phase HONO formation, and, thus, always has lower HONO concentrations.

Figure 4.11 also shows the amount of VOC oxidized by ·OH for the three model runs. As with HONO photolysis, the differences appear during the first few hours following sunrise. The extra ·OH created from HONO in Run C quickly begins to attack VOCs. At around 11 a.m., the reservoir of nighttime Run C HONO is depleted, ·OH initiation approaches values found in Runs A and B, and VOC oxidation levels also align with those in Runs A and B.

4.4 Conclusion

This study demonstrated the successful implementation of new HONO sources in a regulatory air quality model. Direct emissions and heterogeneous chemical formation on surfaces each improved modeled HONO performance. Daytime HONO concentration increases were seen to propagate vertically. That is, additional HONO was not confined to the surface model layer where it was created. In the lower vertical layers (ground and second layers), though, increased HONO concentrations were especially apparent at night. This was not true in the upper layers (third and fourth), which could indicate there are still important HONO formation mechanisms that are missing from the model (e.g. aerosol surfaces).

For the first time, a surface model representing the physical and chemical HONO formation processes has been developed and implemented in CAMx. This work provided proof of concept and met two key goals. First, we assessed the impor-

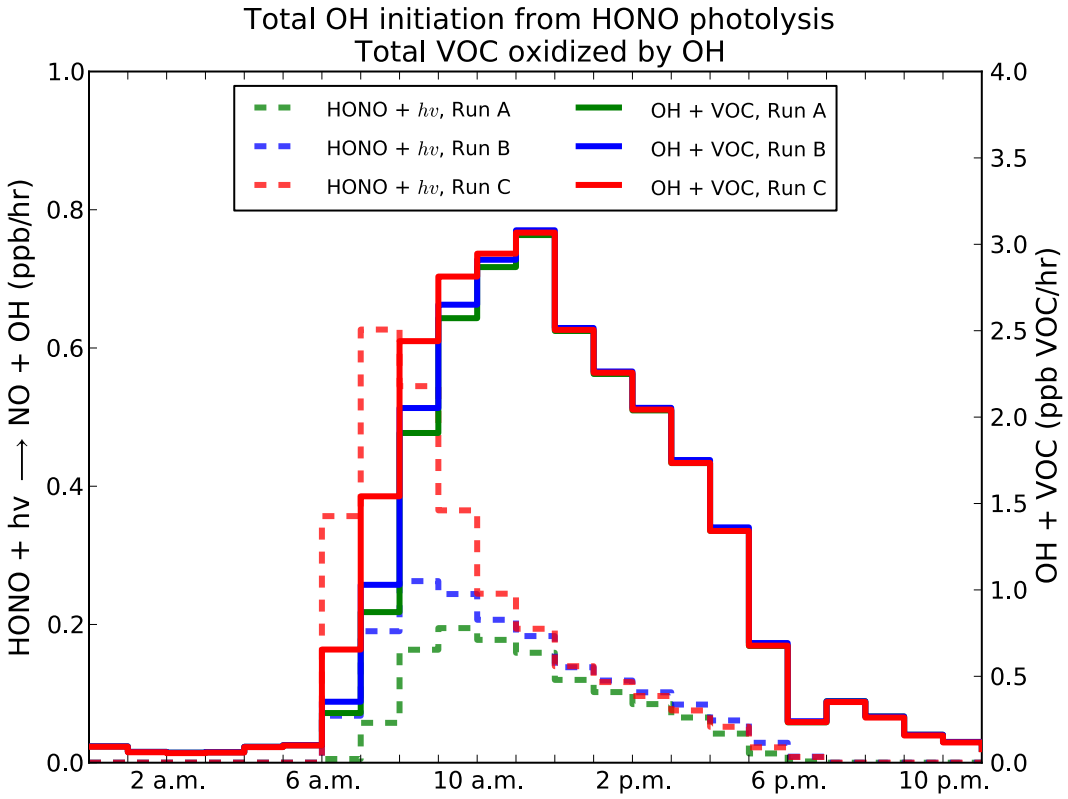

Figure 4.11: Hourly rates of ·OH initiation from HONO photolysis and VOC oxidized by ·OH. Data is from April 21, 2009, in the grid cell southwest of Moody Tower and is vertically aggregated up to the PBL.

tance of direct HONO emissions and photo-enhanced heterogeneous HONO formation. And, second, we quantified the impacts of the new HONO sources on the oxidative environment.

Increased HONO led to increases in the overall reactivity of the system. Changes in $^{\cdot}$OH initiation, propagation, and chain lengths were found, especially in the hours following sunrise. The additional HONO led to greater overall NO to NO_2 conversions and O_x production. The surface model generated more HONO than direct emissions and also led to greater increases in O_x. Heterogeneous HONO formation led to 1-hr O_3 increases of nearly 3 ppb, and direct emissions led to 1-hr O_3 increases up to 0.3 ppb.

This was only a first step in assimilating heterogeneous HONO chemistry into a 3-D modeling framework, but will guide further efforts to improve air quality models. Pending further testing and a reevaluation of surface reaction rate constants, this surface model could be an important feature of future regulatory modeling frameworks. A next step will evaluate changes to modeled non-typical O_3 (NTOC) performance as a result of the new HONO sources. Given the link between NTOCs and rapid VOC oxidation, an increase in model reactivity should improve the model's ability to simulate that phenomenon. This is an especially interesting question because the additional HONO affected modeled chemistry most in the morning, which is when most NTOCs occur.

REFERENCES

B. Alicke, A. Geyer, A. Hofzumahaus, F. Holland, S. Konrad, H. W. Patz, J. Schafer, J. Stutz, A. Volz-Thomas, and U. Platt (2003). OH formation by HONO photolysis during the BERLIOZ experiment. *J. Geophys. Res.*, 108(D4):8247. doi:10.1029/2001JD000579.

H. J. Beine, F. Domine, W. Simpson, R. E. Honrath, R. Sparapani, X. Zhou, and M. King (2002). Snow-pile and chamber experiments during the Polar Sunrise Experiment 'Alert 2000': exploration of nitrogen chemistry. *Atmos. Environ.*, 36:2707--2719.

W. Carter (2010). Development of the SAPRC-07 chemical mechanism. *Atmos. Environ.*, 44(40):5324--5335. doi:10.1016/j.atmosenv.2010.01.026.

M. Concalves, D. Dabdub, W. L. Chang, O. Jorba, and J. M. Baldasano (2012). Impact of HONO sources on the performance of mesoscale air quality models. *Atmos. Environ.*, 54:168--176. doi:10.1016/j.atmosenv.2012.02.079.

E. Couzo, H. E. Jeffries, and W. Vizuete (2013). Houston's rapid ozone increases: preconditions and geographic origins. *Environ. Chem.*, 10:260--268. doi:10.1071/EN13040.

E. Couzo, A. Olatosi, H. E. Jeffries, and W. Vizuete (2012). Assessment of a regulatory model's performance relative to large spatial heterogeneity in observed ozone in Houston, Texas. *J. Air Waste Manag. Assoc.*, 62:696--706. doi:10.1080/10962247.2012.667050.

B. H. Czader, B. Rappengluck, P. Percell, D. W. Byun, F. Ngan, and S. Kim (2012). Modeling nitrous acid and its impact on ozone and hydroxyl radical during the Texas Air Quality Study 2006. *Atmos. Chem. Phys.*, 12:6939--6951. doi:10.5194/acp-12-6939-2012.

J. E. Dibb, M. Arsenault, M. C. Peterson, and R. E. Honrath (2002). Fast nitrogen oxide photochemistry in Summit, Greenland snow. *Atmos. Environ.*, 36:2501--2511.

ENVIRON International Corporation (2013). CAMx Users Guide: Comprehensive Air Quality Model with Extensions, version 6.0. Novato, CA: ENVIRON International Corporation.

C. George, R. S. Strekowski, J. Kleffmann, K. Stemmler, and M. Ammann (2005). Photoenhanced uptake of gaseous NO_2 on solid organic compounds: a photochemical source of HONO? *Faraday Discuss.*, 130:195--210. doi:10.1030/b417888m.

G. W. Harris, W. Carter, A. M. Winer, and J. N. Pitts, Jr. (1982). Observations of nitrous acid in the Los Angeles atmosphere and implications for predictions of ozone-precursor relationships. *Environ. Sci. Technol.*, 16:414--419.

R. M. Harrison, J. D. Peak, and G. M. Collins (1996). Tropospheric cycle of nitrous acid. *J. Geophys. Res.*, 101(D9):14429--14439.

Y. He, X. Zhou, J. Hou, H. Gao, and S. B. Bertman (2006). Importance of dew in controlling the air-surface exchange of HONO in rural forested environments. *Geophys. Res. Lett.*, 33:L02813. doi:10.1029/2005GL024348.

B. H. Henderson, H. E. Jeffries, B. U. Kim, and W. Vizuete (2010). The influence of model resolution on ozone in industrial volatile organic compound plumes. *J. Air Waste Manag. Assoc.*, 60:1105--1117. doi:10.3155/1047-3289.60.9.1105.

B. H. Henderson, Y. Kimura, E. McDonald-Buller, D. T. Allen, and W. Vizuete (2011). Comparison of Lagrangian process analysis tools for Eulerian air quality models. *Atmos. Environ.*, 45:5200--5211. doi:10.1016/j.atmosenv.2011.06.005.

R. Kurtenbach, K. H. Becker, J. A. Gomes, J. Kleffmann, J. C. Lorzer, M. Spittler, P. Wiesen, R. Ackermann, A. Geyer, and U. Platt (2001). Investigations of emissions and heterogeneous formation of HONO in a road traffic tunnel. *Atmos. Environ.*, 35:3385--3394.

B. Lefer, B. Rappengluck, J. Flynn, and C. Haman (2010). Photochemical and meteorological relationships during the Texas-II Radical and Aerosol Measurement Project (TRAMP). *Atmos. Environ.*, 44:4005--4013. doi:10.1016/j.atmosenv.2010.03.011.

G. Li, W. Lei, M. Zavala, R. Volkamer, S. Dusanter, P. Stevens, and L. T. Molina (2010). Impacts of HONO sources on the photochemistry in Mexico City during the MCMA-2006/MILAGO campaign. *Atmos. Chem. Phys.*, 10:6551--6567. doi:10.5194/acp-10-6551-2010.

Y. Li, J. An, M. Min, W. Zhang, F. Wang, and P. Xie (2011). Impacts of HONO sources on the air quality in Beijing, Tianjin and Hebei Province of China. *Atmos. Environ.*, 45:4735--4744. doi:10.1016/jatmosenv.2011.04.086.

J. N. Pitts, Jr., H. W. Biermann, A. M. Winer, and E. C. Tuazon (1984). Spectroscopic identification and measurement of gaseous nitrous acid in dilute auto exhaust. *Atmos. Environ.*, 18(4):847--854. doi:.

U. Platt, B. Alicke, R. Dubois, A. Geyer, A. Hofzumahaus, F. Holland, M. Martinez, D. Mihelcic, T. Klupfel, B. Lohrmann, W. Patz, D. Perner, F. Rohrer, J. Schafer, and J. Stutz (2002). Free radicals and fast photochemistry during BERLIOZ. *J. Atmos. Chem.*, 42:359--394.

K. A. Ramazan, D. Syomin, and B. J. Finlayson-Pitts (2004). The photochemical production of HONO during the heterogeneous hydrolysis of NO_2. *Phys. Chem. Chem. Phys.*, 6:3836--3843. doi:10.1039/b402195a.

G. Sarwar, S. J. Roselle, R. Mathur, W. Appel, R. L. Dennis, and B. Vogel (2008). A comparison of CMAQ HONO predictions with observations from the Northeast Oxidant and Particle Study. *Atmos. Environ.*, 42:5760--5770. doi:10.1016/j.atmosenv.2007.12.065.

J. H. Seinfeld and S. N. Pandis (2006). *Atmospheric Chemistry and Physics*. Wiley, Hoboken, NJ, 2nd edition.

K. Stemmler, M. Ammann, C. Donders, J. Kleffmann, and C. George (2006). Photosensitized reduction of nitrogen dioxide on humic acid as a source of nitrous acid. *Nature*, 440:195--198. doi:10.1038/nature04603.

K. Stemmler, M. Ndour, Y. Elshorbany, J. Kleffmann, B. D'Anna, C. George, B. Bohn, and M. Ammann (2007). Light induced conversion of nitrogen dioxide into nitrous acid on submicron humic acid aerosol. *Atmos. Chem. Phys.*, 7:4237--4248.

J. Stutz, K. W. Wong, L. Lawrence, L. Ziemba, J. H. Flynn, B. Rappengluck, and B. Lefer (2010). Nocturnal NO_3 radical chemistry in Houston, TX. *Atmos. Environ.*, 44:4099--4106. doi:10.1016/j.atmosenv.2009.03.004.

T. W. Tesche, J. G. Wilkinson, G. M. Stella, D. E. McNally, and C. F. Loomis (2010). Modeling protocol for the 2013 Houston, TX, air quality model study: Ensemble modeling and probabilistic attainment demonstration for the new 8-hour ozone National Ambient Air Quality Standard. Prepared for the Houston 8-hr Ozone SIP Coalition by Climate & Atmospheric Research Associates (Boise, ID) and Alpine Geophysics, LLC (Arvada, CO).

W. Vizuete, B. U. Kim, H. E. Jeffries, Y. Kimura, D. T. Allen, M. A. Kioumourtzoglou, L. Biton, and B. Henderson (2008). Modeling ozone formation from industrial emission events in Houston, Texas. *Atmos. Environ.*, 42:7641--7650. doi:10.1016/j.atmosenv.2008.05.063.

K. W. Wong, H. J. Oh, B. L. Lefer, B. Rappengluck, and J. Stutz (2011). Vertical profiles of nitrous acid in the nocturnal urban atmosphere of Houston, TX. *Atmos. Chem. Phys.*, 11:3595--3609. doi:10.5194/acp-11-3595-2011.

K. W. Wong, C. Tsai, B. Lefer, C. Haman, N. Grossberg, W. H. Brune, X. Ren, W. Luke, and J. Stutz (2012). Daytime HONO vertical gradients during SHARP 2009 in Houston, TX. *Atmos. Chem. Phys.*, 12:635--652. doi:10.5194/acp-12-635-2012.

G. Yarwood, S. Rao, M. Yocke, and G. Z. Whitten (2005). Updates to the Carbon Bond chemical mechanism: CB05. Final report prepared for US EPA. http://www.camx.com/publ/pdfs/CB05_Final_Report_120805.pdf.

R. Zhang, G. Sarwar, J. C. Fung, A. K. Lau, and Y. Zhang (2012). Examining the impact of nitrous acid chemistry on ozone and PM over the Pearl River Delta region. *Adv. Meteorol.* Article ID 140932. doi:10.1155/2012/140932.

X. Zhou, H. Gao, Y. He, and G. Huang (2003). Nitric acid photolysis on surfaces in low-NOx environments: Significant atmospheric implications. *Geophys. Res. Lett.*, 30(23):2217. doi:10.1029/2003GL018620.

X. Zhou, G. Huang, K. Civerolo, U. Roychowdhury, and K. L. Demerjian (2007). Summertime observations of HONO, HCHO, and O_3 at the summit of Whiteface Mountain, New York. *J. Geophys. Res.*, 112:D08311. doi:10.1029/2006JD007256.

X. Zhou, N. Zhang, M. TerAvest, D. Tang, J. Hou, S. Bertman, M. Alaghmand, P. B. Shepson, M. A. Carroll, S. Griffith, S. Dusanter, and P. S. Stevens (2011). Nitric acid photolysis on forest canopy surface as a source for tropospheric nitrous acid. *Nat. Geosci.*, 4:440--443. doi:10.1038/NGEO1164.

Z. Zhou, Y. He, G. Huang, T. D. Thornberry, M. A. Carroll, and S. B. Bertman (2002). Photochemical production of nitrous acid on glass sample manifold surface. *Geophys. Res. Lett.*, 29(14):1681. doi:10.1029/2002GL015080.

CHAPTER 5
FINAL THOUGHTS

The purpose of this work was to improve our understanding of the details surrounding Houston's extreme O_3 events in the real and modeled environments. This is the first time the NTOC problem has been considered within the 8-hr O_3 attainment framework, and our results confirmed that the dual-O_3 paradigm is still valid for Houston. The 2010 SIP modeling performed by the TCEQ was unable to reproduce observed NTOCs (Texas Commission on Environmental Quality, 2010). This is concerning because we found nearly 60% of NTOC days violated the 1997 0.08 ppm 8-hr O_3 standard. One purpose of regulatory models is to test pollution control strategies and demonstrate future attainment of the O_3 standard. In Houston, many O_3 violations have causes that are not represented in regulatory modeling. This makes the job of environmental regulators, who rely on models to understand the complex dynamics in the airshed, difficult indeed.

The first study in this work looked closely at the modeling performed in support of the TCEQ's 2010 SIP. Our earlier research showed that NTOCs occurred with notable frequency during the period that was modeled, and we found broad evidence that the model was missing this feature of O_3 pollution in Houston (Vizuete et al., 2011). With that in mind, we drilled deeper into the simulation data. We discovered that the model was not predicting the large spatial concentration gradients that appeared in ambient observations. While the model could simulate high O_3, it could not replicate the narrow plumes affecting individual monitors. We believe much of the model's deficiency stems from the choice of emission inventory. Significant evidence exists that links rapid O_3 production to variable HRVOC emissions (for example Kleinman

et al. (2002) and Ryerson et al. (2003)), but variable HRVOC emissions are absent in the SIP model. A second EI, one not used to demonstrate attainment of the O_3 standard, had an early morning HRVOC release from an industrial point source. We compared O_3 values predicted by the model using the two different EIs and found the HRVOC release led to a spatially limited plume of O_3 20-25 ppb greater than in the simulation without the release.

Our second study looked to a broader range of ambient measurements in an attempt to better characterize the conditions and origins of observed NTOCs. We found that nearly all NTOCs occur when monitors are downwind of the industrial ship channel. The remarkable strength of the relationship between wind direction and NTOCs is made more interesting when chemical data is analyzed. We used CH_2O concentrations as a marker for photochemical activity and showed that there are substantial differences between NTOC and typical O_3 days. CH_2O values were significantly greater in the early afternoon on NTOC days compared to typical O_3 days. This is expected following the rapid oxidation of HRVOCs because CH_2O is a product of VOC photochemistry. We also found evidence for industrial upset emissions in the hours preceding most NTOCs. We used SO_2 concentrations as a marker for industrial activity. At monitors where SO_2 is recorded, more than half of all NTOCs followed a sudden increase in SO_2. Taken together, our findings point to industrial emissions in the ship channel region as a likely cause of NTOCs.

In our third study, we shifted our focus back to the air quality model. While industrial emissions are an important factor in high O_3 events, they do not produce O_3 *per se*, but rather serve as a major source of free radicals like $^{\cdot}OH$. Radicals are key constituents in O_3 formation because they oxidize NO to NO_2. Increased system reactivity is achieved by augmenting radical budgets through VOC emissions or other means. We looked closely at missing sources of HONO, an important radical source,

in this last paper. Field campaigns in 2006 and 2009, as well as over a decade of laboratory experiments, identified new HONO formation mechanisms absent in 3-D photochemical models. Our major contribution in this work was to implement and test a surface sub-model that converts HNO_3 and NO_2 into HONO on the ground. The introduction of these heterogeneous reactions increased model reactivity, especially just following sunrise. Base case modeling without the surface sub-model predicted near-zero concentrations of HONO at night, though measurements showed this not to be the case. HONO that was produced by the surface sub-model overnight was immediately available for photolysis at sunrise. As a result, more than twice as much $^{\cdot}OH$ was created from HONO than in the base case. There was also an increase in the total VOC oxidized by $^{\cdot}OH$ in the first half of the day. Subsequent analysis and tuning of the surface sub-model is needed, but we demonstrated its conceptual viability. The result is a more realistic and accurate modeling framework that should become the standard for regulatory air quality modeling.

REFERENCES

L. I. Kleinman, P. H. Daum, D. Imre, Y. N. Lee, L. J. Nunnermacker, S. R. Springston, J. Weinstein-Lloyd, and J. Rudolph (2002). Ozone production rate and hydrocarbon reactivity in 5 urban areas: A cause of high ozone concentration in Houston. *Geophys. Res. Lett.*, 29:1467. doi:10.1029/2001GL014569.

T. B. Ryerson, M. Trainer, W. M. Angevine, C. A. Brock, R. W. Dissly, F. C. Fehnsenfeld, G. J. Frost, P. D. Goldan, J. S. Holloway, G. Hubler, R. O. Jakoubek, W. C. Kuster, J. A. Neuman, D. K. Nicks, Jr., D. D. Parrish, J. M. Roberts, D. T. Sueper, E. L. Atlas, S. G. Donnelly, F. Flocke, A. Fried, W. T. Potter, S. Schauffler, V. Stroud, A. J. Weinheimer, B. P. Wert, C. Wiedinmyer, R. J. Alvarez, R. M. Banta, L. S. Darby, and C. J. Senff (2003). Effect of petrochemical industrial emissions of reactive alkenes and NOx on tropospheric ozone formation in Houston, Texas. *J. Geophys. Res. Atmos.*, 108:4249. doi:10.1029/2002JD003070.

Texas Commission on Environmental Quality (2010). Revisions to the State Implementation Plan for the control of ozone air pollution: Houston-Galveston-Brazoria ozone nonattainment area. Austin, TX. Project No. 2009-017-SIP-NR.

W. Vizuete, H. E. Jeffries, T. W. Tesche, E. P. Olaguer, and E. Couzo (2011). Issues with ozone attainment methodology for Houston, TX. *J. Air Waste Manag. Assoc.*, 61:238--253. doi:10.3155/1047-3289.61.3.238.